COMPLEX DYNAMICS AND PHASE BEHAVIOR IN NON-EQUILIBRIUM MODELS: FROM LORENTZ MODELS TO LIQUID CRYSTALS

A Thesis
Presented to
The Academic Faculty

by

Ashley K. Tucker

In Partial Fulfillment
of the Requirements for the Degree
Doctor of Philosophy in the
School of Chemistry and Biochemistry

Georgia Institute of Technology
August 2011

COMPLEX DYNAMICS AND PHASE BEHAVIOR IN NON-EQUILIBRIUM MODELS: FROM LORENTZ MODELS TO LIQUID CRYSTALS

Approved by:

Dr. Rigoberto Hernandez, Advisor
School of Chemistry and Biochemistry
Georgia Institute of Technology

Dr. Jean-Luc Brédas
School of Chemistry and Biochemistry
Georgia Institute of Technology

Dr. Thomas Orlando
School of Chemistry and Biochemistry
Georgia Institute of Technology

Dr. Ken Brown
School of Chemistry and Biochemistry
Georgia Institute of Technology

Dr. Turgay Uzer
School of Physics
Georgia Institute of Technology

Date Approved: May 6, 2011

ACKNOWLEDGEMENTS

This work would not have been possible without the tremendous support I have received throughout graduate school. First, I would like to thank my advisor, Professor Rigoberto Hernandez. He has provided me with valuable advise and guidance. I would also like to thank the members of my committee: Prof. Jean-Luc Brédas, Prof. Thomas Orlando, Prof. Ken Brown and Prof. Turgay Uzer. I have had a wonderful experience working with the past and current members of the Hernandez group: Jeremy Moix, Gungor Ozer, Matt Hagy, Galen Craven and Shi Zong. Specifically Alex Popov and Eli Hershkovits have patiently helped me by providing a wealth of knowledge and creative ideas. I was also very lucky to have a friend and mentor in Ashley Ringer who helped keep me focused with her friendship and advice. I also had an amazing group of advisors and mentors at Westminster College that provided a strong foundation for my success as a graduate student. Specifically, Dr. Tricia Shepherd and Dr. Peter Conwell took particular interest in my academic future and provided advice, guidance and support. Finally and most importantly, I would never have completed my work without the unwavering support of my family. My husband, Garritt Tucker, provided more support than can be expressed here. He was never too busy to discuss ideas and he also provided a tremendous amount of emotional support. My parents, Gordon and Michelle Phillips always believed in me and encouraged me to do my best. My sisters and brother-in-law: Taylor, Nick, Alex and Jessica, have always been supportive and I am truly grateful for all of them. I also need to thank my papou, who taught me the value of education and provided an example of true character.

TABLE OF CONTENTS

LIST OF TABLES

LIST OF FIGURES

SUMMARY

Anisotropy in both the geometry and spatial arrangement of particles in liquids and soft matter lead to a variety of dynamical regimes and complex phase behaviors. Geometrically anisotropic particles have exhibited a variety of dynamical regimes and rich phase behavior. The non-trivial dynamics exhibited by such systems include Enskog diffusion, reptation and glassy dynamics. Anisotropy in the geometric components and spatial arrangement of a system also leads to preferred directions of transport, as is exhibited by solutes diffusing through ordered arrays or liquid crystals. Geometrically anisotropic particles possess the ability to exhibit mesophases indicative of a liquid crystal. For some systems the driver of the phase behavior is simply the degree of geometric anisotropy, where increasing geometric anisotropy leads to increased long-range and positional order. The geometric anisotropy of guest molecules greatly affects the transport through structured materials such as: porous gels and nano- and micro-structured materials. Spatially anisotropic systems show complex dynamical regimes and structure as well. A specific example of a spatially anisotropic system is the cytoskeletal network of a living cell. The spatial anisotropy of the network shows complex transport of media throughout the matrix, where trajectories exhibit hindered motion in certain areas of the network and directed, rapid motion in other areas.

The complex phase and dynamics in liquid and soft matter systems are directly related to the transport, optical and electronic properties of these systems. It has therefore been a challenge across many fields, to study such systems. One avenue in which to study these systems is through the use of computers. However, these systems are difficult to study computationally. Many of these systems possess complicated interactions between particles and large numbers of atoms. Often the dynamics of these systems exhibit disparate time and length scales, making integration of forces and torques a daunting task. It is therefore necessary to reduce the complexity of computational models describing these systems so

that they are realizable on computational platforms. To that end, this thesis has focused on two classes of simple modes: Lorentz models, where the surrounding solvent is stationary and one solute molecule is allowed to translate and rotate through the resulting network, and a liquid crystal model comprised of hard spherocylindrical particles that are driven by an external rotating electric field. Both of these models are amenable computationally and provide the fundamental physics necessary to capture the complex behavior indicative of the complex dynamics and phase behavior described above.

The Lorentz models studied throughout this work are comprised of a combination of needles and spherical particles. The particular version of the model useful to describing a variety of dynamical regimes, is that of a thick needle diffusing through an array of stationary scatterers. The resulting dynamics of the thick needle in a two-dimensional array of point scatterers shows three regimes of transport, the expected Enskog behavior at low scatterer density, reptative transport that gives rise to enhanced translational diffusion parallel to the long-axis of the needle at intermediate densities and finally a geometric trapping at large densities. The competition between suppression of rotational and translation motion perpendicular to the long-axis of the needle leading to reptation and suppression of the motion of the needle leading to trapping is determined by the ratio of the thickness of the needle to the average inter-particle spacing of the scatterers. In order for the needle to reptate, the length of the needle must be sufficiently longer than the average inter-particle spacing while the width remains somewhat small compared to the inter-particle spacing, creating an effective Edwards tube. A corresponding three-dimensional system is studied, where the scatterers are made spherical. In this system, the effective Edwards tubes are cut-off due to the excluded volume of the scatterers. The competition between reptation and trapping still is determined by the ratio of the needle width to the inter-particle distance. However, in three-dimensions, suppression of the translation motion perpendicular to the needle only occurs when the inter-particle spacing is small compared to the needle width. Thus, reptation is not observed. The structure formed by the stationary scatterers provide connections to diffusion of guest molecules through porous gels and nano- and micro-structured particles. Anisotropic transport has been observed in the motion of proteins with varying geometric

anisotropy with respect to the pore or channel size. The competing effects of length scales observed in these models lend knowledge to the processes that control diffusion of these guest molecules.

The opposite of the previously described Lorentz model is studied, where the stationary scatterers are needle-like particles and the solute is a spherical probe. In this model, a direct comparison between models with long-range orientational order and isotropically orientated scatterers is undertaken. The results of this study indicate the importance of directed collisions caused by the geometric and spatial anisotropy of the particles in the preferred direction of transport of the spherical probe. Also, the effect of the size of geometrically anisotropic nematogens is probed, by varying the scatterer length. Correlations in the VACFs along the direction of long-range order indicate highly correlated directed collisions. When the scatterer begins to exhibit a transition to geometric trapping, the correlations in the VACFs become negative and show increasing negative long-time tails. The functional form of the decay of these long-time tails are compared to previous work of a variety of Lorentz models. The effect of geometric and spatial anisotropy ultimately shows directed transport along the direction of long-range order and also staves off trapping. This model is directly connected to the complex diffusion observed in the transport of proteins through living cells, where complicated trajectories occur, showing moments of rapid directed motion and moments of hindered motion. This model also successfully reproduces the behavior observed in the diffusion of solutes in liquid crystal phases, where preferred transport is observed with increasing long-range order.

The second class of models discussed in this thesis, is a simple liquid crystal model. This model is comprised of nematogens formed from hard spherocylinders. The spherocylinders are aligned and driven by an external, rotating electric field. The field is coupled to the nematogens via a dipole along the long-axis of the spherocyinder. The frequency and field-dependent phase behavior is studied. For stationary fields, an overall stabilization of long-range order is observed, accessing liquid crystal phases that would not be accessible otherwise. However, upon rotation of the field, long-range order is seen to decrease. The loss in long-range order is more pronounced with increasing frequency and increasing volume

fraction and geometric anisotropy. When a constant frequency is chosen, and the field strength is varied, a reentrant phase behavior is observed. When a low field strength is applied, the long-range order possessed by the system is lost, upon increasing the field strength, the long-range order increases. This work provides an avenue in which to control the phase behavior of liquid crystal system by tuning parameters of an external rotating electric field.

The complex frequency and field dependent phase behavior of driven nematogens indicates that the dynamics of a spherical probe immersed in this system can also be tuned with respect to the parameters of the external field. The frequency dependent dynamics of a spherical probe immersed in driven nematogens is studied. The translational diffusion of the probe increases with increasing frequency, until a frequency of $\omega = 2$ ps^{-1} is reached. After this frequency is reached, a downturn in the diffusion coefficients is observed. At this frequency, the rotational motion of the nematogens show a transition to collision dominated dynamics, indicated by the complex decay of the rotational correlations. These results show that the dynamics of the probe are strongly coupled to the rotational dynamics of the nematogens. This data provides strong evidence suggesting that the transport of a spherical probe in orientable fluids can be controlled by tuning the parameters of the external field.

Overall this thesis provides advances in the description of the underlying physical processes of a variety of materials systems. We are able to accurately obtain transport coefficients and describe correlations of rotational and translational motion with respect to increasing spatial and geometric anisotropy. We are also able to access and control the phase behavior and dynamics in orientable fluids. Moreover, we were able to advance the use of simple Lorentz models and a simple LC model in describing complex dynamics and phase behavior.

CHAPTER I

INTRODUCTION

1.1 Motivation

Fundamental to a wide variety of fields, ranging from biology to engineering, are systems that exhibit anisotropy in the spatial arrangement and/or geometry of their components. Such anisotropy generates a wide range of observed dynamical and phase behaviors. For example, non-uniform dynamics seen in spatially heterogeneous systems include: intra and extra cellular transport, movement through polymeric networks, diffusion through pores, nanotubes and other structures, and many other processes. There are a large number of biological systems that display anisotropy in both the orientation and shape of their constituents. The environments within and surrounding living cells are heterogeneous, thus, these environments exhibit both geometric and spatial anisotropy leading to non-trivial dynamics and structural properties. One such example is the heterogenous cytoskeletal network in living cells. Lieleg and coworkers [63] found varying degrees of structural polymorphism in cytoskeletal networks that yield increasing heterogeneity in the network. Moreover, evidence exists of heterogeneous transport of proteins and other substances through the cell. One example is the heterogeneous transport of α_{1B}-adrenoceptor in living cells [39]. The trajectory observed throughout the cell shows two regimes of transport. The first is rapid and simultaneously directed motion of the protein. The second regime is hindered motion. Thus, the trajectory of the protein is complicated, exhibiting multiple dynamical behaviors. Studies of protein diffusion through hydrogels illustrate anisotropic transport depending on the geometric anisotropy (*i.e.*, aspect ratio) of the protein [36]. Anisotropic diffusion in stiff polymeric suspensions is observed due to the confinement of the polymer by the surrounding network, creating an effective tube, a so-called Edwards tube. The motion perpendicular to the tube is strongly suppressed, as is the rotational motion of the polymer, causing enhancement of the translational motion parallel to the tube. This

behavior is known as reptation. Reptation has also been experimentally observed in biologically significant polymer systems, like solutions of DNA chains [82] and semi-flexible actin filaments [54].

Other systems of importance to materials science and engineering also exhibit dynamical and structural properties influenced by geometric and spatial anisotropy. Polymer systems and filaments that are not biological in nature, display anisotropic, reptative motion. Solutions of single-walled carbon nanotubes in porous networks also show reptative motion [28]. Moreover, anisotropy is observed in the rotational motion of polymer melts constrained by nanometric confinement, producing long time tails in the correlation functions defining reorientational motion [57]. Porous media and media that possess micro- and nano-structures can also cause anisotropic diffusion. Nanoporous materials have shown anisotropic diffusion of the guest molecules moving through the channels and pores [100]. Additionally, more complex structural motifs of nanoporous materials, other than channels and pores, have been explored. Specifically, diffusion through a coiled pore microparticle shows anisotropic characteristics that are tunable by opening the mesopore [101].

These processes are ubiquitous within liquids and other soft matter; therefore, a fundamental understanding of the dynamical behavior of simplistic models lends vital insight to the ultimate understanding and control of these processes. Many simple models are able to capture rich dynamical and phase behavior indicative of more complicated liquid and soft matter. Such models provide amenable avenues to study complex phase and dynamical behavior by providing numerical studies that are realizable on today's computational platforms. These simple models include systems where the surrounding particles of the medium are stationary, a so-called Lorentz model, and a liquid crystal comprised of rod-like particles that interact via a hard-wall potential. While interactions in these models are simplistic, rich phase and dynamical behavior have been previously observed [9, 26, 25, 67, 13, 27, 46, 2]. The main goal of this thesis is to elucidate phase and dynamical behavior by studying these simple models. Specifically, this research utilizes a variety of related Lorentz models (comprised of a combination of rod-like particles and spherical/point particles) as well as a simplistic liquid crystal system comprised of rod-like particles.

1.2 Problem Definition and Thesis Objectives

Many liquid systems exhibit spatial and geometric anisotropy that gives rise to rich phase and dynamical behavior, providing areas of study suited for the use of simple models. For example, in the case of Lorentz models, previous work has shown that when the probe in the model exhibits geometric anisotropy (*i.e.*, is a needle), the probe will exhibit reptative diffusive motion when a critical density of scatterers is reached [47, 48]. In addition, liquids comprised of hard spherocylinders show phase behavior due to the geometric anisotropy of the particles. Liquid crystal phases composed of hard spherocylinders emerge as the geometric anisotropy of nematogens increases [69]. A number of liquid systems exhibit non-trivial dynamics when the system possesses some degree of spatial anisotropy. Such systems include transport of a tracer through an ordered array or liquid crystalline phases [108, 97, 56, 83, 58, 59]. Therefore, it is important to leverage simple models that are able to provide insight into the relationships of spatial anisotropy with these dynamical behaviors of tracer particles. To that end, this research aims to address the following:

1. A wide variety of dynamical regimes are observed in polymeric solutions with increasing polymer density, including reptative behavior at intermediate densities and ultimately glassy behavior when the density is large. Given this, is it possible to investigate these regimes with a simple Lorentz model? Specifically, what dynamical regimes are accessible by tuning the thickness of a two-dimensional needle in an array of stationary point scatterers? Are the effective Edwards tubes seen in the two-dimensional system observed in a corresponding three-dimensional system? Does reptation of a needle in a three-dimensional array of stationary scatterers occur or is the formation of Edwards tubes affected by the dimensionality of the model?

2. Many solutes immersed in solvents exhibiting anisotropy possess anisotropy in the resulting dynamics of the solute. For example, this occurs in systems that possess long-range orientational order. Can this behavior be captured by a Lorentz model comprised of geometrically anisotropic scatterers? How does the geometric and spatial anisotropy of rod-like scatterers in a Lorentz model of stationary needles affect the

dynamics of a spherical probe?

3. Systems comprised of particles displaying significant geometric anisotropy display rich phase behavior. These phases vary in terms of their degree of long-range orientational and positional order. Perturbations to the geometrically anisotropic particles (*i.e.* nematogens) can stabilize long-range order and thus, produce phases that were not previously accessible. Such perturbations include the presence of an external field. If an external, rotating electric field is imposed, what is the frequency dependent phase behavior of hard nematogens driven by the field? Is there an effect on the phase behavior due to varying the field strength?

4. Assuming that there is an effect in the phase behavior of a driven system of nematogens, the resulting dynamics of a probe would be affected as well. Therefore, it is important to elucidate the frequency dependence of the probe dynamics. Moreover, is it possible to tune the probe dynamics by changing the parameters (*i.e.*, frequency and strength) of the driving field?

Given these questions, the goal of this thesis is to determine the effect of geometric and spatial anisotropy on the dynamics of a probe in a variety of Lorentz models, deduce the effect of driving nematogens with an external field, as well as the effect of increasing the aspect ratio, L/D, of the nematogens and study the dynamics of a spherical probe in externally driven nematogens. This leads to the following specific goals of this thesis:

- Investigate the dynamical regimes accessible to a two-dimensional thick needle in stationary point scatterers. Using this model, we aim to measure diffusion coefficients of the various dynamical regimes exhibited by polymeric systems and probe the parameters that give rise to these regimes. Also a connection between the description of the underlying physical processes governing these regimes in the simple model and the complex physical systems of interest is desired.

- Given the previous goals, using a three-dimensional corresponding Lorentz model, further exploration of the parameters governing reptation in complex systems are

studied. Specifically, the fragility of Edwards tubes by studying a three-dimensional array of stationary spherical scatterers with a traversing rod-like needle is investigated, providing knowledge about the fundamental process driving reptation in the simple models and also in more complex systems.

- Provide a juxtaposition of measurable transport quantities for systems with no spatial anisotropy and systems with long-range order. Using a simple Lorentz model, a direct comparison between systems where only the degree of long-range order is altered is feasible. A description of the dynamics of a probe in stationary needles and the dependence of the dynamics on long-range orientational order as a function of increasing the geometric anisotropy of the needle scatterers is pursued.

- Determine the effect of an external perturbation, in the form of a rotating external field, on the phase behavior of a liquid crystal and elucidate avenues in which to control/access phases not accessible without external perturbations. Using a system of nematogens comprised of spherocylindrical particles in the presence of an external field makes the investigation of the phase behavior of nematogens driven by an external field with changing frequency and constant field strength realizable. Also, we aim to describe the phase behavior with increasing field strength at a constant frequency.

- Given the previous goal, if it is possible to control the phase behavior and response of liquid crystal systems, then a description of the dynamics of a spherical probe in the driven system is necessary in order to develop methodologies to direct the transport of the probe using the parameters of the external field. To that end, the dynamics of a spherical probe in a LC system of nematogens driven by a rotating field with varying frequencies must be explored.

First, previous work on infinitely thin needles in a two-dimensional array of stationary point scatterers has shown a variety of diffusive behaviors. The needle exhibits an increase in translational diffusion when a critical density of point scatterers is reached while a simultaneous suppression of rotational motion is observed. Thus, two dynamical regimes are seen: the expected Enskog behavior at low scatterer densities and the regime characterized

by the enhancement of translational diffusion [47, 48]. The observed enhancement is due to the reptative motion of the needle in the scatterers; the needle is able to traverse parallel to the long axis of the needle with ease, while both the perpendicular and rotational motion are suppressed. The surrounding scatterer network creates effective Edwards tubes, enhancing translational motion. Reptative motion has been previously observed in dense systems of semi-flexible polymers as well as fluids of rigid rod-like particles [23, 19]. Because the needle is infinitely thin, entrapment of the needle will never occur and the translational diffusion coefficients will continue to increase with increasing scatter density. Therefore, a more realistic representation would allow for possible needle entrapment due to its excluded volume/area which is explored by adding finite thickness. Thus, this thesis determines the influence of needle thickness on the observed dynamical regimes.

Second, numerical studies employing a three-dimensional needle in stationary spherical particles are leveraged to determine whether similar translational enhancement seen in the two-dimensional model is observed in three-dimensions. Previous work has shown that a two-dimensional needle with finite thickness does reptate due to the surrounding scatterers [74]. The surrounding scatterers form an effective tube allowing for enhanced diffusive motion parallel to the long axis of the needle. The fragility of these tubes, however, would presumably be affected by needle width and the geometry of the surrounding scatterers.

Third, Lorentz models show a transition between dynamical regimes based on scatterer density. With increasing scatterer density, long-time tails in the velocity autocorrelation functions and transitions in the dynamics have been observed [8, 9, 26, 25, 67, 13, 27, 46]. The effect of arranging geometrically anisotropic scatterers with long range order along a director is studied as well as increasing the length of the needle scatterer. Previous work has shown rich dynamical behavior of a probe when the surrounding fluid possesses some degree of long-range order [108, 83, 58]. The diffusion of a spherical probe in a liquid crystal system near the isotropic-nematic phase transition has shown anisotropic diffusion [108]. Also, the effect of the size of the probe has been studied when colloidal rods from an entangled network and caging of the solute is induced [83, 58].

Fourth, liquid crystals exhibit complex phase behavior in the presence of a strong aligning external field. Previous experimental and theoretical work have shown stabilization of LC phases with long-range order when the external field is held static [49, 20, 95]. In addition, previous experimental work has investigated the dynamics of the director when aligning fields are pulsed [65, 66, 70, 7, 77]. Theoretical descriptions have also indicated interesting dynamics of the director when an external field is rotated [41]. In this thesis, the phase behavior is investigated when the external field is rotated with respect to frequencies that are approximately on the order of rotational motion of the particles themselves. Furthermore, the possibility of reentrant phase behavior is explored by varying the field strength and holding the frequency constant.

Finally, the frequency dependent dynamics of a spherical probe in externally driven nematogens is elucidated. The dynamics of the spherical probe immersed in the driven nematogens is compared to that of the dynamics of the nematogens themselves. It appears that the rotational motion of the nematogens is coupled to the dynamics of the spherical probe; when the rotational motion begins to undergo a transition, the translational diffusion coefficients of the spherical probe show a change in the observed trend with respect to increasing frequency. Previous work on liquid crystal systems under the influence of an external, static field has indicated that the rotational motion is coupled to the translational order exhibited by the nematogens [20]. This thesis aims to discover if this coupling is visible between the nematogens and a spherical probe immersed in the driven nematogens.

1.3 Significance of Research

The significance of this thesis can be described by two main categories. First, this work provides an advance in the study of materials and the properties of materials. A variety of dynamical regimes are observed in polymeric systems, where reptation of the species is possible. Also, many suspensions, when the density is large, show glassy behavior due to the kinetic arrest of the suspension. The dynamics of macromolecules diffusing through porous gels also show a variety of dynamical regimes. The dynamics of the needle in stationary scatterers gives rise to the dynamical regimes seen in these complex systems. The

three non-trivial regimes observed are the low density regime described by Enskog diffusion, the intermediate density regime where the formation of effective Edwards tubes causes reptation, and ultimately enhanced transport of the needle and finally, the glassy regime observed at large densities where the needle is trapped. The three dynamical regimes illuminate the competition between caging effects and reptation. The Lorentz models studied provide a direct route to investigate this competition by altering the thickness of the needle with respect to the spacing between scatterers as well as the excluded volume of stationary scatterers in three-dimensions. This work provides a basis for understanding the balance between the suppression necessary to form the Edwards tubes, that leads to reptation, and the glassy entrapment of the solute. Thus the thick needle shows the existence of several transport mechanisms, vitally important in complex systems.

Other material processes that exhibit dynamics dependent upon the geometric and spatial anisotropy of the constituents of the system include: diffusion of solutes through liquids crystals, porous gels, micro- or nano-structured materials or ordered arrays, and solutes in suspensions of *fd* virus or other semi-flexible filaments [108, 97, 56, 83, 58, 59]. The resulting dynamics of the solute show preferred directions of transport when the surrounding structure or matrix possess long-range order. It has been previously observed, that the size of the tracer with respect to the resulting mesh created by the surrounding network of liquid crystals or filaments, greatly determines the mode of transport of the solute, resulting in trapping when the size of the solute is exceedingly large relative to the free volume in the matrix. The study contained in this thesis provides an understanding of the effect of long-range order as well as the effect of increasing the length, and therefore geometric anisotropy, of scatterers. A preferred direction of transport is observed and the underlying dynamics of this system point to the importance of directed collisions in producing this preferred direction of transport. A fundamental difference between the motion along the direction of long-range order and the perpendicular directions, as evidenced by the correlations in translational velocity, is observed. The resulting structures observed in this work suggests that the structure of the surrounding media, *i.e* porous gels, suspension of semi-flexible filaments or liquid crystal, greatly affects the extent to which transport is directed.

The unique phases exhibited by LC systems leads to novel optical and electronic properties, thus the ability to control or drive the possible phases is desirable. Previous work has indicated the ability to stabilize long-range order by applying a stationary field [110, 20, 95]. Inducing a change in the direction of the director is also possible by imposing pulsed or oscillating fields [61, 10, 65, 66, 70, 7, 77]. The work in this thesis investigates the effect of a rotating external field on a LC. The study of driven nematogens by an external field provides insight into complex phase behavior. Long-range orientational order is stabilized by a stationary field when conditions would not permit such order without the field, consistent with previous work. When the field is rotated with a given frequency, destabilization of long range order is seen. Reentrant long-range order is also obtained by increasing field strength, thus providing another potential avenue to control the phase of a LC system.

Previous work using reduced dimensional models on the diffusion of solutes through anisotropic solvents have suggested that the solute could be driven to diffuse in preferred directions [45]. By modeling a tracer in driven nematogens, we are able to show frequency dependent behavior of the diffusing spherical probe, indicating that it is possible to selectively direct the transport of a solute by induced perturbations on the solvent. The patterns recognized in the frequency dependent dynamical behavior of the probe can be utilized to drive the diffusion of probes in varying liquid crystal solvents. The work provided in Chapter 7 illustrates that with increasing frequency, the probe shows an increase in the translational diffusion coefficients, until the frequency is increased to a value greater than $\omega = 2$ ps^{-1}. At this frequency, the diffusion coefficients begin to decrease. Also at this frequency, the rotational correlations of the nematogens appear to undergo a transition to collision dominated dynamics that produces large long-time tails in the rotational correlations. Thus, it appears the dynamics of the spherical probe are directly coupled to the rotational motion of the nematogens, providing an avenue in which to control the diffusion of the spherical probe.

The other significant contribution of this work is the advancement of simple models in describing the non-trivial behaviors observed in complex systems. In studying Lorentz models with rod-like tracers, we are able to reconcile multiple dynamical regimes in one

model. The Lorentz model studied in Chapter 3 is able to reconcile the enhancement observed by a reptating needle [47, 48] with the glassy behavior of Moreno and Kob [74], providing a more realistic model. Due to the excluded area of the needle, Enskog behavior is observed at low scatterer densities as well as reptative and glassy regimes. We also elucidate the influence of the geometry of the surrounding matrix on the dynamics of the needle. If scatterers are given excluded volume in a three dimensional system, there is a competition between end-cap collisions and reptative behavior caused by suppression of rotational motion and suppression of translational motion perpendicular to the long axis of the needle. When the scatterers possess excluded volume, end-cap collisions shorten the effective Edwards tubes and reptation is not observed, thus Edward's tubes are fragile depending upon the structure of the surrounding matrix.

The study of Lorentz models with stationary needle scatterers elucidates the influence of geometric and spatial anisotropy which, as previously described, is vital in many polymer and confined systems. The entrapment due to geometric confinement is staved off with long-range orientational order of the needle scatterers. We also observe negative long time tails in the velocity autocorrelation function (VACF) when the probe particles begin to rattle in cages formed by the surrounding network, consistent with previous Lorentz models [8, 9, 26, 25, 67, 13, 27, 46]. The Lorentz models studied in Chapter 5 extend the previously studied Lorentz models by adding the additional parameters of geometric anisotropy and degree of long range order of the scatterers.

The LC model used through Chapter 6 and 7 are based upon spherocylindrical LC models used previously throughout the literature [78, 31, 34, 84, 80, 99, 69, 49, 96]. However, the model provided here, has the added complexity of the external driving field. This model provides only the fundamental interactions necessary to produce LC phases as well as a response to an external field. In this model, we have leveraged the fact that simply increasing the geometric anisotropy of the particles in the model results in rich LC phase behavior. Also, we have outlined how the coupling between an imposed dipole along the long-axis of the needle and the external electric field by a torque inducing rotation about the center of mass of the particles is enough to probe the phase and dynamical behavior of

nematogens under the presence of an external rotating field. Using this model, the frequency and field strength dependent phase behavior is able to be studied.

Overall, the results of this thesis provide a fundamental description of the underlying physical processes that produce non-trivial dynamical regimes and phase behavior of liquids and soft matter. The study of the simple models provided in this thesis exhibit complex dynamical regimes, indicative of dynamics in a large number of complex systems. These systems include polymers, living cells, liquid crystals, colloidal suspensions, silica gels etc. Understanding the rich dynamics and phase behavior of these systems can potentially lead to more fundamental understanding of the complex systems the models represent and ultimately provide an understanding of the effect of imposed anisotropy that leads to the ability to control and stabilize desired phase and dynamical behaviors. Furthermore, advancements in the use of simple models for liquid and soft matters systems have been made by extending the current studies of Lorentz and LC to the models outlined in this work.

1.4 Thesis Structure

A brief description of previous work, methodologies and dynamical behavior is provided in Chapter 2. In Chapters 3 through 5, a variety of Lorentz models are discussed. Chapter 3 describes the numerical data for a needle of finite thickness diffusing through a two-dimensional array of stationary point scatterers. Chapter 3 is adapted from published work in Ref. [104]. Such models exhibit complex dynamical behavior that is seen in polymeric systems. Three distinct dynamical regimes are observed with respect to increasing scatterer density; Enskog behavior at low scatterer density is seen up to a critical density where reptative motion is dominant due to effective Edward's tubes. The onset of reptative motion causes an enhancement in translational diffusion coefficients. At large scatterer densities, geometric trapping is observed, giving rise to a downturn in diffusion coefficients.

Further investigation of the dynamics of a needle in stationary scatterers is included in Chapter 4. In this work, a needle with finite thickness is allowed to traverse through a three-dimensional stationary array of spherical scatterers. This chapter is adapted from published work in Ref. [105]. Upon increasing the scatterer density, reptative enhancement

is not observed. This is due to the excluded volume of the scatterers, shortening the effective Edwards tubes and never allowing the needle to reptate. Reptation of an infinitely thin needle is not observed either. The loss of Edwards tubes is also prevalent in the velocity autocorrelation functions, where backscattering begins to occur, giving rise to negative correlations in the velocity correlations.

The dynamical regimes of the reverse system described in Chapter 4, where the scatterers are now needle-like particles and a spherical probe is allowed to move throughout the resulting mesh, is described in Chapter 5. The effect of geometric anisotropy of spherocylindrical scatterers on a spherical probe is outlined. The scatterer particles are either aligned along some director, *i.e.*, a stationary nematic phase, or are isotropically oriented. Upon increasing the aspect ratio of the stationary scatterers, we find that the long-range order in the stationary nematic phase staves off glassy behavior due to effective channels created along the nematic director. Large correlations in the velocity along the director due to directional collisions through the tube are observed. When the geometric anisotropy of scatterers increases, entrapment begins to occur, causing long-negative time tails in the velocity autocorrelation function. The functional decay of the long time tails are provided.

Chapter 6 describes the phase behavior of nematogens, formed by the same needle-like particles used in the model described in Chapter 5, driven by a rotating external electric field. The frequency dependence, as well as aspect ratio and density dependence, is probed thus providing a three-dimensional phase diagram with respect to volume fraction, aspect ratio and rotating frequency. With increasing frequency, destabilization of long-range order is observed. The expected result of stabilization of long-range order with stationary fields is also observed. The nematic order parameters and orientational correlation functions are provided in this study. Furthermore, the effect of electric field strength is also probed as the volume fraction and aspect ratio are held constant. A reentrance in phase behavior is observed with increasing field strength. With no field applied to the system of nematogens, long-range order is exhibited. When the field strength is low, disruption of the long-range order is seen but upon further increasing the field strength, long-range order reoccurs and ultimately results in an overall increase in long-range order.

Chapter 7 is the culmination of the Lorentz and liquid crystal models described in Chapters 3-6. In this work, a spherical probe is allowed to diffuse through the driven nematogens, whose phase behavior is described in Chapter 6. The frequency dependent dynamical behavior of a spherical probe is determined and compared to the resulting dynamics of the driven nematogens. The diffusion of the spherical probe is strongly coupled to the rotational motion of the nematogens. The decay of the VACFs and the rotational correlation functions show multi-exponential decays indicative of complex dynamics.

Finally, concluding remarks, significant findings and the overall contribution of this work as a whole, are provided in Chapter 8. The significant findings of Chapters 3-7 are summarized and connections are made to experimental results and other model systems. Furthermore, additional work and future directions of this research are discussed to provide a path forward, building on the findings of this thesis.

CHAPTER II

BACKGROUND

2.1 Introduction

All of the numerical work provided in this thesis has been carried out using molecular dynamics methods. Molecular dynamics (MD) is a computational technique used widely for a variety of systems such as proteins, colloidal suspensions, polymeric systems and liquid crystals. The basics of MD rest upon the classical equations of motion for the system of interest. The trajectories generated using MD are dependent upon the potential used to describe the inter-particle interactions and the collision dynamics employed, pointing to the inherent simplicity of MD. Once the positions and velocities of each particle in a given system are known, any property that depends on the positions and momenta can be determined. The following describes the basics of MD as well as a brief (and certainly not exclusive) description of inter-particle potentials. A description of the metrics used throughout this thesis is provided and finally, an overview of previous work for Lorentz models and the relevant liquid crystal systems are also provided.

2.2 Molecular Dynamics Methods for Liquid Systems

2.2.1 Classical Dynamics and Equations of Motion

The classical equations of motion can be written in many forms. The Newtonian equations of motion are the most familiar but it is more general to write the equations of motion in terms of the Lagrangian. The Lagrangian is defined as,

$$\mathcal{L} = \mathcal{K} - \mathcal{V}, \tag{1}$$

where the first term, $\mathcal{K}$, is the kinetic energy of the system and $\mathcal{V}$ is the potential energy. The Lagrangian equation of motion is therefore defined as,

$$\frac{d}{dt}(\partial\mathcal{L}/\partial\dot{q}_k) - (\partial\mathcal{L}/\partial q_k) = 0 \tag{2}$$

where the generalized cartesian coordinate are q_k, the time derivative is $\dot{q}_k$ and $\mathcal{L}$ is the Lagrangian defined in equation 1. The kinetic energy of the system, $\mathcal{K}$, is defined as the sum of the momenta for each particle, k, in the system.

$$\mathcal{K} = \sum_{k=1}^{N} \sum_{\alpha} p_{k\alpha}^2 / 2m_k \tag{3}$$

Equation 3 defines the kinetic energy, $\mathcal{K}$, where N is the total number of particles, p is the momenta conjugate to the coordinates q. The index α denotes the x,y and z components of the momentum. The potential energy, $\mathcal{V}$, describes the interactions between the particles in the system. Potential functions can range from hard-sphere interactions to complex functional forms describing interactions between pairs, triplets etc. of particles in the system. The potential defines the forces and torques on a particle due to the surrounding system. When the form of the kinetic energy given in equation 3 and a well-behaved form for the potential is used, the equation of motion defined in equation 2 becomes,

$$m_k \ddot{r} = \mathbf{f}_k \tag{4}$$

where the mass of particle k is m_k and the force $\mathbf{f}_k$ is found from the gradient of the potential, *i.e.*,

$$\mathbf{f}_k = -\nabla_{r_k} \mathcal{V}. \tag{5}$$

Equation 5 describes how the force acting on atom k can be determined from the Lagrangian. The equation of motion given by equation 4 defines the translational motion of the center of mass of each particle in the system as a function of the force on the particle determined from equation 5.

The conjugate momenta, p_k to coordinate q_k has been mentioned in describing equation 3. The conjugate momenta can be obtained by the following.

$$p_k = \partial \mathcal{L} / \partial \dot{q}_k \tag{6}$$

The Lagrangian defined in equation 1 is a function of the generalized coordinates (q_k) and its time derivative ($\dot{q}_k$). The equations of motion can also be written in terms of the coordinates and conjugate momenta. This form involves the Hamiltonian, $\mathcal{H}$.

$$\mathcal{H}(\mathbf{p}, \mathbf{q}) = \sum_{k} \dot{q}_k p_k - \mathcal{L}(\mathbf{q}, \dot{\mathbf{q}}) \tag{7}$$

where the velocity, $\dot{q}_k$, can be written as some function of the momenta. Using the Hamiltonian, the equations of motion for the system become

$$\dot{\mathbf{r}}_k = \mathbf{p}_k/m_k \tag{8a}$$

$$\dot{\mathbf{p}}_k = -\nabla_{\mathbf{r}_k}\mathcal{V} = \mathbf{f}_k \ . \tag{8b}$$

Therefore, computing trajectories for the center of mass for the atoms in the system, we must either solve the second-order differential equation given by equation 4 or by solving the set of first-order differential equations given by equation 8.

A defining result of these equations of motion is that the particle trajectories determined by these equations of motion are reversible in time. That means if the signs of the velocities and momenta are reversed, the particles can retrace their trajectory. Many algorithms used to find collision times for non-spherical particles take advantage of this by finding collisions after they have already occurred and then moving the particles back to colliding contact by reversing the velocities of the particles. Additionally, there exists generalized coordinates for both versions of the equations of motion where $\mathcal{V}, \mathcal{H}$ and $\mathcal{L}$ are independent of these generalized coordinates. Also, a key property of the Hamiltonian, is that it is a constant of motion; the total energy of the system is conserved.

2.2.2 Potentials and Generating Trajectories

The equations of motion described in the previous section involve the calculation of the forces and torques imposed upon each particle. By differentiating the potential $\mathcal{V}$ (equation 5) the resolved forces and torques are calculated. Therefore, the intermolecular interactions are described by the chosen potential. The simplest interaction often used in MD simulations is the hard-sphere potential shown in Figure 1.

$$\mathcal{V}(r) = \begin{cases} 0 & \text{if } \mathbf{r} \geq \sigma \\ \infty & \text{if } \mathbf{r} < \sigma \end{cases} \tag{9}$$

This potential is a pair-wise potential in which the value is 0 until two particles touch or collide, then the potential is ∞, shown in equation 9. This potential form keeps particles from penetrating each other and does not provide any other interactions. A large number

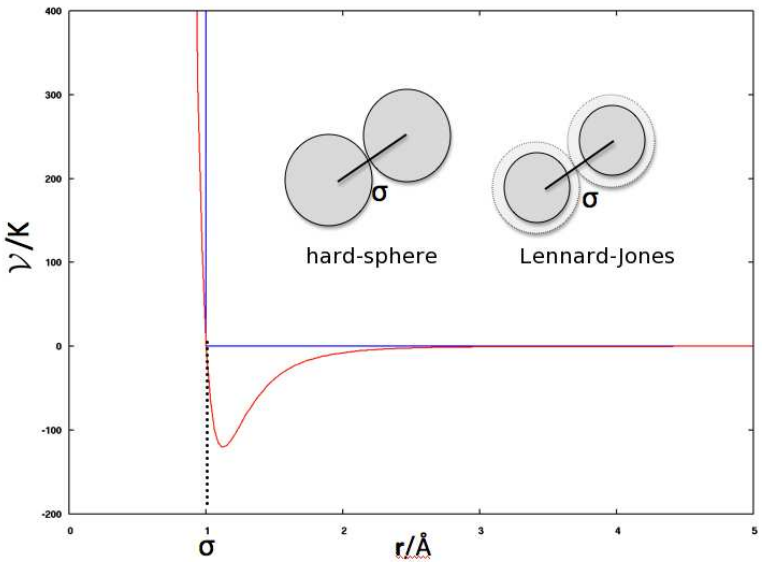

Figure 1: A plot of the hard sphere potential with radius σ (blue curve) and the Lennard-Jones potential (red curve). The radius for the hard sphere fluid is defined as well as for the Lennard-Jones fluid, both occur at 1.

of more complex potential energy functions have been developed. Besides the hard-sphere potential, the Lennard-Jones potential is an ubiquitous potential that provides attractive and repulsive forces [60]. The Lennard-Jones potential is a pairwise potential of the form

$$\mathcal{V}(r) = 4\epsilon[(\sigma/r)^{12} - (\sigma/r)^{6}] \tag{10}$$

where the parameter ϵ defined the well depth, σ is the collision diameter and r is the distance between the centers of mass. The parameters in the LJ potential are dependent upon the particles in the system. Many quantum mechanical methods have been used to determine potential energy landscapes for varying atom types. Numerous studies have gone into parameterizing, fitting and correcting potentials to accurately describe complex intermolecular interactions. While the hard-sphere potential may seem over simplistic, rich dynamical behavior is obtained using this potential. Its employment in MD simulations also provides a strong base for additional work with more complicated interactions.

In order to generate trajectories for particles interacting via a hard-sphere potential the following steps must be taken: First, the next collision in time must be calculated, then the particles are moved to that collision. When the particles are in colliding contact, the

proper collision dynamics must then be determined to update the velocities of the colliding pair. The impulse of the collision must be determined and the post-collisional velocities computed. The particles can then be moved forward in time according to the equations of motion described previously with the newly calculated post-collisional velocities.

A large number of algorithms have been developed to find the collision times of hard particles. Spherically symmetric particles have been well studied. When the particles in question lose spherical symmetry, the algorithms to determine collision times become more complex but have also been established. A good review of the algorithms developed for both spherically symmetric and spherically asymmetric molecules is located in Allen and Tildesley [3]. Due to the hard-sphere potential, the particles in-between collisions, translate and rotate freely in space, thus the trajectories for hard particle simulations are generated collision to collision instead of with a consistent time-step, as used in soft-body dynamics simulations. Once the system is able to be modeled computationally, any metric based upon the positions and momenta of the particles in the system can be determined, such as the mean-square displacement and correlation functions.

2.3 Diffusion, Mean-Square Displacement and Correlation Functions

One metric used to measure the mass transport of a system is the diffusion coefficient. The classical treatment of diffusion coefficients involves determining the temporal evolution of the probability density of the mass in question at a position $\mathbf{r}$. The diffusion coefficient provides this information. The classical diffusion equation is given in equation 11.

$$\frac{\partial}{\partial t}p(\mathbf{r},t) = D\nabla^2 p(\mathbf{r},t) \tag{11}$$

The probability distribution with respect to position and time is $p(\mathbf{r},t)$, D is the diffusion coefficient, and the del operator is ∇. The diffusion coefficient itself can be related to the mean-square displacement and is defined as

$$D = \lim_{t\to\infty} \frac{\Delta r(t)}{2dt}, \tag{12}$$

where d is the dimensionality of the system and $\Delta r(t)$ is the mean-square displacement. Equation 12 is known as the Einstein relation. When t approaches infinity, the mean-square displacement (MSD) will follow the behavior of $MSD \sim t^{-1}$. Practically speaking, ballistic simulations will transition to diffusive behavior after multiple collisions, giving rise to diffusive behavior in the MSD after some finite amount of time. This allows for the use of equation 12 in a realizable time scale. Deviation from this behavior results in sub-diffusive behavior, if the exponent is less than 1, or super-diffusive behavior if this coefficient is larger than 1 and less than 2 (indicative of ballistic motion). There is also a well-known prediction describing the relationship between the diffusion coefficients and the density of the system. The Enskog theory of hard-sphere fluids is a generalization of the Boltzmann equation that predicts that the diffusion coefficients should decrease with increasing density, $D \sim 1/\rho$.

Another way to elucidate the dynamics of a system is to investigate the correlations in the velocities with respect to time. The velocity-autocorrelation function (VACF) gives this data.

$$C_v(t) = \frac{1}{d}\langle v(0) \cdot v(t)\rangle. \tag{13}$$

The VACF, $C_v(t)$, is given in equation 13 where the velocity is given by $\mathbf{v}$, d is the dimensionality and the brackets denote an ensemble average.

$$D = \lim_{t\to\infty} \frac{\Delta r(t)}{2dt} = \int_0^\infty C_v(t)dt \tag{14}$$

The VACF can also be related back to the mean-square displacement by the relation in equation 14 known as the Green-Kubo relation. This relates the diffusion coefficient back to the underlying dynamics of the system. The VACF, when normalized, will start at 1 at $t = 0$ and then decay down to zero with increasing time If the diffusional process is a Markovian process, events at one time are uncorrelated at subsequent times, then $C_v(t)$ will decay exponentially. However, a vast body of work has deduced non-exponential decay of varying functional forms depending upon the system. The functional form of

long-time tails is often studied computationally as well as the origins of the long-time tails [2, 8, 9, 26, 25, 67, 13, 27, 46].

The rotational motion of a molecule can be probed using a variety of methods. For two-dimensional systems, it is possible to measure the mean-square angular displacement (MSAD). The MSAD measures the angle traversed by a rotating particle with respect to its original orientation at t=0. Similar methods to extract the translation diffusion coefficients from the MSD can be used to determine the rotational diffusion coefficients from the MSAD. It is also possible to calculate the velocity autocorrelation function for the angular velocity, ω. However, these correlations are not directly observable experimentally, but the shape of this function can be related to the shape of the reorientational correlation function [40]. The reorientational orientation correlation function, $C_1(t)$, describes correlations in the orientations of non-spherically symmetric molecules and is defined as

$$C_l(t) = \langle P_l[\mathbf{u}_i(t) \cdot \mathbf{u}_i(0)] \rangle \ , \tag{15}$$

where P_l is the Legendre polynomial, and $\mathbf{u}_i$ is the unit vector parallel to the internuclear axis of molecule i. For $l = 1$ equation 15 becomes

$$C_1(t) = \langle \hat{\mathbf{u}}(t) \cdot \hat{\mathbf{u}}(0) \rangle \ . \tag{16}$$

The reorientational correlation functions are applicable to linear molecules and also molecules where all three principal moments of inertia are identical, spherical top molecules. Once calculated, this quantity is more useful than others because it can be directly compared to experimental data, while the angular VACF cannot. The function calculated from equation 16 is experimentally measurable by infrared absorption; it is related to the spectral band-shape [40]. If the rotational motion can be described as a diffusive Markovian process, *i.e.*, the orientation becomes uncorrelated in small steps in time, then the rotational motion is said to follow the Debye approximation and the function calculated in equation 15 can be modeled as

$$C_1(t) = \exp[-l(l+1)D_R] \,, \tag{17}$$

where D_R is the rotational diffusion coefficient and l is the corresponding integer of the Legendre polynomial used to calculate the correlation function. While this expression is very powerful, it doesn't accurately describe rotational motion for all density regimes of all liquids. At low densities, the particle can easily rotate back on itself giving rise to negative correlations in $C_1(t)$. The process has been previously described as J-diffusion and is described in Refs. [37, 11]. Also, deviations from the Debye approximation are evident in high torque fluids, like liquid acetonitrile, at large densities [40].

2.4 Lorentz Models

As described previously, one model that provides interesting dynamical behavior that is also amenable computationally is a Lorentz model. The model was first introduced to describe the diffusion of electrons in a metal by Lorentz. It has also been used to describe the scattering of electrons from impurities as well as theories of neutron transport and diffusion in binary mixtures when the species have disparate masses. In these systems, one probe particle is allowed to move through an array of stationary obstacles. The probe can either move ballistically (scatterers and probe are in vacuum) or diffusively with a dampening Brownian or Langevin solvent. The probe interacts with the scatterer through a variety of potentials ranging from hard interactions to more complex soft interactions. There are also multiple variants of Lorentz models that vary depending upon how the particle encounters the scatterer. In some models, the probe is allowed to hop from one scatterer to another in a stochastic way. In other models, the probe particle is given a velocity and is allowed to traverse the space. The latter variant is the focus of this thesis. Upon encountering the scatterers, some Lorentz models allow for reflection by the scatterer or transmission through the scatterer. Still in other models the scatterers reflect the probe regardless. Variants of the Lorentz model have proven to show useful insight into dynamical processes [47, 48, 64, 106, 46, 76, 30, 74, 75, 62, 26, 25, 67, 9]. Two examples of Lorentz models are depicted in Figure 2. In the depicted models, the probes traverse the space with

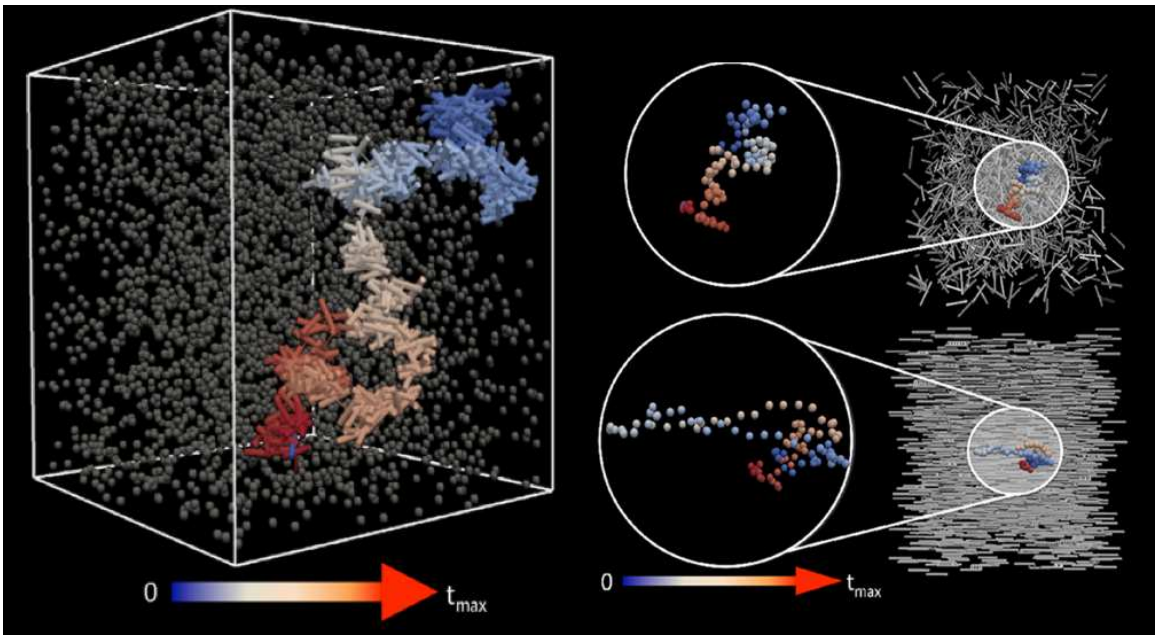

Figure 2: Two Lorentz models. The left panel shows a three-dimensional needle traversing through stationary spherical scatterers. The coloring of the needle indicates time in the trajectory, progressing from blue at $t = 0$ to red at $t = t_{max}$. This Lorentz model is the subject of Chapter 4. The right panel depicts a spherical probe traversing through stationary needle scatterers with the isotropic orientation of scatterers shown in the top panel. The bottom panel shows scatterers with long-range orientations. The spherical probe is also colored with respect to time. This Lorentz model is the subject of Chapter 5

a constant velocity and collide with the stationary scatterers of varying geometries. A large body of work on Lorentz models exists in the literature. Much of this work has focused on the long-time behavior that persists in the dynamics of the probe. Long-time tails in the VACF are indicative of interesting physics taking place in the system *i.e.* a non-Markovian process. Long-time tails were first observed in hard sphere fluids in the seminal work by Alder and Wainwright [2] where non-exponential decay was observed in the VACFs. This was explained by the vortex flow caused by the hydrodynamic effect of the collision of the hard sphere in the fluid. This result was surprising, due to the fact that most solvable models had predicted the VACFs would decay exponentially [12]. The exponential decay is indicative of a memory-less process; collisions of the particle decorrelate the velocity rapidly. However, as described by Alder and Wainwright, long-time tails are indicative of interesting behavior leading to persistent correlations over decades. Interesting long-time tails persist

also in the Lorentz model, but due to the simplicity of the model, cannot be explained by the same hydrodynamic considerations. Long-time tails in the VACFs of Lorentz models have been attributed to the probe's memory of being trapped in the cage formed by the surrounding stationary scatterers [8, 9, 26, 25, 67, 13, 27, 46].

Much of the work in the literature describing the long-time tails of the VACFs, has aimed to determine the functional form that describes the behavior of the long-time tails. Low-density expansions and MD simulations of the VACF give rise to decay in the form of $t^{-(\frac{1}{2}d+1)}$, where d is the dimensionality of the system in question [26, 62]. Previous work in two and three-dimensions has also been performed giving rise to the result that the VACFs decay as $t^{-d/2}$. The same work has also shown that such time tails can be predicted fairly well with mode coupling theory in three-dimensions but in two-dimensions, deviate significantly [106]. Further computational efforts have shown a power-law type decay in a two-dimensional and three-dimensional Lorentz system [8, 9, 64]. Höfling and coworkers found power-law time tails in both two and three- dimensional Lorentz models of a structureless particle diffusing through spherical scatterers [27, 46]. In this work, the transport properties, *i.e.*, the long-time tails, are shown to depend upon the density of scatterers. Correlations in the dynamics are seen to persist over decades when the density of scatterers approaches a critical density. Thus, sub-diffusive behavior can be reached when the density is increased to that critical density. Upon further increasing the density, the probe experiences geometric trapping. A complex transition from a power-law decay of long times tails to a density dependent power-law decay is observed as the scatterer density is increased. The universal decay is consistent with previous work as described above, while the intermediate decay is density dependent [46].

Another variant of the Lorentz model with surprising correlations in the dynamical behavior is that studied by Franosch *et al.* and is comprised of structureless scatterers and an infinitely thin needle probe [47, 48]. In this system, anomalous diffusion is seen when the density of scatterers increases. At low scatterer density, the translational diffusion coefficients follow the expected Enskog behavior. Upon increasing the scatterer density, the needle experiences enhanced diffusion. Moreover, the rotational motion of the needle is

suppressed and the translation motion perpendicular to the needle axis is also suppressed, leading to reptative behavior that gives rise to enhanced diffusion coefficients. Reptation is caused by the effective tubes created by the surrounding network of stationary scatterers. This behavior is similar to that observed in entangled polymer networks [23, 19]. Simulations of a thick rod in a two-dimensional array of soft disk-like obstacles shows no enhancement of the translational diffusion coefficient when plotted with respect to the reduced scatterer density, even though reptative-like behavior was observed at sufficiently large scatterer densities [74]. The rotational diffusion coefficients showed the suppression described previously by numerical simulation as well as by kinetic theory [23, 47]. A concomitant suppression of the motion perpendicular to the long axis of the rod was also observed.

The anomalous transport phenomenon in Lorentz models, gives rise to dynamical regimes that are relevant to more complex systems. There are but a few parameters that can be used to tune the dynamics of the probe in Lorentz models making the model simple, yet powerful. As described above, one such parameter, the density of the scatterers, can be used to access different dynamical regimes. Throughout this work, we explore how dynamics can be tuned by the geometric anisotropy of either the probe or the scatterer. These systems include a needle in points/spherical scatterers as well as a spherical probe immersed in needle, rod-like scatterers. Both variants give rise to interesting dynamical transitions that differ with respect to structural parameters assigned to the system.

2.5 Liquid Crystal Systems: Phase, Order Parameters, and External Fields

Liquid crystal (LC) systems are comprised of particles that exhibit anisotropy. LC molecules are noted by the geometric anisotropy of the molecule. This geometric anisotropy allows for the formation of mesophases that exist between the isotropic disorder of a liquid and the crystalline order indicative of solids. For particles with one large dimension compared to the other two dimensions, a simple range of phases can be obtained. The phases that are realizable by such particles are shown pictorially in Figure 3. The isotropic phase of nematogens is characterized by the lack of long range order in both the center of mass positions as well as alignment of the particles along some axis of the particle. The nematic

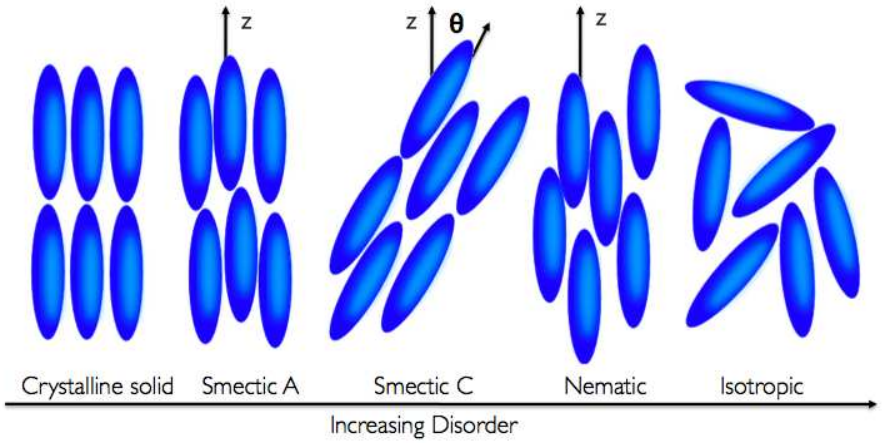

Figure 3: The liquid crystal phases available to particles where the geometric anisotropy exists due to one long dimension with respect to the other two. With increasing aspect ratio, L/D, phases with increasing order are accessible. The isotropic phase shows now long range order, the nematic shows long range orientational order with isotropic center of mass positions. Smectic phases shows ordering by the appearance of layers with isotropic center of mass positions with in the layers. Smectic phases are characterized by the tilt of the long range orientational vector. Finally the crystalline solid is observed when there is order in all three dimensions of the system.

phase is characterized by alignment of particles along some vector, known as the director, as well as the isotropic orientation of the center of mass positions. The smectic phases have additional order due to the appearance of layering. The nematogens are organized into layers with all of the particles in the layer pointing along the director. The center of mass positions within a layer are isotropic thus providing some liquid-like phase behavior. Smectic phases are often characterized by the angle of the director with respect to the normal. Such phases are accessed by increasing the geometric anisotropy, often quantified by the aspect ratio (L/D), as well as the density of nematogens.

The phase of LC systems can be characterized by the degree of long-range, orientational order. One metric often used for this task is the nematic order parameter. The nematic order parameter is defined as

$$S = \frac{1}{N}\sum_{i=1}^{N} P_2(\cos\theta_i) \ , \tag{18}$$

where P_2 is

$$P_2(\cos\theta_i) = (3\cos^2\theta_i - 1)/2 \ , \tag{19}$$

θ_i is the angle between the director, $\vec{n}$, that characterizes the nematic phase and the principal molecular axis of the nematogen i. The sum is over all of the particles in the system, N. This method works if the direction of $\vec{n}$ is known *a priori*. Usually the orientation of the director is not known and must be determined by the order tensor $\mathbf{Q}$, where

$$\mathbf{Q} = \frac{1}{N}\sum_{i=1}^{N}(\frac{3}{2}\mathbf{u_i u_i} - \frac{\mathbf{I}}{2}) \ . \tag{20}$$

The orientation of the molecular axis is given by $\mathbf{u_i}$ and $\mathbf{I}$ is the unit tensor. Diaganolization of equation 20 will produce the nematic order parameter as the largest eigenvalue. The eigenvector corresponding to this eigenvalue is the orientation of the director. Typical values for the order parameter range from zero to one, indicating an isotropic and perfect crystalline phase, respectively. LC phases range between 0.25 and 0.8. Similarly, the orientational radial distribution function can be calculated. This function indicates long-range order if the function decays to a finite value with increasing center of mass distance. The orientational radial distribution functions are defined as:

$$g_2(r) = \langle P_2(\cos\theta_{ij}(r)\rangle \tag{21}$$

$$g_4(r) = \langle P_4(\cos\theta_{ij}(r)\rangle \tag{22}$$

$$g_6(r) = \langle P_6(\cos\theta_{ij}(r)\rangle. \tag{23}$$

Here the orientational pair distribution functions are defined in terms of the Legendre Polynomials where, θ_{ij} is the angle between the direction of the molecular axis $\vec{u_i}$ of molecule i and the molecular axis of molecule j, $\vec{u_j}$, $\cos\theta_{ij} = \vec{u_i}\cdot\vec{u_j}$, and P_L is the Legendre polynomial of degree L.

Nematogenic particles that are simple spherocylinders, cylinders with a hemisphere cap on each end, are able to access LC phases even when the inter-particles interactions are hard-sphere interactions. The phase diagram for hard spherocylinders is well described in Ref. [69], The geometric anisotropy of the spherocylinders is the driver for the LC phase behavior exhibited by these systems. With increasing aspect ratio, L/D, more LC phases are accessed. The phase of the LC system becomes more ordered with increasing volume fraction and aspect ratio, producing the full range of phases depicted in Figure 3. The phase diagram with respect to aspect ratio has been well described previously in the literature [80, 34, 31, 99, 84, 69, 96]. Using the transformed equation of state for hard sphere fluids, the critical packing fraction that gives rise to orientationally ordered states before crystallization begins to occur was found [80]. Seminal computer simulations by Frenkel *et al.* [34, 31] found stable LC phases in hard fluids when the aspect ratio equals 5. A smectic phase was also observed when previously it was thought that attractive forces were necessary to gain such ordering [31]. This work was followed by additional studies focusing on the effect of changing the aspect ratio [84, 99, 96, 69].

There has also been focus on spherocylinders with more complex inter-particle interactions [35, 5, 111, 55, 17, 50, 110]. A widely used potential for non-spherical, linear molecules is the Gay-Berne potential [35]. This potential has been developed to decrease computational time when a site-site soft potential is desired. To model a linear molecule with a soft potential, it is common to employ multiple sites for a single molecule. The Gay-Berne potential allows for the assignment of a single site for a linear molecule. The potential uses parameters that allow for the determination of the anisotropy of the attractive and repulsive interactions. The phase diagram of Gay-Berne mesogens has been previously studied in the

literature [5, 111]. Using this potential, isotropic, nematic and two smectic phases have been seen in systems of soft mesogens. Also, the parameters of the Gay-Berne potential have been successfully fit to a real system to produce rich phase behavior [5]. A complex LC system has also been formed by connecting Gay-Berne mesogens with Lennard-Jones linkers to create flexible LC molecules that have also exhibited elaborate phase behavior [111]. Another soft potential is a generalization of the Lennard-Jones potential for anisotropic molecules developed by Kihara [55]. This potential has also been used to study the phase behavior of LC systems [17]. The Kihara fluid exhibits isotropic, nematic and smectic A phases [17]. There have also been studies on LC systems where electrostatic effects have been studied. Specifically, the coupling between dipoles and quadrupoles of spherocylinders have been investigated [50, 110].

Previous work has also shown interesting reentrant phase behavior for LC systems [14, 21, 81, 18, 16, 15, 42, 109, 24]. The first reentrant nematic phase was observed by Cladis in Ref. [14]. Systems of binary mixtures of LCs have exhibited reentrant phases in their phase diagram. Attractive hard ellipsoids exhibit reentrant phase behavior when the parameter that controls the strength of the attraction is suitably strong [21]. Binary mixtures of both polar and nonpolar LCs show a transition from nematic to smectic and back to a nematic phase with varying temperature [14, 81, 18] and pressure [16, 15]. In all of these cases, whether polar or not, the mixtures show a decrease in their order with respect to changes in temperature or pressure. Binary mixtures of spherical particles with cylindrical particles have exhibited reentrant phase separation [42]. It is also possible to produce reentrant behavior by synthesizing a hydrogen bonded ferroelectric LC. The odd hydrogen bonded complexes show different phase behavior than the even, where a reentrant smectic ordering is observed [109]. Reentrant smectic ordering has also been observed in ^{2}H NMR studies of an external magnetic field on chiral smectic liquid crystalline mesophases [24].

LC particles are able to be orientated by external magnetic and electric fields. This is due to the magnetic/electric anisotropy of most LC molecules. This occurs when the dielectric constant parallel to the long-axis of a calamitic LC molecule, $\epsilon_{\|}$, is significantly different than the perpendicular value, $\epsilon_{\perp}$. This anisotropy is quantified by the dielectric

anisotropy, $\Delta\epsilon = \epsilon_{\parallel} - \epsilon_{\perp}$. If this value is positive, then the permittivity parallel to the large axis is greater than the perpendicular permittivity and the LC will align with the electric field. If the dielectric anisotropy is negative, then the LC will align perpendicular to the electric field. While n the presence of an external field, an induced dipole will form in many LC molecules; however, many LC molecules possess permanent dipoles, *e.g.*, 4-cyano-4'-pentylbiphenyl (5CB) has a permanent dipole around 4.8D, thus providing a response to the external field.

The effect of external fields on the phase of LC systems has been studied widely in the literature [49, 20, 95]. If the fluctuations of the director are ignored in a completely aligned system of hard rods, the nematic-smectic transition which is 2nd order with director fluctuations, reduces to a first order phase transition [49]. The MD of polarizable spherocylinders showed a novel crystalline structure when under the influence of an external field [95]. Work on a Gay-Berne LC under the presence of an external field showed a stabilization of the smectic A phase, indicating a stabilization of long-range order as well as correlated translational order [20].

It is also possible to probe the dynamics of the director in the presence of an external magnetic or electric field. Experiments studying the dynamics of the director are often carried out using NMR and other spectroscopic techniques, where the spectrometer field is used to align the LC particles in the system. Previous work has shown the dynamics of the director of LC molecules as they reorient themselves to electric fields that are pulsed and oscillating [65, 66, 70, 7, 77]. It is possible to follow the director and measure the response time of the director with respect to the external field, as well as determine the effect of field strength. Previous theoretical work on a system of hard spherocylinders using density functional theory showed different dynamical states of the director of the nematogens. Depending upon the frequency, the nematic director experiences towing, breathing, splitting or overtaking by the external field [41]. The frequencies studied in this work are relative to a frequency, ω_0, which is roughly based on the Brownian time scale of rotation.

Due to the complex phase behavior and geometrically anisotropic nature of the nematogens in LC systems, the dynamics of a tagged probe immersed in nematogens is quite

rich [108, 58, 83, 53, 51]. When diffusion of a spherical particle is probed near the isotropic-nematic transition, anisotropy of the diffusion is observed where the diffusion parallel to the director is greater than that perpendicular to the director. Also, interesting solute size effects have been observed [108]. Diffusion of spherical tracers in colloidal, rigid rods has also been studied using fluorescence. When rod entanglement effects begin to dominate, the spherical tracer becomes efficiently trapped, thus the motion of the tagged tracer is very dependent on the pore size of the matrix formed by the rigid rods, as well as the size of the solute [83, 58]. The efficiency of trapping depends strongly upon the phase of the rigid colloidal rods. A large body of work has been completed by Dhont and coworkers studying the diffusion of spherical probes through LC suspensions of rods. This body of work speaks to the hydrodynamic effects of the fluid in which the rods and spheres are immersed as well as the effect of mesh size relative to the solute. In addition, the effects of electrostatic interactions as well as hydrodynamic screening have been considered [53, 51].

CHAPTER III

OBSERVATION OF A TRAPPING TRANSITION IN THE DIFFUSION OF A THICK NEEDLE THROUGH FIXED POINT SCATTERERS

3.1 Introduction

The diffusion of infinitely thin needles scattering elastically through obstacles has been studied widely. The dynamics of these deceptively simple models is sufficiently complex that it can capture much of the rich dynamical behavior found in physical processes of fundamental importance to polymer science and biophysics. The dynamics of a flexible needle—viz. a chain—through fixed obstacles, for example, is the basis of de Gennes' models for reptation in concentrated and entangled polymer networks [19]. It turns out to be interesting even in the limit when the needle is shorter than the Kuhn (persistence) length, and is therefore rigid and straight [48]. Examples of these models in the biophysics context include biopolymers like f-actin, microtubules and the *fd* virus [6, 39, 103, 23, 52, 53, 29, 63]. Such biopolymers form rheological systems influencing mass transport within a cell, and cellular responses to external environmental factors [6, 29, 63]. As long as the obstacles are small in comparison to the relevant dimensions of the needle, their particular geometry only affects the short time scales between collisions. At longer time scales, the frequent collisions between the rod and the scatterers smooth out the internal structure of the scatterers. It therefore suffices to consider models in which the obstacles consist of unstructured scatterers interacting through hard-sphere collisions. This simple model exhibits rich dynamical complexity while being amenable to analytical treatments and realizable by simulations on present-day computing platforms [47, 48, 107, 33, 32, 68, 90].

The equilibrium or static properties of an infinitely thin needle diffusing within an environment composed entirely of infinitely thin needles or stationary point scatterers depends strongly on the density of the scatterers. One limit occurs when the density is such that

the particles are far from each other in comparison with the length scales of the needles. Therein the needle dynamics can be characterized as a series of well-spaced independent collisions. As the density of the scatterers increases, however, strong correlations in their relative dynamics has been reported in simulations [107, 33, 32, 68, 90]. These strong dynamical correlations are observed because of the persistence of structure—viz. rigidity—in the surrounding dense network of needles or point scatterers.

Transport properties of solutes within such liquids also show interesting behavior. Frenkel and Maguire [32, 33] determined that the translational diffusion of a needle in a surrounding liquid of needles diverged with increasing density. The expected decrease in diffusion constant with increasing particle density (consistent with Enskog behavior) occurs in the dilute regime. Once a crossover density is reached, however, the translational diffusion constant begins to increase. The interesting behavior observed in the transport of the tagged needle is due to the surrounding network of needles. The dense system creates an effective Edwards tube where the particle can only travel in essentially one dimension. The rotational diffusion of the particle past the crossover density is strongly suppressed. It leads to greater diffusion through the tube parallel to the long axis of the needle, and suppressed diffusion perpendicular to the long axis of the needle. The needle essentially rattles inside of the effective tube. The dynamics of the needle is therefore dominated by the dynamics of the Edwards tube as suggested by the reptation model of de Gennes.

The possibility that entanglement effects create an effective tube for the reptation of freely-jointed polymer chains was first described by de Gennes [19]. and further developed by Doi and Edwards [23], The needle that is the focus of this work is the limit in which this chain reduces to a single Kuhn segment, and yet its dynamics can still be described in the context of reptation through an Edwards tube created by the surrounding medium. Indeed, Franosch and coworkers [47, 48] observed the transition from Brownian diffusion of an infinitely thin needle into reptation at a crossover density of the scatterers. The rotational motion of the needle also becomes suppressed as the point particle—scatterer—density increases.

The enhanced translational diffusion and suppressed rotational diffusion observed in

the numerical simulations of Franosch and coworkers [47, 48] were correctly captured by a kinetic description based on the model of Doi and Edwards [23]. This description is based upon the assumption that the diffusion constant of the needle traveling parallel to the long axis is determined by the hydrodynamics of a Brownian single rod. The latter is consistent with the assumption that the needle is infinitely thin. Independent theoretical work agrees with the observed increase in the translational diffusion constant with increasing network density [79, 68]. Moreno and Kob [74] described the dynamics of a rod with finite thickness immersed in a glass of discs interacting through soft potentials using numerical simulations, kinetic theory and reptation. They observed the transition between simple diffusion at moderate densities and diminished diffusion dynamics at higher densities. The latter is dominated by the excluded volume effects leading to tubes through which the needle now diffuses slowly. The origin of this diminished diffusion regime is presumably the glassy structure of the solvent, whereas Franosch and coworkers [47, 48] see an enhanced diffusive regime originating, in part, from their choice of a random media.

The aim of this work is to determine the effect of the needle thickness on the transport phenomena of a rigid needle-like particle diffusing in a simple Lorentz model consisting of randomly placed scatterers. In the limit that the needles are infinitely thin, the only relevant length scale is the ratio of the needle length to the average inter-scatterer distance [6, 39, 103, 23, 52, 53, 29, 63]. As the particle length increases, the rotational motion is further suppressed and reptative motion dominates the dynamics. The question driving this study is whether this mechanism persists if the needles are no longer infinitely thin. In generalizing the structure of the needle to have a thickness, we necessarily add an additional structural parameter: the aspect ratio of the length to the thickness of the needle. This structural parameter introduces the possibility of a competition between the enhanced diffusive behavior seen in the dynamics of infinitely thin needles through random scatterers, and the diminished diffusive behavior seen in the dynamics of thick needles through glassy scatterers. Anticipating the results shown below, the usual diffusive regime has been observed at low scatterer density. When the scatterer density is very large or the needle

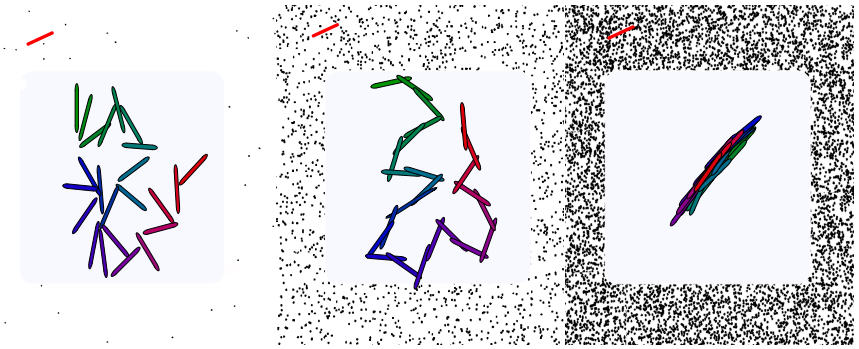

Figure 4: Representative trajectories of the three regimes observed by simulation for the dynamics of the needle through scatterers of varying density. The point scatterer density increases from left to right. The left panel illustrates standard diffusion. The middle panel illustrates reptative dynamics with short-time correlation in the linear motion. The right panel illustrates a localized regime in which the needle is trapped for long times. The particles are colored with respect to time, changing smoothly from green at t_0 to red at t_f. These representative trajectories have a times step of approximately 1 fs and run for 25 fs. The scatterer densities are shown in the margins of each panel. The scatterers are not shown at the center of each panel and the needles have been magnified for clarity. The length of the actual needle in comparison to the scatterers is shown in the upper left hand corner. The width of the needle is $\frac{1}{20}^{\text{th}}$ of the average obstacle distance shown in the right most panel.

width is very large, a diminished diffusive regime emerges. In this regime, the needle experiences caging effects as seen in glassy environments because of the apparent localization of the needle. At intermediate scatterer densities, a reptative regime emerges leading to enhanced diffusion. Therein, frequent long-distance hops dominate the dynamics as the needle moves primarily along its primary axis. All three of these regimes are illustrated in Figure 4 using representative hand-drawn trajectories. The dynamics of the needle is also modified because the aspect ratio of the length to the thickness of the needle introduces a competition between head-on collisions and side collisions as the driver of reversals in the velocity of the needle. In the work by Höfling *et al* [47], head-on collisions cannot occur and such reflections are due only to the rattling of the infinitely thin needle inside the Edwards tube. However, there still remains the possibility that the needle thickness can lead to trapping (or caging) not possible in the case of infinitely thin needles. Indeed, earlier theoretical work by Yoshizaki and Yamakawa [112] did admit the possibility that such reflections should persist with particle thickness but suggested the effect of the end

cap on transport would be relatively small.

The aim of this work is therefore the elucidation of the dynamical regimes exhibited by a needle through obstacles with respect to the needles thickness. Molecular dynamics simulations have been done on a rigid needle-like particle in an isotropic array of stationary points interacting via a hard sphere potential. The needle-like particle is a two dimensional cylinder with semicircular caps on each end as described in Sec. II. The thickness of the needle is varied with respect to the average length between point particles, ϵ. The resulting transport of the needle-like particle is shown to strongly depend upon the excluded area of the needle in Sec. III.

3.2 Model and Simulation Details

The Lorentz model we consider is comprised of a two-dimensional isotropic array of stationary point scatterers. These obstacles are distributed uniformly on the xy plane and periodic boundary conditions are employed. An ensemble of different realizations of the scatterer positions were sampled at each density. The simulations are performed within a periodic square box with sides measuring 100Å by 100Å. The tracer is a needle-like rigid rod with a semi-circular cap at each end. The thickness of the particle (the width of the cylinder and diameter of the semicircular cap) is σ. The average distance between point scatterers is $\epsilon = n^{-1/2}$, where n is the number density. The longest needle considered is 6Å long. The simulation box is at least 16 times longer than the needle. This should be long enough to remove finite size effects in the dynamics, but different size boxes were simulated so as to confirm their absence. The reduced density of the point scatterers is $n^* = nL^2$ where L is the length of the rod. The rod interacts with the point particles via a hard potential. The simulations are carried out at constant energy corresponding to an equipartition temperature, 300K. (This sets the time scale in physical units but is otherwise arbitrary.) Because the thick needle interacts with the static particles via a hard potential, the overall total velocity of the needle does not change, though the resolved velocity components do fluctuate.

The integration of the equations of motion for this model system was carried out using

a Fortran code written by us. The needle and the obstacles—the point scatterers—collide through a hard-wall potential defined at the surface of the tracer. In between collisions, the needle is propagated as a free particle through the well-known exact expressions,

$$\mathbf{r}(t+\tau) = \mathbf{r}(t) + \mathbf{v}(t)\tau \tag{24a}$$

$$\theta(t+\tau) = \theta(t) + \omega(t)\tau \ , \tag{24b}$$

where $\mathbf{r}(t)$ is the center of mass position, $\mathbf{v}$ is the linear velocity of the center of mass, and ω is the rotational velocity. The propagation was effectively integrated using an event-driven algorithm. However, the data collection was facilitated by stopping the integration at constant time intervals. The time step of the interval was chosen to be on the order of the mean collision time at a given density. As a consequence, typically only one or a few events occurred in between the time intervals and this also helped speed up the performance of the numerical integrator. The time step was taken to be 0.5 femtoseconds for the densest systems and conservatively 1.0 femtoseconds, otherwise.

Collisions are detected by determining the closest point between the needle tracer and the point scatterer. Once that point is known, the velocity of the point on the tracer closest to the scatterer is determined using

$$\mathbf{v}_p = \mathbf{v}(t^<) + \omega \mathbf{r}_p^\perp \tag{25}$$

where $\mathbf{v_p}$ is the velocity of the vector, $\mathbf{r_p}$, from the center of the needle to the point on the needle closest to the scatterer, and $t^<$ is a time just before the collision. The perpendicular operator, denoted by the superscript $\perp$, applies a 90° counterclockwise rotation to $\mathbf{r}_p$. The time to collision between the needle and each particle can be deduced from the solution of Eq. 24 with the appropriate velocities for a distance corresponding to contact between them. Collision detection is simplified within the current model of the needle because of the use of semi-circular end caps. The closest contact between the thick needle and the point scatterer occurs when an infinitely thin needle and a point scatterer are separated by the diameter, σ, of the thick needle.

Post-collision particle dynamics were determined using an impulse based algorithm. Collisions were treated as elastic, frictionless and instantaneous. The impulse of the collision

was determined and post-collision velocities were calculated by updating the pre-collision velocities by the impulse in the direction of the normal to the collision. We follow the the algorithm of Ref. [3] for the collision between hard spheres with only a few minor modifications to account for the lack of spherical symmetry in the colliding particles. The post-collision center-of-mass and rotational velocities are

$$\mathbf{v}_2 = \mathbf{v}_1 + \frac{j}{m}\mathbf{n} \tag{26a}$$

$$\omega_2 = \omega_1 + \frac{r_p^{\perp} \cdot j\mathbf{n}}{I} \, , \tag{26b}$$

where $\mathbf{v}_1$ and ω_1 are the respective pre-collision center-of-mass and rotational velocities, m is the mass of the needle, and $\mathbf{n}$ is the normal vector of the collision. The impulse j is determined by

$$j = \frac{-2\mathbf{v} \cdot \mathbf{n}}{\frac{1}{m}(\mathbf{n} \cdot \mathbf{n}) + \frac{1}{I}(r^{\perp} \cdot \mathbf{n})^2} \, , \tag{27}$$

where I is the moment of inertia.

In the first set of simulations, the particle width is varied with respect to the average distance between point scatterers, ϵ, where $\epsilon = n^{-1/2}$ while the density is held constant at $n^* = 175$. The needle thickness σ is varied across several representative values, $\epsilon/3, \epsilon/5, \epsilon/10$, and $\epsilon/20$ where $\epsilon = 0.37$Å at the chosen density. In these simulations, the length of the needle is set at $L = 5\text{Å} + \sigma$ and the aspect ratio L/σ of the needle varies with its thickness. The length of the rod is much shorter than the length of the simulation box in order to avoid spurious correlations in the dynamical properties of the system.

In the second set of simulations, the needle thickness is set to a constant value, $\sigma = 0.013$Å, and the density of the point scatterers is varied. This value of σ is small enough that the ratio σ/ϵ is always less than $1/20$ for the chosen densities, and hence the needle can, on average, reptate between any two scatterers. (The value of σ has been chosen such that it is one-twentieth of the size of ϵ in the densest case studied here, $n^* = 350$.) In the third set of simulations, the ratio of the rod thickness to the average spacing between scatterers is held constant as the density of point scatterers is also varied. This ratio is taken to be $\sigma = \epsilon/20$ where ϵ is a function of the reduced density, n^*. The needle length remains at $L = 5\text{Å} + \sigma$ corresponding to an aspect ratio that varies from 10 to 385 for the

reported range of dilute to dense obstacles.

3.3 Results and Discussion

3.3.1 Trapping Transition as a Function of Needle Width

In introducing the needle width as an adjustable parameter, there now exists two regimes that will not be considered further. The first regime occurs when the width is sufficiently larger than the needle length that the diffusing particle structure is oblate. The limit when the interior cylinder vanishes leads to a model in which the diffusing particle is a sphere scattered by point obstacles. It is not of interest here because this limit is well understood in the literature [25, 67, 9, 26, 62, 46, 27, 13]. The more general oblate case within this limit will also not be a focus of the present work because its topology is not consistent with a needle. The second regime occurs when the width is shorter than the needle length but on the order of the mean inter-particle distance ϵ between the point obstacles. In this case, the needle is essentially trapped at all times. Presumably, this trapping can also effectively occur even at widths smaller than σ. Thus the focus of this work is the nontrivial regime in which the needle widths are small enough to allow transport through obstacles. We first explore this crossover regime as a function of the reduced obstacle density, n^*.

Figure 5 shows a series of trajectories that exhibit competition between diffusion and entrapment at relatively large number density of $n^* = 175$. In panels (a) through (d), the width of the thick needle is set to $\epsilon/3$, $\epsilon/5$, $\epsilon/10$, and $\epsilon/20$, respectively, where ϵ is the average distance between obstacles. The expected dynamics includes periods of reptation of the needle through dense obstacles —as seen at early times in all of these representative cases— staggered with periods of caging. The needle does experience vibrations in the translational diffusion although it is hard to see in Figure 5 due to the small scale of the vibrations when entrapment occurs. Entrapment was also seen in trajectories —not shown— after significant periods of diffusion. Eventually, the needle escapes from these cages and diffusive behavior is regained. As the particle width is decreased, entrapment becomes less prevalent and plays a reduced role in the overall diffusive behavior of the center of mass of the needle. The number of trajectories of a given time period that exhibit this caging

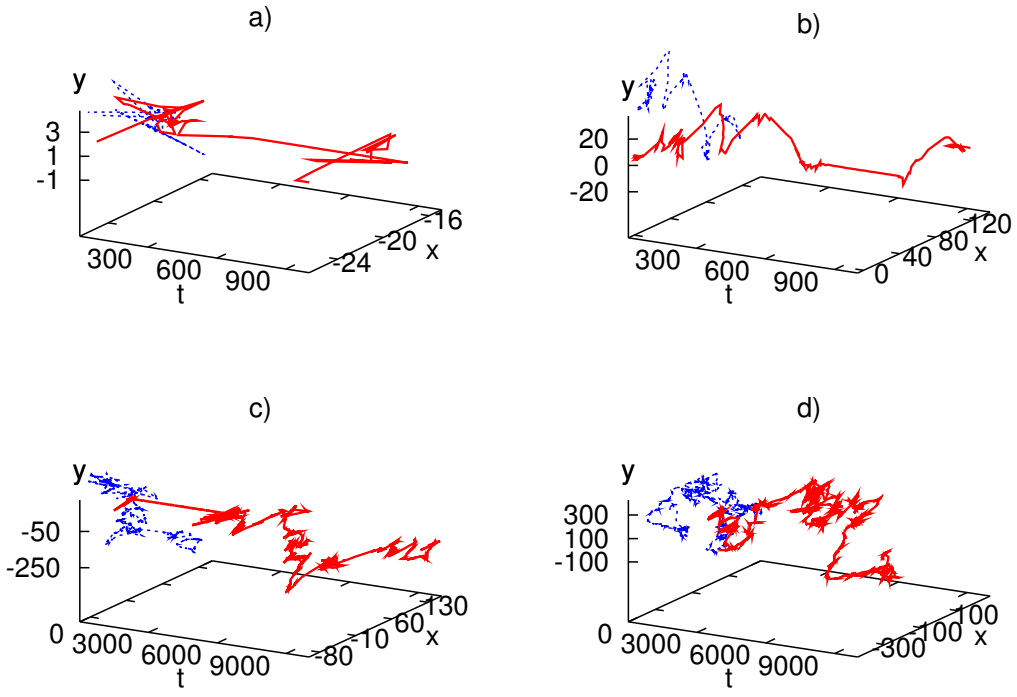

Figure 5: Representative trajectories are shown for the fixed obstacle density discussed in Sec. 3.3.1 at various values of the particle width. The solid curve tracks the time dependence of a trajectory while the dotted curve exhibits the projection of the trajectory onto the xy plane. The particle widths are $\epsilon/3$, $\epsilon/5$, $\epsilon/10$ and $\epsilon/20$ for the four cases shown above. At the largest thickness, frame (a), the trajectory exhibits a series of reptative periods followed by an extended trapping, etc. As the width of the particle decreases, from frames (b) to (d), the number of trajectories that exhibit entrapment decreases, entrapment times decrease, and the longest particle moves occur during periods of reptation.

behavior also decreases dramatically.

Table 1: Statistics over 500 trajectories of the needle with each integrated for a total time of 1000 ps are shown here for varying needle widths: the percentage in time that the needle is "trapped" in the sense that the needle doesn't move more than 0.02 Å in each direction within a given time step, and the percentage of trajectories which exhibit at least one such trapping period. Convergence in these values (up to the displayed two significant digits) was verified by ensuring that the diffusion in the x and y directions is converged to the reported values within 5% or better. Each calculation required a total of 150 CPU hours spread across twenty 3.2 GHz Intel Xeon cores.

σ	% time	% trajectories
$\epsilon/3$	61	98
$\epsilon/5$	32	56
$\epsilon/10$	80	12
$\epsilon/20$	6.4	16

In larger density systems and for relatively large needle thickness, transport is seen to exhibit competition between reptation due to suppression of rotation and also slow dynamics caused by particle caging due to the excluded area. As the particle thickness is decreased in these large density systems, the reptative dynamics begins to dominate and an overall increase in the translational diffusion of the particle is observed. The corresponding statistics for an ensemble of trajectories is provided in Table 1 for various choices of the the particle width. As in the trajectories in Figure 5, the average inter-particle distance between obstacles is $\epsilon = 0.37$Å corresponding to the choice of reduced density, $n^* = 175$. As the needle thickness decreases, the entrapment time significantly decreases as well as the relative percentage of trajectories that exhibit trapping.

Rotational and translational diffusion constants for the needle-like particle with a density of $n^* = 175$ are shown in Figure 6. An overall increase in the translational diffusion constants with decreasing particle width is observed, and a slight decrease in rotational diffusion is also observed (even though rotational motion is very suppressed at this density). To compare the differences in the rotational motion due to the excluded area of the particle, the mean-square angular displacement (MSAD) and the rotational correlation function $C_1(t)$ are calculated. In Figure 7, the MSAD of the same system of $n^* = 175$ with a varied particle thickness shows

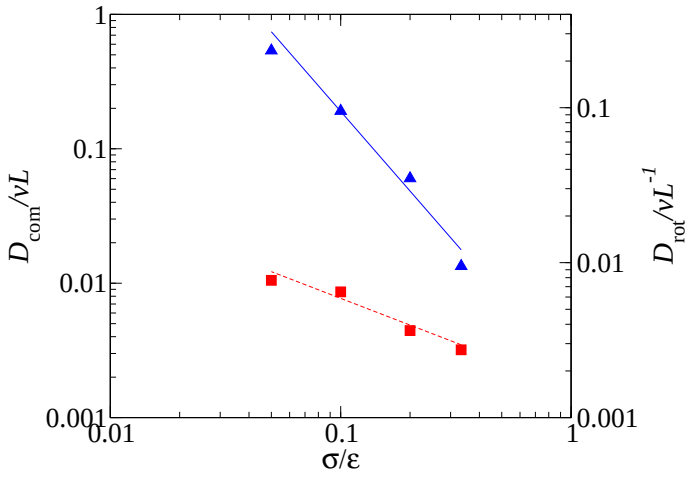

Figure 6: Dimensionless translational and rotational diffusion constants, $D_{\rm com}$ ($D_{\rm rot}$) with respect to particle width are shown in triangles (squares) with ordinates marked by the left (right) axes labels. The lines are power-law fits to the data with slopes of -2 and -0.5 for translational and rotational coefficients respectively. The diffusion constants have been scaled, as indicated, by the physical parameters following Höfling et al [47]. Each point has been generated by sampling 500 trajectories, and required 150 CPU hours spread across twenty 3.2 GHz Intel Xeon cores. The diffusion constants have error bars within 5% percent assuming the standard error of the mean.

that at short times rotational motion is diffusive for all particle widths. As time progresses, the thicker particle systems start to show slight sub-diffusive behavior. The orientational correlation function $C_1(t) = \langle \hat{u}(t) \cdot \hat{u}(0) \rangle$ is shown in Figure 8. The particle width does not significantly affect the correlations of the orientation of the particle with respect to the dimensionless time, t/τ_{coll}. All four particle widths tested show similar relaxation at short time. The correlations are consistent with the rotational diffusion constants. Thicker particles show more correlation of particle orientation at longer times due to particle caging.

Another figure of merit providing insight into the effect of excluded area is the velocity autocorrelation function (VACF). The VACFs for four chosen particle widths are shown in Figure 9. The initial decay in the VACF decays at longer time scales with decreasing particle thickness because of the decreasing role of the head-on collisions. The thickest needles, however, exhibit a non-exponentially decaying correlation several decades of the collision time later. This is a result of the caging of the needle by the obstacles. The

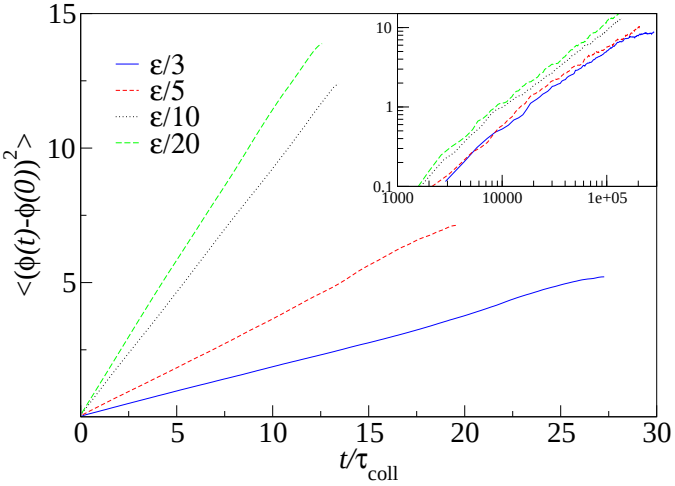

Figure 7: The mean-square angular displacement, $\langle \delta\phi^2(t) \rangle$, is displayed as as a function of time for ensembles of integrated trajectories with varying needle widths, $\sigma \in \{\epsilon/3, \epsilon/5, \epsilon/10, \epsilon/20\}$. The x-axis is divided by 10000. The inset is the same data on a log-log scale. In each case, the time has been scaled by the corresponding mean collision time τ_{coll} which was found to be equal to 0.003 ps, 0.005 ps, 0.006 ps and 0.007 ps, respectively, through a numerical average of the collision times in the sampled trajectories.

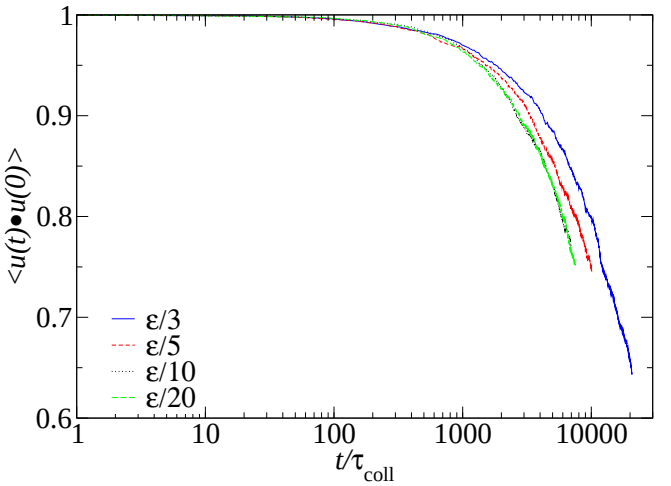

Figure 8: The orientational correlation function $C_1(t)$ with respect to dimensionless time, t/τ_{coll}, is shown for the four needle widths as in Figure 7.

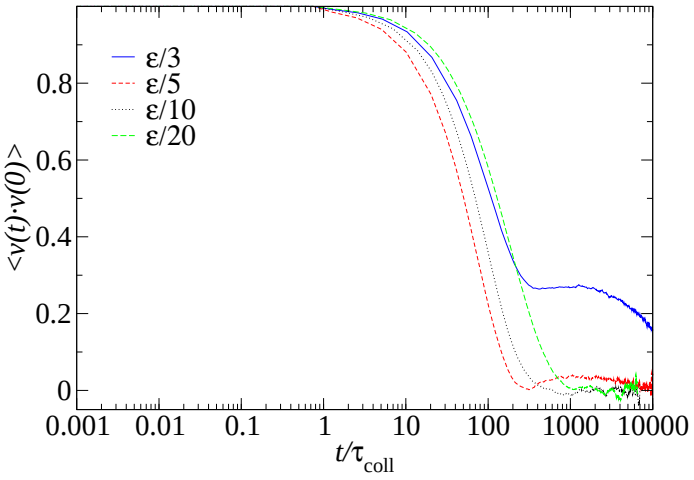

Figure 9: Semi-log plot of the velocity autocorrelation function with respect to time. The time has been scaled by the mean collision time. Correlations in thick needles persist for long times showing entrapment while thinner needles show exponential decay.

effect is curtailed—though not shown— as the needles become longer —or equivalently the obstacle density increases. This is easily understood. With the increasing length of the needle, the collisions between the side of the needle and the obstacles become the dominant mechanism. Consequently, the effect of head-on collisions is suppressed, and the non-exponentially decaying long-time correlation is lost.

3.3.2 Crossover Regimes as a Function of Obstacle Density

When the needle width is small enough that the needle tends to escape every would-be cage despite its non-zero thickness, then it can be expected to exhibit long-range transport. It is then possible to explore whether the thick-needle dynamics correspond qualitatively (or quantitatively) to those seen for infinitely-thin needles diffusing through stationary point scatterers by Höfling et al [48], for thick needles through glassy obstacles by Moreno and Kob [74], or perhaps some combination of these. To this end, a fairly small particle width has been set —*i.e.*, $\sigma = \epsilon/20 = 0.013$— corresponding to the highest density — $n^* = 350$— explored in this work. This particle width is small enough that the needle exhibits computationally-measurable translational and rotational diffusion over a broad set

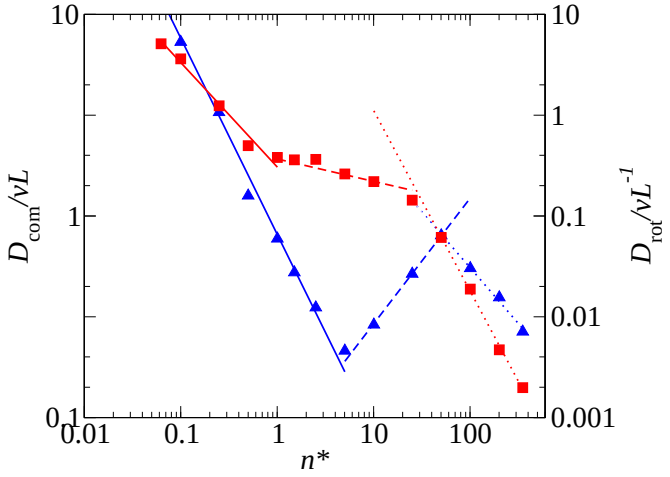

Figure 10: Log-log plot of the diffusion constants for the translational and rotational motion versus the reduced particle density for $\sigma = 0.013$. Triangles are the translational diffusion constants (scale on the left) and squares are the rotational diffusion constants (scale on the right). D_{com} is normalized by vL and D_{rot} is normalized by $v^{-1}L$. Solid lines indicate the expected Enskog behavior, slope of -1, while the dotted lines show power-law behavior with slopes given in the text. The expected Enskog behavior for low density is observed in both translational and rotational motion. Enhanced translational diffusion is accompanied with suppressed rotational motion. An intermediate region between these regimes is observed.

of obstacle densities. As the obstacle density decreases, the fixed particle width becomes a decreasingly smaller fraction of the average obstacle spacing ϵ and their dynamics are expected to be increasingly similar to those for an infinitely thin needle scattering through point obstacles.

The diffusion constants in Figure 10 exhibit the expected Enskog behavior at low densities for both the rotational and translational motion, $D \propto (1/n)$. The transition in the center-of-mass translational motion to enhanced diffusion occurs here at a particle density of $n^* \approx 5$. This transition was observed by Höfling et al [47] and the enhanced diffusive transport was attributed to reptative motion of the needle. They did not, however, see the second transition at $n^* \approx 110$ in which the transport exhibits diminished diffusion. This third dynamical regime, occurring at very high densities, is a result of caging of the needle

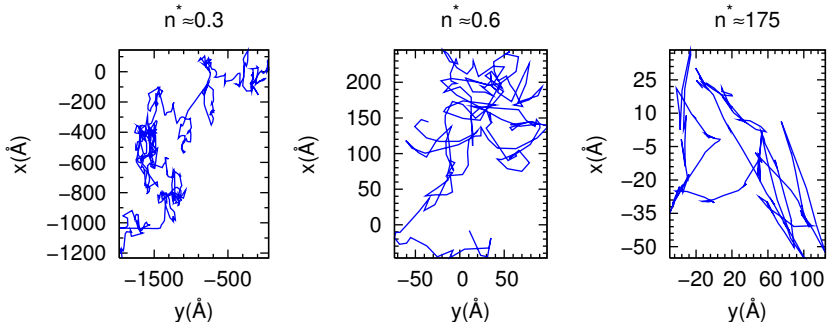

Figure 11: Representative trajectories of the center of mass (com) of the needle in the xy-plane are given in the top panel. A clear transition from diffusive behavior that occurs at low densities to reptative motion at moderately high density is observed. Density increases from left to right. Results shown are from simulations of a needle where $\sigma = 0.013$Å.

as a consequence of head-on collisions between the thick needle and the obstacles. With respect to the rotational diffusion constants, an intermediate regime occurs between when the mean scatterer distance, ϵ, is approximately half of the needle length, L, and when $n^* \approx 80$. At lower densities, we observe the expected Enskog behavior, and at higher densities, we observe the caging effects also seen by Höfling et al [47]. In the intermediate regime, there is presumably a competition between these effects as a consequence of the particle width.

The translational diffusion constants follow a power law,

$$D_{\text{com}} \propto n^{\zeta} \,, \tag{28}$$

at densities just above the crossover density, $n^* \approx 5$, for the exponent $\zeta = 0.63 \pm 0.01$. This exponent observed here is smaller than that determined by Höfling *et al.* [47]. This is due to the addition of needle width in the present model. They saw a larger exponent of $\zeta = 0.80 \pm 0.05$ with a crossover density of $n^* \approx 5$, due to larger diffusion constants because of the ease in which the infinitely thin particle can move through the stationary points. A slight decrease in the diffusion constants at all densities is observed because of the addition of collisions with the end cap of the particle, once again showing the influence of needle width on transport. The enhanced motion in both cases is due to diffusive motion becoming reptative. As scatterer density increases, the motion of the needle perpendicular to the long axis becomes suppressed as well as the rotational motion of the needle. The transition from diffusive to reptative motion with respect to density is shown in Figure 11. Large scatterer

density leads to the needle rattling in an effective tube. When scatterer density begins to increase to the point that caging effects begin to dominate, the translational diffusion also follows the power-law of equation 28 with $\zeta = -0.55 \pm 0.03$.

The rotational motion follows the expected Enskog behavior with respect to density at low densities. The intermediate regime of the rotational motion occurs around the crossover density of $n^* \approx 5$. The rotational diffusion at densities larger than the crossover density scale as $D_{\text{rot}} \sim n^{-2}$ which is the same power-law exhibited in the work of Höfling [47] and also the Doi-Edwards scaling prediction for infinitely thin needles [23].

3.3.3 Persistence of crossover regimes with larger needle widths

The nontrivial width of the needle was seen in the previous section to give rise to a new crossover regime when that width is fixed at a very small size. In this section, we choose to keep the ratio of the width size to mean particle distance, σ/ϵ, fixed as the density of obstacles is varied. The ratio is set to 1/20 because as seen in Sec. 3.3.1, that is small enough that the needle dynamics is not dominated by entrapment at nearly all densities. Nevertheless, the data in Figure 12 provide evidence that the transitions—though now softened—seen in Sec. 3.3.1 still persist. The translational and rotational diffusion constants follows the expected Enskog behavior with respect to density at low densities, $D \sim (1/n)$. At the crossover density, $n^* \approx 7.5$, the particle begins to experience an increase in the diffusion constant which is attributed to reptative transport. This crossover density is larger than that obtained for the very thin needles in Sec. 3.3.1 and also for infinitely thin needles [47]. As density is further increased, a decrease in the translational diffusion coefficient is observed. This is due to the competition between the slow dynamics and caging resulting from the head-on collisions, and the motion of the effective Edwards tube. A downturn for the density is observed at a crossover density near $n^* \approx 175$ which is larger than that of the data reported above. In both cases, the downturn is caused by caging due to collisions with the needle end cap. The thinner needles of the previous section evidently lead to a transition at a lower density. We conjecture that the thinner widths allow the needles to move faster between non-trapping obstacles, and thereby find cages more easily.

Such cages must be sufficiently confining to trap the thin needle, and presumably are able to trap it for longer caging times.

The translational and rotational diffusion constants in each of the three regimes illustrated in Figure 12 can be described by power laws with respect to the reduced density. The low density behavior of both rotational and translational diffusion agrees with that observed by Höfling et al [47] as does the suppressed rotational motion. When the crossover density at $n^* \approx 7.5$ is reached, the asymptotic behavior of the translational diffusion constants follows a power-law, $D_{\rm com} \propto n^{\zeta}$, where $\zeta = 0.33 \pm 0.02$ for moderate densities. The downturn observed after $n^* \approx 175$ also follows a power law but with $\zeta = -0.45 \pm 0.07$. Both of these exponents are smaller than those obtained by Höfling *et al.* [47] and the results described previously. A table comparing all of the exponents is given in Table 2. The decrease in the exponents for enhanced translational motion is due to the needle width and the associated end-cap collisions. At moderate densities, we observe a range of densities —which we call a plateau region— in which the rotational diffusion constants decrease with a markedly smaller exponent with respect to increased density. This plateau region coincides with a flattening out of the translational diffusion constants near the crossover density of $n^* \approx 7.5$. The plateau region in the rotational diffusion constants observed in this work was not seen in the dynamics of infinitely thin needles. Interestingly, it persists over a wider range of densities and with larger downward slope, in the case of the thicker needles.

3.4 Concluding Remarks

In this work we have investigated the competition between caging effects and reptation in a system of a thin needle-like particles scattered by a fixed random array of obstacles. Reptative dynamics dominates the diffusion if the width of the particle is not too large as compared with the average distance between scatterers. If the needle width is fairly small (but nonzero), then the the observed dynamics is qualitatively similar to that seen for infinitely thin needles within certain regimes. We found that enhanced diffusion is observed at a crossover density of $n^* \approx 5$. We also found the emergence of a transition at $n^* \approx 110$ not seen in the dynamics of infinitely thin needles that is due to caging effects resulting from

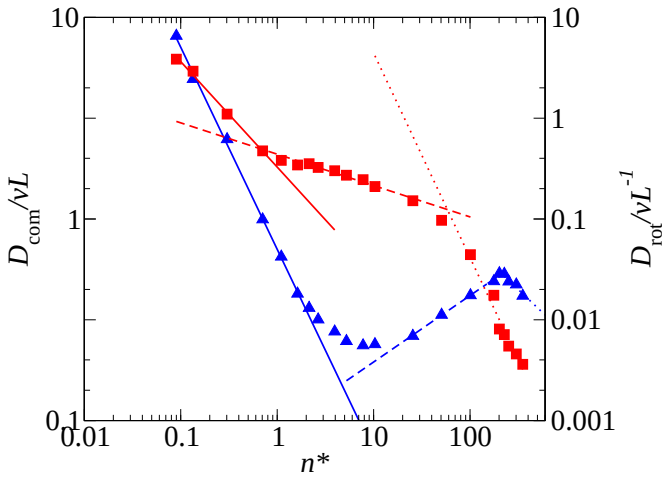

Figure 12: Log-log plot of translational (triangles) and rotational (squares) diffusion constants for $\sigma = \epsilon/20$. Translation diffusion constants scale is on the left, and the rotational diffusion constants scale is on the right. Enhanced translational transport is seen when rotation is suppressed. $D_{\rm com}$ is normalized by vL and $D_{\rm rot}$ is normalized by $v^{-1}L$. Solid lines indicate slopes of -1, while dotted lines show power-law behavior described in the text.

nontrivial particle widths. We have also shown that when particle width is set as a function of scatterer density, a gradual change from the expected Enskog behavior to an increase of translational diffusion and suppression of rotational motion at a crossover density, $n^* \approx 7.5$ occurs. This gradual divergence of the diffusion coefficients is not observed for infinitely thin needles and can be attributed to needle thickness. End cap collisions cause a lowering of the both the translational and rotational diffusion constants compared to the infinitely thin needle, however enhanced translational diffusion is observed due to the reptative behavior of the needle. We also observe a second, higher crossover density, $n^* \approx 175$, in which the reptative motion of the particle is in competition with slow dynamics created by particle caging effects which is not observed unless the particle is given some width.

In summary, the present work indicates that the dynamics of thin needles of nontrivial thickness scattered by randomly placed obstacles experiences three nontrivial regimes. The low density regime is the standard Enskog diffusion, and has been seen earlier in other work. The intermediate density regime gives rise to enhanced diffusion as seen earlier by

Table 2: The scaling exponents for the translational—with respect to the center of mass (com)—and rotational (rot) diffusion with respect to n^* are shown. The constant σ case corresponds to the simulations displayed in Figure 10 and discussed in Sec. 3.3.2. The non-constant σ case corresponds to the simulations displayed in Figure 12 and discussed in Sec. 3.3.3. While Höfling *et al* [47] saw only two regimes, we see three regimes in the current work. In all cases, the typical Enskog behavior is seen at low n^*. At large n^*, we attribute the exponents observed in this work to two separate regimes as indicated in the table, but do not explicitly attribute the exponents of Höfling *et al* [47] to either regime. (See text for the interpretation.)

com	low n^*	enhanced n^*	caging n^*
$\sigma = 0.013$	-0.99 ± 0.01	0.63 ± 0.01	-0.55 ± 0.03
$\sigma = \epsilon(n^*)/20$	-1.00 ± 0.02	0.33 ± 0.01	-0.45 ± 0.07
Ref. [47]	-1	0.80 ± 0.05	
rotation	low n^*	plateau n^*	caging n^*
$\sigma = 0.013$	-1.00 ± 0.04	-0.23 ± 0.05	-1.8 ± 0.1
$\sigma = \epsilon(n^*)/20$	-1.04 ± 0.05	-0.31 ± 0.02	-2.0 ± 0.2
Ref. [47]	-1	-2	

Höfling et al [47] for the case of infinitely thin needles. The large density regime gives rise to suppressed diffusion as seen earlier by Kob and Moreno [74] in the case of glassy obstacles scattering thick needles. The present work thus reconciles both of the earlier observations within a single model governed by two relevant order parameters: the ratio of the length of the needle to the typical obstacle spacing, and the ratio of the width of the needle to the typical obstacle spacing.

It also forms a basis for future work using particle-like models to describe the dynamics of solutes diffusing through driven anisotropic solvents. Earlier work [45] used reduced-dimensional non-stationary Langevin models [43, 44] to suggest the possibility that solutes could be driven to diffuse in preferred directions. The existence of several transport mechanisms for thick needles diffusing through obstacles suggests that dynamics of these liquid crystals may be even richer.

CHAPTER IV

ON THE ABSENCE OF ENHANCED DIFFUSION IN THE DYNAMICS OF A THICK NEEDLE THROUGH THREE-DIMENSIONAL FIXED SCATTERERS

4.1 Introduction

A large number of complex systems—involving non-spherical analytes dissolved in structureless solvents—can be represented through a simple model involving a thin needle scattering through fixed obstacles. Though seemingly simple, it involves a competition between dynamical events occurring at various length and time scales as described in Chapter 3. The ability of the needle to penetrate through the obstacles depends on its width in comparison with the average separation of the fixed obstacles. The space-filling of the needle within the obstacles depends on its volume in comparison with the obstacle density. The correlation in properties of the needle transport in turn depends on the position correlation of the scatterers. The resulting dynamics is thus nearly as rich as has been seen in other recent examples of particles moving in non-stationary solvents [43, 98]—e.g., in thermosetting polymerization, [44] surface diffusion, [73, 71] swelling [86, 85] and driven colloidal suspensions [45], dissipated molecular wires, [72] and nanorods sliding across a surface [87]. Indeed, the fact that the dynamics of the needle can exhibit a wide range of coherence in the absence of a dynamic complex environment is perhaps surprising.

The wide range of dynamical regimes for the diffusion of a needle through fixed-point scatterers has been seen in a variety of physical systems in polymer science and biophysics [47, 74, 104]. The reptative behavior of a flexible polymer was described by de Gennes in concentrated entangled polymer networks [19]. Reptation persists even in the limit that the polymer is a rigid needle—viz, when it is rigid, straight and shorter than the persistence length (Kuhn length). The reptative motion of particles in a liquid comprised of rigid needles is a result of entanglement effects that create effective tubes for the

particle transport, as was first described by Doi and Edwards [23]. Therein, they found that the reptative motion persists even in the limit of rigid particles such as is the case for the needles that are the focus of the present work. As stated previously, models in which reptative, entangled polymers are biologically relevant include f-actin, microtubules and the *fd* virus [6, 39, 103, 23, 52, 53, 29, 63]. Biopolymers, such as these, are important in mass transport within a cell and cellular responses to external environmental factors [6, 29, 63]. Diffusion of macromolecules through stationary media, like porous hydrogels, show reptative behavior. The pore-size of the gel with respect to the aspect ratio of the diffusing molecule as well as the conformation of the molecule determines whether or not reptation will take place [36, 22, 1].

Frenkel and Maguire [32, 33] found that the translational diffusion of a needle in a surrounding liquid of needles diverges with increasing density. At very low densities, the structure of the scatterers does not influence the long-time dynamics of the needle significantly, and leads to the usual Enskog behavior. As the density increases beyond a critical value, the diffusion coefficient of the needle increases with increasing density. This is due to the emergence of effective tubes, the so-called Edwards tubes, created by the surrounding network of needles. The Edwards tube arises because of the severely hindered rotational motion along with hindered motion perpendicular to the needle. This effective rattling inside a tube was first described by de Gennes [19] and further developed by Doi and Edwards [23]. The presence of strong dynamical correlations due to reptative behavior was also confirmed in studies of infinitely thin needles [68, 90, 107].

Further numerical studies of infinitely thin needles in a stationary, random, two-dimensional array of scatterers have also been shown to give rise to long-range dynamical correlations. Höfling *et al.* showed that a rigid infinitely thin needle in a network of points does in fact show suppressed rotational diffusion and reptation after a critical density is reached [47, 48]. Their findings are in agreement with the kinetic description theorized by Doi and Edwards [23]. The latter is based on the assumption that the diffusion constant of the needle parallel to the long axis is determined by the hydrodynamics of a free Brownian rod in which head-on collisions play no role, i.e. the needle is infinitely thin. Höfling *et al.*'s observation

that the translational diffusion coefficients increased with increasing scatterer density is also consistent with earlier theoretical work [79, 68].

When the needle thickness is taken to be finite, several dynamical transitions emerge as a function of the obstacle density relative to the needle dimensions. Moreno and Kob [74] described the dynamics of a rod of finite thickness immersed in a glass of soft discs. Using numerical simulations, they observed a transition between simple diffusion at moderate densities and diminished diffusion at higher densities. Excluded volume effects of a needle with finite thickness appear to give rise to the observed diminished diffusion. The results given in Chapter 3 and also in Ref. [104] show this regime in the dynamics of a needle with finite thickness diffusing through a 2-dimensional array of random points. We attributed this slow regime to spatial regions in which the particle appears to be localized for extended stays—viz. traps—and therefore renamed it a trapping transition. Unlike Moreno and Kob, [74] however, we [104] observed an intermediate regime akin to that seen by Höfling *et al.* [47, 48] exhibiting enhanced translational diffusion. We attributed it to the onset of reptative-like motion after a critical density is reached. The needle presumably diffuses unabatedly along the parallel axis of an effective Edwards tube. In this enhanced-transport regime, the needle finds itself in longer (but thinner) tubes as the density increases which thereby increasingly enhances its translational diffusion.

The regimes seen thus far in Chapter 3 and Ref. [104] took place in two-dimensions. The question that remains is which dynamical behaviors persist in an analogous three-dimensional system. In the limit of an infinitely thin needle scattering off of infinitely thin points, the answer is trivial. Namely, the needle moves ballistically essentially forever because the points span a space of measure zero —regardless of the value of their finite density— giving rise to no collisions. If, instead, an additional mean-field Brownian solvent is added (as in the two-dimensional work by Franosch et al [30]), the needle will simply follow Brownian dynamics with the same diffusion constant regardless of the scatter density. Thus, the introduction of a finite thickness is essential both in making the three-dimensional system nontrivial, and in allowing this model to be more readily physically realizable. It is also notable that the diffusion of spherical probes through Lorentz models of stationary

needles or through moving needle scatterers have also exhibited nontrivial probe dynamics [45]. Both two and three dimensional Lorentz models have been the subject of several numerical and analytic studies. In all of the work, persistent negative time-tails have been observed [46, 62, 26, 9]. However, the functional form of such time tails has been debated. The analytic treatment of a d-dimensional Lorentz gas by Ernst and Weyland [26] predicted a negative time tail of the form $t^{-\frac{1}{2}d+1}$ where d is the dimensionality of the system. Molecular dynamics simulations on a two-dimensional hard disk Lorentz model gave a tail that decayed consistent with $1/t^2$ [62]. More recent studies by Franosch and coworkers [47, 48] gave a more complex view of the persistence of the long-time tails of the VACFs. At low densities, the VACFs decay as $1/s^2$ where s is the mean number of collisions. As the density is increased, intermediate and universal power-laws are exhibited indicating a competition between critical and universal relaxation.

The present work thus seeks to understand the behavior of a thick needle diffusing through a three dimensional array of stationary spherical scatterers. The numerical techniques used to integrate the three-dimensional trajectories are similar to those employed in two-dimensions described in Chapter 3 and in Ref. [104] with only subtle differences as discussed in Section 4.2. The enhanced-transport regime seen for finite [104] and infinitely thin needles [47, 48] in a two-dimensional array of point scatterers is not observed in the three-dimensional array as shown in Section 4.3. Contrary to the two-dimensional case, the onset of the trapping (glassy) dynamics is highly dependent on the particle thickness.

4.2 Model and Simulation Details

The Lorentz model considered in this work is comprised of stationary spherical particles randomly distributed throughout a three dimensional box. The probe particle is a rigid, thick needle; a cylinder with a hemispherical cap on each end. The simulation box is a square cube with dimensions 50Å $\times$ 50Å $\times$ 50Å in which periodic boundaries are employed. The radius of the spherical particles is set to give volume fractions analogous to the previously reported two-dimensional data in which transport transitioned from diffusive motion to reptative motion with increasing scatterer density. The scatterer density is reported in

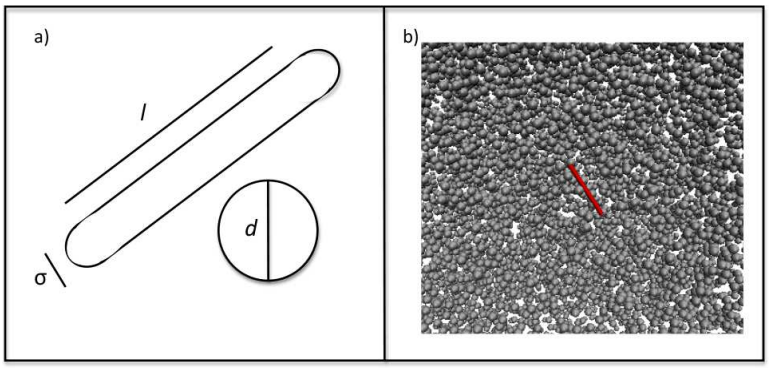

Figure 13: Panel (a) illustrates the aspect ratio, L/σ, of the needle probe. Throughout this work, the length L of the needle is varied in relation to the average scatter density n^*. The relative likelihood of head-on collisions is investigated by varying the width of the needle, σ, in relation to the the larger scatterer diameter. For concreteness, the scatterer diameter is fixed at $d = 2$Å. Panel (b) shows the needle within one of the densest cases ($n^* = 12$) of three-dimensional spherical scatterers considered in this work.

terms of the reduced density n^*,

$$n^* = nL^3 \,, \tag{29}$$

where n is the number density of particles and L is the length of the needle probe. The Lorentz model studied herein is illustrated in Figure 13. Three different needle widths are studied, $\sigma = 0$Å, $\sigma = 0.1$Åand $\sigma = 0.5$Å. The length of the cylindrical portion is held constant for all three needle widths at $L = 5$Å. The diameter of the stationary spherical scatterers is also held constant through all of the simulations at $d = 1.0$Å. Interactions between the needle probe and the stationary obstacles is strictly elastic and limited to hard collisions between the solid representations of the particles. The overall kinetic energy of the probe consequently remains constant and collisions with the probe change only the resolved components of both translational and rotational velocity of the needle.

The integration of this model was carried out using an in-house Fortran code that was validated using appropriate limits. The algorithm used is a three-dimensional analog of the algorithm used previously for a two-dimensional needle as described in Chapter 3 and Ref. [104]. In between collisions, trajectories are integrated through the formally-exact

free-particle equations of motion,

$$\vec{\mathbf{r}}(t+\tau) = \vec{\mathbf{r}}(t) + \vec{\mathbf{v}}\tau \tag{30a}$$

$$\vec{\mathbf{u}}(t+\tau) = \mathbf{R}\vec{\mathbf{u}}(t)\,, \tag{30b}$$

where $\vec{\mathbf{v}}$ is the translational velocity, $\mathbf{R}$ is the rotation tensor for the the angular velocity $\vec{\omega}$ and $\vec{\mathbf{u}}$ is the vector defining needle orientation. Collisions were detected using an event-driven algorithm in which the first collision time between the probe and all the scattering particles was tracked after a given collision event. For each colliding pair, the relative velocity was determined along the line (p) defined by the closest point along the cylinder axis with the center of the spherical obstacle. The relative velocity between the closest point along the needle is

$$\vec{\mathbf{v}}_p = \vec{\mathbf{v}} + \vec{\omega} \times \vec{\mathbf{r}}_p. \tag{31}$$

The collision time is obtained using the relative velocity given by Eq. 31 and the distance between the particles. Once the collision is detected for the identified scatterer, the impulse is

$$j = \frac{-2\vec{\mathbf{v}} \cdot \hat{\mathbf{n}}}{(m^{-1}) + [\mathbf{I}^{-1}(\vec{\mathbf{r}}_p \times \hat{\mathbf{n}})] \cdot \hat{\mathbf{n}}} \tag{32}$$

where m is the mass of the needle, $\hat{\mathbf{n}}$ is the normal vector of the collision, $\mathbf{I}$ is the inertia tensor, and $\vec{\mathbf{r}}_{\mathrm{p}}$ is the point along the cylinder axes closest to the scatterer. The collisions are considered to be elastic, instantaneous and frictionless. Note that Eq. 32 is simplified because it involves a stationary —viz immovable— object. The resulting post-collisional velocities are

$$\vec{\mathbf{v}}_f = \vec{\mathbf{v}}_i + \frac{j}{m}\hat{\mathbf{n}} \tag{33a}$$

$$\vec{\omega}_f = \vec{\omega}_i + \mathbf{I}^{-1}(\vec{\mathbf{r}}_{\mathrm{p}} \times j\hat{\mathbf{n}})\,. \tag{33b}$$

The three different correlation functions computed in this work,

$$C_{\mathrm{MSD}}(t) = \langle(\vec{\mathbf{r}}(t) - \vec{\mathbf{r}}(0)) \cdot (\vec{\mathbf{r}}(t) - \vec{\mathbf{r}}(0))\rangle \tag{34a}$$

$$C_{\mathrm{VACF}}(t) = \langle\vec{\mathbf{v}}(t) \cdot \vec{\mathbf{v}}(0)\rangle \tag{34b}$$

$$C_1(t) = \langle\hat{\mathbf{u}}(t) \cdot \hat{\mathbf{u}}(0)\rangle. \tag{34c}$$

associated with the mean square deviation (MSD) in the center of mass of the needle $\vec{r}$, the velocity auto-correlation function (VACF), and rotational (rot) correlation function in the unit vector $\hat{u}$ denoting the needle direction, respectively. According to the Brown-Einstein-Smolouchowski, the first of these should obey the simple expression

$$C_{\mathrm{MSD}}(t) \;=\; 6D_{com}t \tag{35a}$$

where D_{com} is the translational diffusion constant. In the linear response limit, the latter two are related to the collision times τ and the rotational diffusion constant D_{rot} through the decaying functions,

$$C_{\mathrm{VACF}}(t) \;=\; \exp(-t/\tau) \tag{35b}$$

$$C_1(t) \;=\; \exp(-2D_R t)\;, \tag{35c}$$

where the latter has been called the Debye approximation or small-step-diffusion model as described by Hansen and McDonald [40]. The diffusion constants have been determined from the numerical simulation data through least-square fits. The linear form of the MSD was treated directly. The early to intermediate-time behavior in the exponentially decaying correlation functions —C_{VACF} and C_{rot}— have been fit to lines in a semi-log representation.

Although the needle moves ballistically between collisions, its dynamics were observed to be approximately diffusive within $\sim$ 10 collisions. The collision times for each model parameter set are listed in Table 4. The standard error of the fits to Eqs. 35 provides a representative error in the corresponding diffusion constants. This assumes that the error in the ensemble averages is smaller or comparable to that found from the fits which is reasonable given the number of trajectories used in the ensemble average. The apparent agreement between the exponential fits and the rotational and velocity correlations shown below has been observed in a regime within a few decay times. The simulations were not run long enough to investigate the question [46, 62, 26, 9] of whether violations from these simplified models would lead to long time tails in the correlations. As summarized in the introduction, this is an important question, but the results from the simulations of this work do not address it.

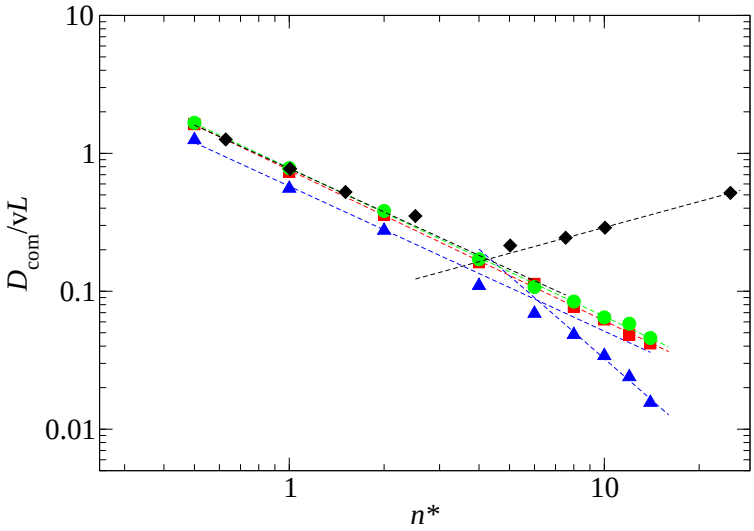

Figure 14: Diffusion coefficients for a needle diffusing through two- and three-dimensional scatterers are shown as a function of the normalized scatterer density, n^*, in a log-log plot. Three-dimensional needles with σ equal to 0 —viz, infinitely thin—, 0.1Å, and 0.5Å, are shown as green circles, red squares, and blue triangles, respectively. Results from Chapter 3 and Ref. [104] for two-dimensional needles with $\sigma = 0.013$ Åare reproduced in black diamonds. Power-law fits to the diffusion coefficients are indicated using dotted lines.

4.3 Results and Discussion

The diffusion coefficients of the needle probe in a three-dimensional array of spherical stationary obstacles are displayed in Figure 14. When the scatterer density is low, the diffusion coefficients follow the expected Enskog behavior, i.e. the diffusion coefficients decay as $D_{\rm com} \sim 1/n^*$. As the density of spherical scatterers is increased, a transition occurs when the needle width is large enough to induce trapping which is visible for the thickest needles with $\sigma = 0.5$. In this trapping regime, the translational diffusion of the needle probe now begins to decrease. The diffusion coefficient obeys a power law, $D \sim t^{-2}$. Note that this power-law behavior is unrelated to the suppressed rotational diffusion observed due to the Edwards tube. The enhanced motion observed in the two-dimensional system [104, 47] (shown as black diamonds in Figure 14) is not observed. The latter is a manifestation of the glancing (or side) collisions of the needle with the scatterers giving rise to effective tubes through which the needle diffuses more quickly. In three-dimensions, however, the glancing

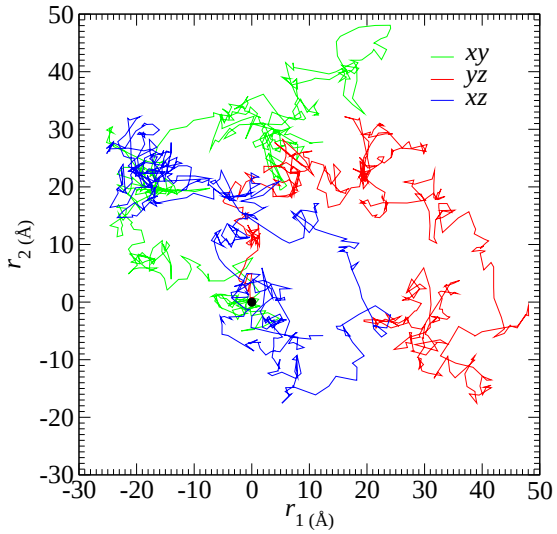

Figure 15: Representative trajectories of the infinitely thin needle in the largest density considered, $n^* = 14$. The green curve is the xy-projection of the trajectory, the blue is the xz projection and the red curve is the yz projection of the trajectory. The black dot shows the corresponding positions of the center of mass of the needle at $t = 0$ which is located at the origin (0,0).

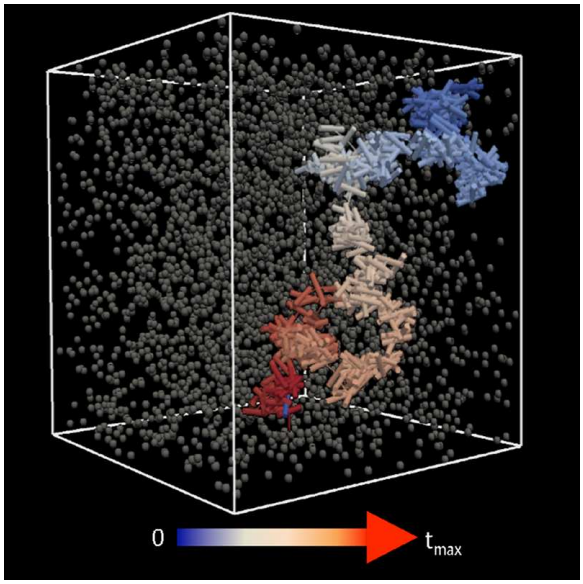

Figure 16: A representative trajectory of a needle with finite thickness diffusing through a random, fixed array of spherical scatterers shown in grey. The needles are colored with respect to time in which $t = 0$ is shown in blue and progresses to red at $t_{\max} = 500$ ps.

collisions remain rare, and the needle does not experience the transition to the enhanced-transport regime. Instead it continues to obey Enskog behavior until the density reaches a still higher value at which both head-on and glancing collisions give rise to the trapping transition. This is further exhibited by the sample trajectories shown in Figures 15 and 16. The projections are indicative of diffusive behavior despite the large scatterer density that in the commensurate 2D system produces (correlated) enhanced transport through self-induced tubes. Thus in two dimensions, the dynamics depend on both the ratio of the length *and* width of the needle relative to the scatterer spacing giving rise to the possibility of two dynamical transitions. In three dimensions, the dynamics depend only on the ratio of the width of the needle relative to the scatterer spacing, and hence give rise to a single transition.

The rotational motion of the needle can be characterized through the rotational correlation function in Eq. 34c. The rotational correlation functions found at a variety of obstacle densities are shown in Figure 17; the symbols are calculated from the simulations and the solid lines are functional fits. At densities in which no anti-correlations are observed, the correlations fit a single exponential, Eq. 35c. At low scatterer densities, anti-correlations are observed because the needles are able to coherently rotate for longer times. At these densities, the anti-correlations are presumed to arise from an oscillatory motion at a frequency corresponding to the average rotation. The correlation functions are consequently fit to the product, $C_1(t) \approx \cos(\alpha t)\exp(-2D_{\rm R}t)$, in which an exponential decay envelops the oscillatory behavior. This simple interpolation combining the Debye approximation and the free rotor model has precedent in the "extended-diffusion" (or J-diffusion) model of Gordon [37, 11]. The average rotational velocity observed in the simulations is $\langle\omega\rangle \approx 2.5$ ps^{-1} which is comparable to the rotational velocity for a freely rotating needle, $\omega_{\text{free rotor}} \approx 3 - 3.5$ ps^{-1}. The fact that the optimal values for α in the fits range from $1 - 3$ ps^{-1} suggests that the slight oscillatory motion observed in the rotational correlation functions is a residue of the free rigid rotor motion at sparser densities. In both regimes, $D_{\rm R}$ is interpreted as the rotational diffusion constant assuming simple diffusive behavior. The diffusion coefficients obtained from the fits are listed in Table 3 and illustrated in

Figure 18. The power-law fits (also shown as dotted lines in Figure 18) to the rotational diffusion coefficients suggest a transition from the expected Enskog behavior with a slope equal to -1 to suppressed rotational motion with a slope approximately equal to -2. This power-law behavior is consistent with that found in earlier simulations of two-dimensional needles [104, 47]. It also agrees with previous work by Doi and Edwards [23]. As expected, the correlations in the rotational motion increases with increasing scatterer density and with increasing needle thickness.

The correlations observed in the three-dimensional rotational motion differ from those seen in the corresponding two-dimensional system. The latter system shows more correlations in rotational motion with respect to time at lower scatterer densities. This appears to be another manifestation of the fact that the reptative regime is not observed in three dimensions. Namely, the suppressed rotational motion seen in two-dimensions allows for the dynamics to be dominated therein by the reptative-like motion of the needle through effective tubes. The increased rotational motion in three-dimensions does not admit the self-induced formation of tubes. The needle is consequently not trapped in the direction perpendicular to its motion at densities above when it is trapped in the parallel direction. Hence only the single transition to glassy dynamics is observed in three dimensions at sufficiently high densities.

The velocity autocorrelation functions shown in Figure 19 collapse to nearly the same form at the short to intermediate times when the time axis is scaled by the corresponding collision times listed in Table 4. Thereafter a small negative correlation appears to varying extents with the most pronounced dips appearing for thicker and longer needles. The negative correlations observed in the VACFs appear to be a manifestation of the dynamics becoming dominated by end-cap collisions causing backscattering, a well-known phenomenon in liquids. The end-cap collisions shorten the effective Edwards tubes and thus suppress reptative motion by the needle. This dip occurs at larger densities as the needle width is decreased. The two-dimensional needle diffusing through an array of points did not show these negative correlations due to the infrequency of end-cap collisions; these collision events did not dominate the dynamics as they do in the three-dimensional system.

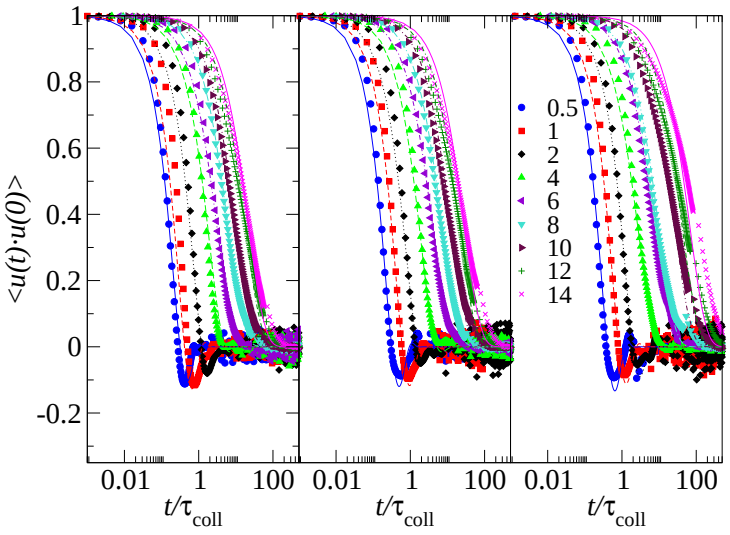

Figure 17: Rotational correlation functions for the needle diffusing though fixed obstacles are shown as symbols at various densities, n^*, ranging from 0.5 to 14 as indicated in the legend. The results for needles with $\sigma = 0$ (infinitely thin), $\sigma = 0.1$Å and $\sigma = 0.5$Å are shown in the left, middle and right panels, respectively. The solid curves are the corresponding fits whose functional forms are described in the text. (Numerical values are listed in Table 3.)

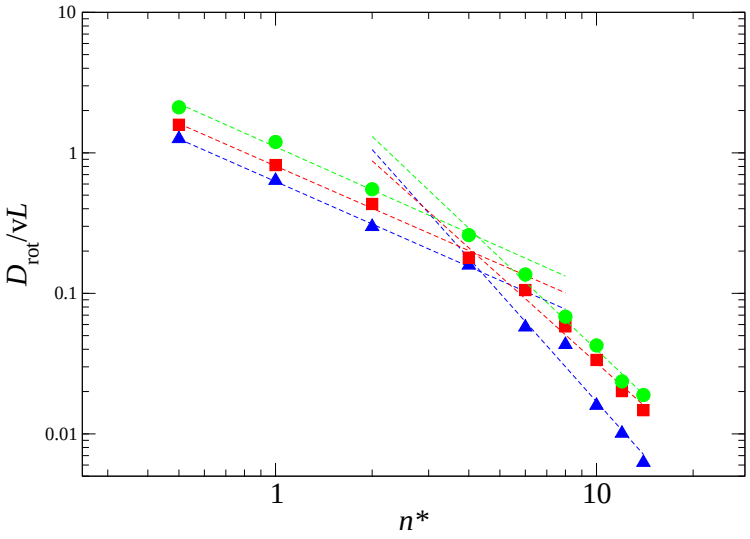

Figure 18: The rotational diffusion coefficients plotted against reduced density, n^* on a log-log scale. The green circles, red squares and blue triangles represent the needle with $\sigma = 0, 0.1$ and 0.5 Å respectively. The dotted lines indicate power-law fits in the Enskog and glassy regimes.

Table 3: The rotational diffusion coefficients (in reduced units, Dv/L) obtained at various scatterer densities, n^*, and needle widths, σ, from the fits of the rotational correlation function shown in Figure 17. At densities below $n^* = 4$, the exponential decay was convolved with an oscillatory term as indicated in the text; only the resulting exponential decay constant is listed here. The frequencies of the oscillation in the best such fits were comparable to the expected value of the free rotor frequency at the thermal rotational energy.

n^*	$\sigma = 0$Å	$\sigma = 0.1$Å	$\sigma = 0.5$Å
0.5	2.1 ±0.05	1.58 ±0.01	1.257 ±0.008
1	1.19 ±0.03	0.82 ±0.01	0.64 ±0.01
2	0.55 ±0.03	0.43 ±0.01	0.298 ±0.008
4	0.3 ±0.1	0.2 ±0.1	0.159 ±0.005
6	0.14 ±0.09	0.11 ±0.01	0.058 ±0.006
8	0.068 ±0.003	0.058 ±0.002	0.043 ±0.007
10	0.043 ±0.003	0.0336 ±.0005	0.016 ±0.005
12	0.024 ±0.004	0.020 ±0.002	0.010 ±0.006
14	0.019 ±0.003	0.015 ±0.003	0.006 ±0.005

Meanwhile, the VACFs shown here do not display the shoulders observed in the analogous two-dimensional system [104, 47] though this may be a result of insufficient sampling in the 3D simulations.

Table 4: The collision times (ps) for a given needle width and reduced scatterer density.

n^*	$\sigma = 0$Å	$\sigma = 0.1$Å	$\sigma = 0.5$Å
0.5	3.1	2.8	2.4
1	1.5	1.4	1.1
2	0.75	0.66	0.54
4	0.33	0.30	0.24
6	0.21	0.19	0.14
8	0.15	0.14	0.11
10	0.12	0.11	0.083
12	0.090	0.094	0.070
14	0.085	0.076	0.060

The diffusion coefficients obtained from fitting the velocity autocorrelation functions with an exponential function are listed in Table 5. The diffusion coefficients calculated from the velocity-autocorrelation functions are systematically higher than the MSD but are mostly in good agreement within the error bars. The diffusion coefficients diverge more from

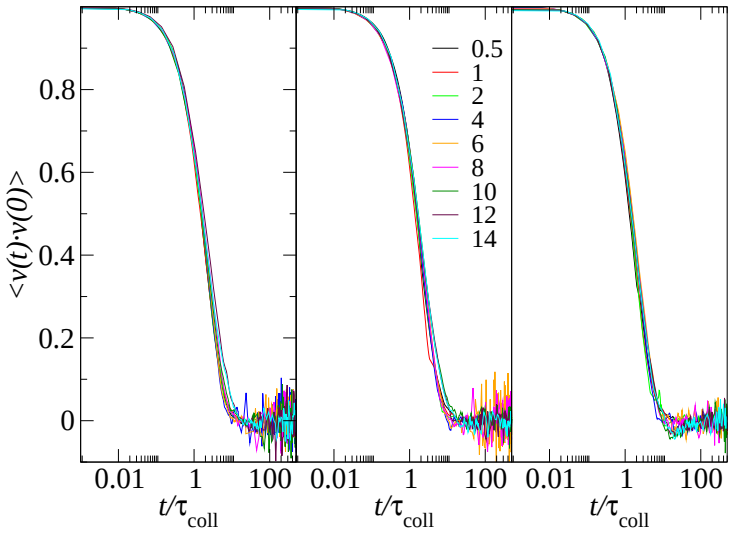

Figure 19: The velocity autocorrelation functions for needles with $\sigma = 0$Å (infinitely thin), $\sigma = 0.1$Å and $\sigma = 0.5$Å are shown in the left, middle and right panels, respectively. As the scatterer density, n^*, is increased, the scaled behavior at short to intermediate times overlap well. The collision times, τ_{coll}, used in this scaling are listed in Table 4. They decrease with increasing scatterer density as should be expected. Similarly, the collision times decrease with increasing needle width.

those calculated using the MSD when the needle width is large and the scatterer density is high. This occurs at the largest densities when the anti-correlations or backscattering in the VACF is most prevalent, and when the assumptions underlying dissipative motion begin to break down.

4.4 Concluding Remarks

In this work, we have shown that the three-dimensional system of a freely translating and rotating needle in stationary scatterers does not exhibit the enhanced translational motion due to reptation that is observed in the two-dimensional system studied previously in Chapter 3 and Refs. [104], [47] and [48]. We have found that the presence of direction reversing collisions (due to collisions with the endcap of the needle with the scatterer) dominates the dynamics in part because the rate of side collisions is dramatically reduced. As a consequence of the loss of this secondary dynamical mechanism, the three dimensional system exhibits only a single transition from Enskog behavior to glassy dynamics as illustrated

Table 5: The translational diffusion coefficients (in reduced units, D/vL) found at the given scatterer densities n^* and needle widths σ directly from the mean-squared displacement (MSD) and from exponential fits to the velocity autocorrelation functions (VACFs). The error bars have been computed according to the standard error of the fits to the corresponding data.

n^*	$\sigma = 0$Å		$\sigma = 0.1$Å		$\sigma = 0.5$Å	
	VACF	**MSD**	**VACF**	**MSD**	**VACF**	**MSD**
0.5	2.04 ±0.01	1.7 ±0.4	1.959 ±0.003	1.6 ±0.3	1.428 ±0.004	1.3 ±0.1
1	0.91 ±0.02	0.8 ±0.1	0.893 ±0.007	0.7 ±0.2	0.61 ±0.01	0.56 ±0.08
2	0.45 ±0.04	0.38 ±0.05	0.407 ±0.009	0.36 ±0.08	0.27 ±0.02	0.28 ±0.05
4	0.20 ±0.07	0.17 ±0.02	0.20 ±0.02	0.16 ±0.04	0.15 ±0.004	0.11 ±0.03
6	0.138 ±0.005	0.11 ±0.01	0.128 ±0.006	0.11 ±0.04	0.09 ±0.01	0.069 ±0.008
8	0.10 ±0.01	0.084 ±0.009	0.10 ±0.01	0.08 ±0.01	0.07 ±0.01	0.048 ±0.007
10	0.08 ±0.03	0.065 ±0.007	0.077 ±0.009	0.062 ±0.008	0.051 ±0.007	0.034 ±0.003
12	0.065 ±0.004	0.057 ±0.007	0.06 ±0.01	0.048 ±0.006	0.04 ±0.01	0.024 ±0.002
14	0.04 ±0.02	0.046 ±0.008	0.05 ±0.02	0.042 ±0.003	0.04 ±0.02	0.016 ±0.002

both by diffusion coefficients associated with the MSD's and the collision times associated with the VACFs.

Thus the effective tubes that give rise to reptation in two dimensions are fragile. Their existence depends on just the right balance between the suppression of the needle in directions perpendicular to it but effectively unhindered in the parallel direction. In two dimensions, this arises when the density is sufficiently large that the needle length is longer than the average spacing between scatterers while the needle width remains sufficiently smaller than this spacing. In three dimensions, however, the needle remains untrapped in the perpendicular direction unless the spacing is small compared to its width. This is the same criteria that must be satisfied for the needle to be trapped in the parallel direction. Hence the needle dynamics in three dimensions exhibits only one dynamical transition. We speculate that the fragile Edwards tubes could reemerge if only there was some additional structure that would somehow couple a long-range correlation in the environment to the length scale of the needle. Indeed, it appears that earlier studies [32, 33] of needles diffusing through three-dimensional liquids of infinitely thin needles exhibited enhanced diffusion.

The three-dimensional model that is the subject of this work should also be experimentally realizable using optical traps. Roichman *et al.* have created three-dimensional arrays of static mesoscopic particles using holographic optical traps [92, 93, 91, 38]. The Roichman group has also assembled ordered three-dimensional structures. For example, they have created icosahedra with 60 1.53μm silica spheres in water and a body centered cubic arrangement of optical traps [38]. The diffusion of monodisperse colloidal particles through traps has also been successfully observed by orienting evenly spaced potential energy wells (traps) and allowing the monodisperse colloids to pass through a 20x2 array of optical traps [93]. The holographic technique used by the Roichman group allows for arbitrary positioning of the traps, and hence the limit of random traps discussed in this work should be accessible. Such work could confirm the transitions found in this work and explore the extent to which restructuring the solvent could reintroduce the enhanced transport [104] to the three-dimensional system.

There are also connections to the dynamics of macromolecules through porous gels. Varying the pore size of the gels as well as the conformation and geometric shape of the macromolecule gives rise to a variety of dynamical regimes [36, 22, 1]. The scatterers in this model create a structure through which the needle diffuses. The ease of such motion is affected by the geometry of the needle—*i.e.*, the thickness and length will determine if the needle is able to access the structure. The findings in this work suggest that the competition between these length scales—including the pore size and the correlation length of free space along the parallel direction—will strongly affect the type and number of transport regimes that are accessible to the needle.

CHAPTER V

DIFFUSION OF A SPHERICAL PROBE THROUGH STATIONARY NEMATOGENS: EFFECT OF INCREASING GEOMETRIC ANISOTROPY AND LONG-RANGE STRUCTURE

5.1 Introduction

Many systems exhibit anisotropic diffusion caused by geometric and/or spatial anisotropy. Such systems typically include a probe or solute diffusing through an ordered array or liquid crystalline phases [108, 97, 56, 83, 58, 59]. A simple model that encompasses anisotropic diffusion is a variant of the Lorentz model where the stationary scatterers are fixed needles and a spherical probe is allowed to freely translate through the resulting mesh. The ability of the probe to diffuse through the scatterers depends upon the density of the scatterers, as well as the aspect ratio, L/D and the long-range orientation of the scatterers. As the aspect ratio of the needles is such that the length approaches zero, the dynamics simply reduce to that of a spherical probe translating through stationary spheres. When the aspect ratio of the stationary needle is increased, the geometric anisotropy as well as the ability to possess long-range order allows for complex dynamical behavior of the spherical solute. Significant work has been performed to study Lorentz models, i.e., systems in which a probe particle diffuses through a series of stationary scatterers with a variety of geometric structures for both the solute and the stationary scatterers [104, 27, 46, 47, 26, 25, 67, 9, 62, 13]; the variant studied in this work adds to the large body of work done on Lorentz models.

Variants of Lorentz models have been widely studied and have provided insight into diffusive behavior in a number of more complex systems [27, 47, 104]. The fundamentals of the behavior captured by Lorentz models is relevant to a wide variety of systems, including diffusion in liquid crystal systems, transport of molecules within cells and also the transport of cells. Lorentz models have also been utilized to recreate diffusion in a network of polymers and have exhibited dynamics with an interesting scatterer density dependence.

These systems have also shown long time tails in the the mean square displacement (MSD) and the velocity autocorrelation function (VACF), as well as non-exponential decay of the VACF when the scatterer density is large [104, 27, 46, 47, 26, 25, 67, 9, 62, 13]. Previous work on Lorentz models composed of spherical scatterers with a structureless point particle probe have displayed an unexpected density dependence in both two and three dimensions [27, 46]. The particle exhibits expected diffusive behavior until a critical scatterer density is reached, upon which, the probe begins to exhibit sub-diffusive behavior [27]. Work on a Lorentz model comprised of a two dimensional network of stationary structureless point scatterers with a freely rotating, translating needle has also uncovered a diverse range of dynamical behavior [47]. Variations in the density of scatterers as well as needle width have displayed the ability to tune the dynamical behavior to different types of motion, specifically from the expected Enskog diffusion at low densities, to reptative diffusion exhibited by entangled polymers to glassy motion where the needle particle is essentially trapped, as discussed in Chapters 3, 4 and Refs. [104, 105, 47].

In this work, the variant of the Lorentz model studied is comprised of a spherical probe in a three dimensional array of rod-like scatterers. The needle scatterers can be oriented isotropically or given long-range orientational order in a nematic phase. Thus, the model system studied possesses both geometric and spatial anisotropy producing rich dynamics of the freely translating spherical probe. Significant interest has been placed on systems where particles exhibit geometric anisotropy. Such systems can form liquid crystal phases under appropriate conditions, leading to preferred directions of transport. In addition, these systems also exhibit anisotropic diffusion, due to the geometric anisotropy of each scatterer. Theoretical and experimental work performed on systems containing a spherical probe moving through geometrically anisotropic particles include: fibrous filaments [83, 58], colloidal suspensions of spherocylinders or ellipsoids [108], and lyotropic liquid crystals of *fd* virus [52, 102, 53].

Relevant experimental work on silica tracer beads with large radii diffusing through silica colloidal rods has shown a dependence on rod density. When the density of rods is low, the diffusion of the bead is determined by the fluid in which the rods and beads

are suspended. Upon increasing rod density to the point where caging effects begin to dominate, the dynamics depend on the tracer size relative to the size of the mesh network formed by the caged rods [58]. Numerical studies have also shown similar results; excluded volume and spherical contact with rods dictate the dynamical behavior [83]. Theoretical and experimental work on a spherical tracer (apoferritin) in *fd* virus show similar hydrodynamic considerations with respect to tracer size [52, 102, 53]. Additional work concerning the theoretical consideration of a spherical tracer diffusing through a liquid crystal comprised of ellipsoid particles has also been performed near the isotropic-nematic phase transition. As the phase of the ellipses transitions to one in which long-range order is present, the dynamics of the tracer becomes increasingly anisotropic, where the tracer radius also plays a role in the resulting dynamics [108]. In these results, the dynamical effect of changing the geometric anisotropy of liquid crystal particles is not as well described as the effects of changing the dimensions of the probe.

Our model is a simple variant of the previously described systems, in which the colloidal rods are fixed in a random array, thus allowing the study of varying geometric and spatial anisotropy. To that end, the rods are either oriented with no long-range order, a stationary isotropic phase, or with long-range orientational order, a stationary nematic phase. Thus, this model incorporates the effect of geometric anisotropy of each scatterer and collective long-range order of the scatterers on the resulting dynamics of a spherical probe. The stationary scatterers are modeled as spherocylindrical particles where the geometric anisotropy is varied by changing the length, L of the cylindrical portion of the spherocylinder relative to the diameter of the hemisphere cap, D. Aspect ratios, L/D, range from 1 to 10. Systems of interest previously mentioned contain anisotropic particles where L/D ranges from ~ 3 to $\sim$10 for molecular dynamics simulations of liquid crystalline molecules, to ~ 300 for systems containing *fd* virus. For spherocylinders, previous work has shown that liquid crystal phases are accessed when $L/D \geq 3$ [69]. In our model, a hard sphere is allowed to diffuse through the mesh. This work aims to answer the following questions: Is the onset of glassy behavior correlated with density and long range order? Does the structure of the solvent created by long-range order change the dynamics of the spherical probe?

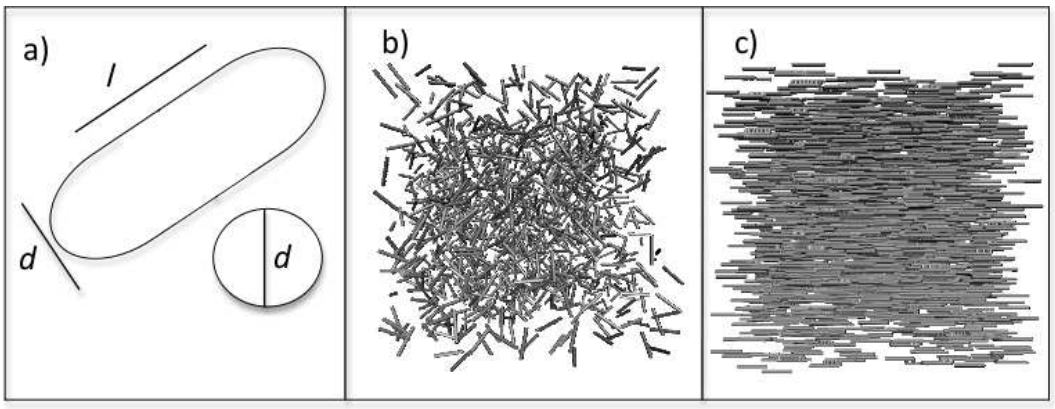

Figure 20: The model used in this work is described pictorially. The first panel shows the aspect ratio of the stationary nematogens with respect to the spherical tracer. The middle panel (b), shows the isotropically orientated nematogens and panel (c) shows the nematically oriented nematogens, with spherocylinders aligned along the x-axis. The length of the cylindrical portion L, is varied which effectively changes the volume fraction.

5.2 Model and Simulation Details

The Lorentz model studied in this work is comprised of a 3D static array of stationary spherocylindrical scatterers, where each scatterer center of mass is placed randomly throughout the simulation box. Two orientations of scatterers are created: isotropic and nematic. Isotropically orientated particles were obtained by randomly rotating the spherocylinders. For systems where the particles are aligned along a director, *i.e.,* a static nematic liquid crystal phase, the particles are aligned along the x-axis of the simulation box. A visual representation of each system is provided in Figure 20.

To probe the dynamics, a spherical tracer is used, where it interacts with the spherocylindrical scatterers via a hard-sphere potential. Each simulation is carried out at constant temperature, 300K, defining initial velocity values. Periodic boundaries are employed in all dimensions, and the overall velocity remains constant because the tracer/scatterer interactions are governed via a hard potential. The spherical tracer is smooth thus rotation of the spherical tracer is not considered. Scatterer density is controlled by varying the length of each spherocylinder and not by changing the number of scatterers.

Once the appropriate orientation of scatterers is obtained, the spherocylinder scatterers are frozen and the tracer particle is allowed to diffuse through the system. Integration of

the equations of motion for this model is carried out using an in-house Fortran code, where the sphere is propagated as a free particle between collisions according to the well known expression

$$\mathbf{r}(t+\tau) = \mathbf{r}(t) + \mathbf{v}(t)\tau, \tag{36}$$

where $\mathbf{v}$ is the linear velocity. The time-step, (τ) is chosen to be a constant value of 1 femtosecond for the ease of collecting data at constant time intervals. However, for dense systems, the value chosen for τ is on the order of the mean collision time.

Particle collisions are detected by determining the closest point between the scatterer and the spherical tracer. Once this point is determined, the relative velocity of this point is set to equal that of the spherical tracer. The collision normal is defined and the relative normal velocity is determined by

$$\mathbf{v}_{\text{rel}} \cdot \mathbf{n} = \mathbf{v}(t) \cdot \mathbf{n}, \tag{37}$$

where $\mathbf{v}_{\text{rel}}$ is the relative velocity along the collision normal, $\mathbf{v}$ is the velocity of the spherical particle and $\mathbf{n}$ is the collision normal. If $\mathbf{v}_{\text{rel}}$ is positive than the spherical tracer is moving away from the scatterer, if it is negative than the particles are colliding. Post-collision velocities are determined by

$$\mathbf{v}_f = \mathbf{v}_i + \frac{j}{m}\mathbf{n}, \tag{38}$$

where $\mathbf{v}_f$ is the post-collisional tracer velocity, $\mathbf{v}_i$ is the pre-collisional velocity, j is the momentum of the collision, $\mathbf{n}$ is the collision normal and the mass of the tracer is m. The momentum of the collision is defined as,

$$j = \frac{-2\mathbf{v}_{\text{rel}} \cdot \mathbf{n}}{\mathbf{n} \cdot \mathbf{n}(\frac{1}{m})}, \tag{39}$$

where the relative velocity, $\mathbf{v}_{\text{rel}}$, is determined from Equation 37.

Varying geometrical anisotropy is considered, where scatterer aspect ratio defines the geometric anisotropy. The length of the cylindrical portion of the particle is varied while the particle density and diameter are held constant. To avoid spurious correlations caused by scatterer length being large with respect to the simulation box, the simulation box was kept at a constant length where the ratio of the simulation box length and scatterer length,

L, did not exceed 3. Results are provided for scatterer densities that ultimately result in diminished diffusive (*i.e.,* glassy) behavior when the scatterer aspect ratio is very large. The results are determined for two needle widths, $\sigma = 0.5$ Å and $\sigma = 0.7$ Å.

5.3 Results and Discussion

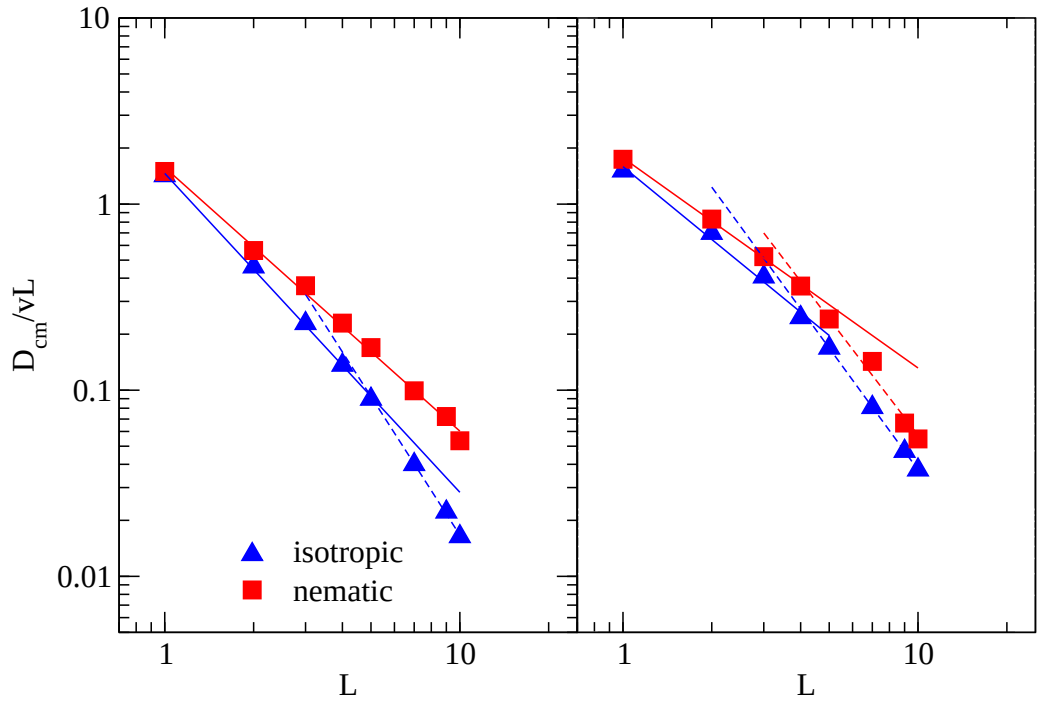

Figure 21: The diffusion coefficients for the nematic (orange squares) and isotropic (blue diamonds) realization of the mesh with respect to the needle cylinder length. The right panel shows data for scatterer width $\sigma = 0.5$ Å and the left for $\sigma = 0.7$ Å. The volume fraction increases with increasing aspect ratio. A downturn in the diffusion coefficients is seen in both scatterer densities in the isotropic mesh. The long-range order of the scatterer particles stave-off entrapment due to effective channels allowing for enhanced transport even at high volume fractions of scatterers for both nematic realization of the mesh. Dotted lines show power-law fits to the diffusion coefficients and help guide the eye to where the critical aspect ratio gives rise to entrapment.

This work aims to elucidate the dynamical behavior of a spherical probe in the stationary mesh when the scatterer density is large enough for the probe to experience glassy behavior. Trapping in these systems is geometric trapping; the probe particle is trapped inside a cage of stationary scatterers, and is not due to kinetic arrest as seen in other glassy systems. The

dynamics of a spherical tracer moving through the isotropic and nematic mesh is provided with varying scatterer aspect ratios, and the appropriate number density, $\rho = 0.05$, to induce entrapment when aspect ratio is large. Two needle widths are studied, $\sigma = 0.5$ Å and $\sigma = 0.7$ Å. The diffusion coefficients for both the isotropic and nematic realizations are shown in Figure 21 for two different needle widths, σ. Diffusion coefficients for the nematic phase are systematically larger than those for the isotropic phase, while the difference in the diffusion coefficients become more prominent as the aspect ratio increases. This behavior is due to geometric anisotropy in consort with long-range order (spatial anisotropy) causing a preferred direction of transport. The orientation of the scatterers along with the geometric anisotropy of the particles produces channels in which the probe can easily diffuse in the nematic mesh. Thus, the spherical probe travels preferentially along the nematic director. There are fewer reflective collisions in these channels, resulting in an overall increase in probe diffusion. A downturn in the diffusion coefficients for needle widths is observed when the scatterer aspect ratio is high enough to induce glassy entrapment of the probe particle. On the other hand, the channels in the nematic mesh caused by the geometric anisotropy and long-range order help to stave off the entrapment for larger scatterer aspect ratios, where no entrapment is observed for the thinner needles studied.

Table 6: The collision times for each length of needle, orientation of the mesh and scatterer width.

L(Å)	$\sigma = 0.5$Å		$\sigma = 0.7$Å	
	isotropic	nematic	isotropic	nematic
1	1.06	1.13	0.493	0.419
2	0.776	0.882	0.410	0.373
3	0.624	0.705	0.314	0.325
4	0.515	0.569	0.265	0.279
5	0.451	0.503	0.230	0.245
7	0.322	0.437	0.120	0.194
9	0.261	0.328	0.167	0.164
10	0.246	0.292	0.154	0.151

The panels in Figure 22 show the MSD data for the isotropic and nematic phase scaled by the squared length, L, of the cylindrical portion of the scatterers. In both phases, the tracer

behavior transitions from super-diffusive at short times to diffusive motion at intermediate times. This transition is due to the non-spherically symmetric nature of the scatterers. The long cylindrical portion of each scatterer allows for directional collisions that do not result in frequent reflections of the probe particle. In the isotropic phase, more direction reversing collisions occur that lead to more reflections of the spherical probe; thus the transition to diffusive and ultimately to sub-diffusive behavior when the probe is trapped, occurs at shorter times compared to transitions observed in the nematic phase. When the aspect ratio is long enough to induce entrapment, sub-diffusive dynamics is observed. Transitions from diffusive motion to a sub-diffusive plateau are observed for larger aspect ratio systems in both isotropic realizations of the mesh and in the nematic phase for the thickest needle. Figure 22 also shows that enhanced mobility caused by channels in the nematic phase leads to larger distances covered by the spherical probe. In the isotropic mesh, we see that probe dynamics is more sensitive to volume fraction than for the nematic mesh.

The VACFs are shown in Figure 23. The isotropic VACFs show a slight aspect ratio dependence in the correlations of the velocity at low aspect ratios, evidenced by the similar correlations observed in the VACFs. However, when the aspect ratio is increased, the spherical probe becomes trapped and anti-correlations are observed. This is due to an increase in collisions resulting in direction reversals in the isotropic phase verses in the nematic phase. The anti-correlations occur around the critical aspect ratio where entrapment begins. The VACFs for the nematic realizations do not appear to be as influenced by scatterer, needle width. The anti-correlations shown in the VACFs in Figure 23 are shown in greater detail in Figure 24 by multiplying the value of the VACF by negative one. This data shows that upon trapping of the probe, long negative time tails emerge. These long time tails decay with power-law behavior. The negative time tails decay with a power-law behavior with an exponent ~ -1 for both the isotropic and nematic mesh when $\sigma = 0.7$ Å. When the needle width is smaller, $\sigma = 0.5$ Å, long time tails are only observed in the isotropic phase with an exponent ~ -1.

In order to observe the anisotropy of the dynamics of the spherical probe, the velocity autocorrelation functions along the nematic director (the x-axis) are given for both phases

of stationary scatterers as well as both needle widths in Figure 25. In the isotropic phase, the VACFs collapse reasonably well when normalized by the collision times. Both data for the isotropic phase show an increase in anti-correlations as the needle length is increased. It is important to note, the VACFs along the perpendicular directions are almost identical for both needle widths in the isotropic mesh. The aspect ratio where these anti-correlations become prevalent are comparable to the needle lengths where entrapment begins to occur. The correlations in the velocity along the director for the nematic phase shows an increase in correlations as the needle length is increased for both needle widths. This is due to the increase in directional collisions caused by the effective tubes created by the long-range order of the system. In the nematic phase, with the largest needle width, anti-correlations are observed when needle length is sufficiently high to induce geometric entrapment. The VACF's along the perpendicular directions decay more quickly than that along the director and also show anti-correlations at smaller aspect ratios further indicating the formation of effective tubes in which the probe traverses.

5.4 Concluding Remarks

This work has investigated the overall aspect ratio dependence of the diffusion of a stationary spherical probe in a network of stationary rods. The orientational order of the geometrically anisotropic rods results in larger diffusion coefficients due to the effective channels or tubes created in which the particle diffuses. The crossover from super-diffusive to diffusive motion is more density dependent in the isotropic phase as compared to the nematic phase. As the aspect ratio is increased, evidence of more severe trapping in the isotropic mesh is displayed in both the MSDs (the plateaus that emerge with respect to aspect ratio) and in the VACFs along the nematic director (the long-time tails in the correlations observed). We also observe the appearance of anti-correlations and negative long time tails when the probe becomes trapped with increasing scatterer length and width. The decay of the long time tails follows a power-law behavior with an exponent ~ -1. The nematic mesh did not show a trapping regime for the smallest needle width but did show trapping when $\sigma = 0.7$ Å. In fact, enhanced transport was exhibited by the spherical probe in the nematic mesh due to

the long-range order and geometric anisotropy of the particle.

We have shown with this simple model that the dynamical behavior of a spherical inertial probe in a system of geometrically anisotropic particles can be efficiently probed. As the aspect ratio of scatterers increases, a change in both the diffusional and glassy dynamics of the system is observed. The observed aspect ratio dependence is visible in both the isotropic and nematic mesh. The nematic mesh shows larger displacements for all aspect ratios and both dynamical regimes when compared to the isotropic.

Implications of this model can be made to probe diffusion through liquid crystal environments, like those of apoferritin in *fd* virus.[52, 102, 53] In this work, hydrodynamic considerations as well as the effect of the tracer size are taken into account. This work looks at the effect of the size of the rod-like scatterer and provides insight into the geometric and spatial anisotropy effect on diffusion. There are also connections between this system and that of a probe traversing a porous gel or matrix of colloidal particles. The pore size or free volume available to the diffusing probe, as well as geometric effects can greatly affect the diffusion of the probe through the media. [36, 22, 1, 83, 58, 108] This work suggests that the geometry of the surrounding gel, *i.e.*, the formation of effective channels by the media vs. a more isotropic orientation of free space, would greatly affect the diffusion through the media.

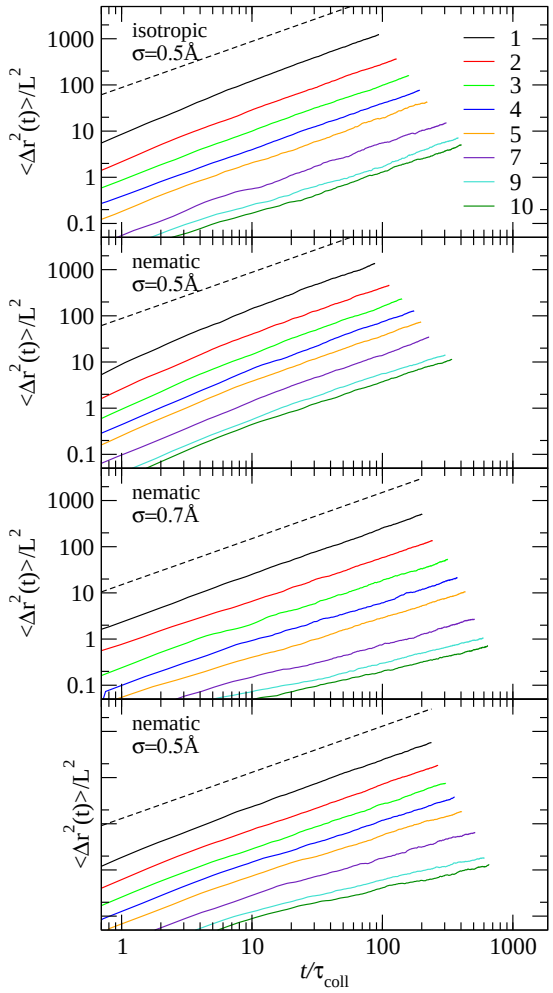

Figure 22: Mean-square displacement (MSD) for varying scatterer aspect ratios and scatterer widths. The top panels show the data when the scatters have a width of $\sigma = 0.5$ Å and the bottom panels shows the data for when the scatter width is $\sigma = 0.7$ Å. As the aspect ratio of the scatterers increases, trapping of the tracer is observed. As the geometric anisotropy increases, the probe enters the sub-diffusive regime, where plateaus start to emerge. The dotted black lines show diffusive behavior, $\langle r^2 \rangle \sim t$. Larger MSD's are observed in the nematic versus isotropic mesh due to the effective channels created by long range order. The MSD given in this figure are used to calculate the diffusion coefficients given in Fig. 21

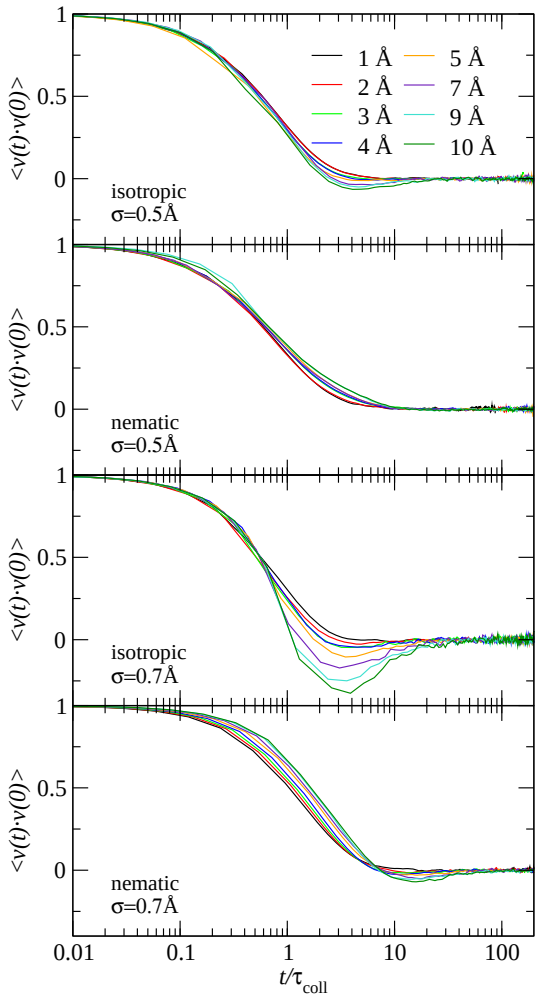

Figure 23: The velocity autocorrelation function (VACF) for varying aspect ratios. The top panels are the data for $\sigma = 0.5$ Å and the bottom for $\sigma = 0.7$ Å. The VACFs given show long correlations with respect to time for both the isotropic orientation of scatterers and the nematic orientation of scatterers. Isotropic and nematic (when $\sigma = 0.7$ Å) realizations of the mesh show slight negative correlations when aspect ratio is large enough for direction reversing collision to dominate the dynamics. Both phases and needle widths collapse reasonably well onto a single curve when normalized by the collision times given in Table 6.

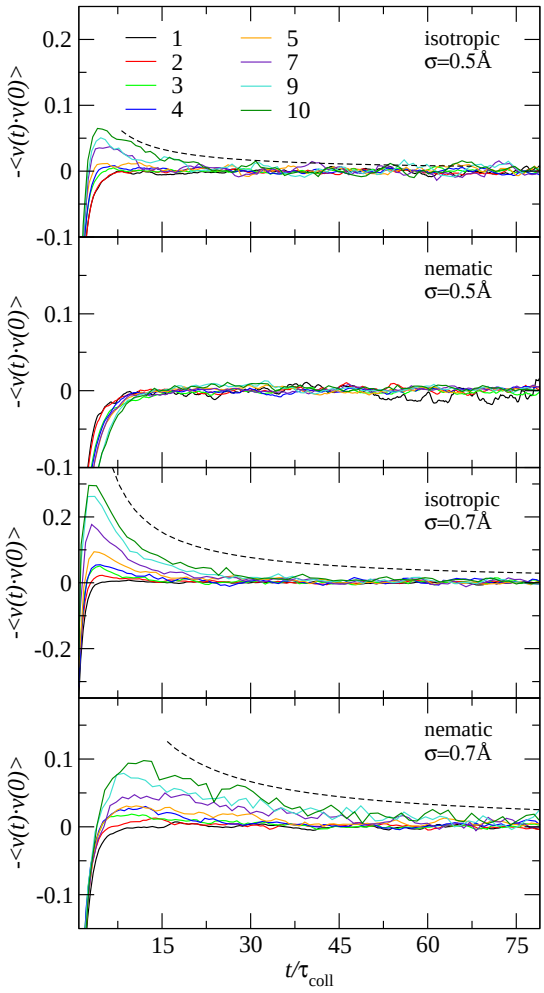

Figure 24: The anti-correlations of the VACFs are shown by plotting $-C_v(t)$. The decay of the long time tail in the VACF is shown. The dotted line indicates a power-law fit that best describes the decay of the long-time tails where the decay goes as t^{-1}.

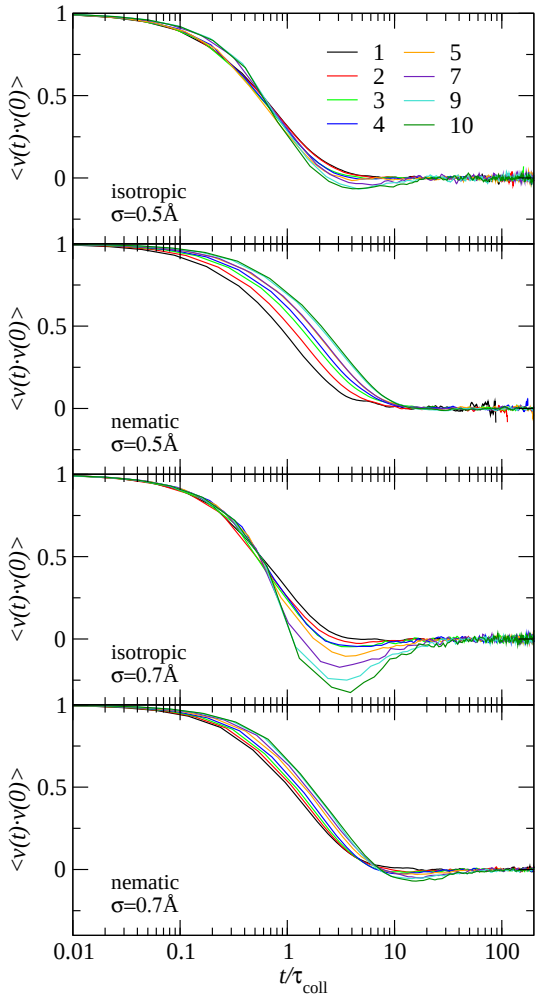

Figure 25: The velocity autocorrelation function (VACF) along the nematic director (x-axis) for varying aspect ratios. The VACFs show longer correlations with respect to time for the nematic orientation of scatterers then for the isotropic. Isotropic realizations of the mesh show slight negative correlations when aspect ratio is large enough for direction reversing collision to dominate. The isotropic VACFs collapse reasonably well onto a single curve when normalized by collision time.

CHAPTER VI

EXTERNALLY DRIVEN LIQUID CRYSTALS: PHASE BEHAVIOR WITH RESPECT TO FREQUENCY AND FIELD STRENGTH

6.1 Introduction

Liquid crystal (LC) systems have been extensively studied due to the exhibited range of phases. The phases range from isotropic, disordered phases to highly ordered crystalline solids. The LC phases that exist in this regime are defined by some degree of isotropy and also long-range order, thus LC phases are defined by the extent of both orientational and translational order exhibited by the system. Orientational order is characterized by the director of the LC, the vector that represents the overall direction that the nematogens are pointing, while translational order is defined by the order that exists in the center of mass positions. While many LC molecules have complex inter-particle interactions as well as complex interactions with the the surrounding fluid, rich phase behavior can be obtained with hard elongated particles [78, 31, 34, 84, 80, 99, 69, 49, 96]. A wide variety of phases have been reached by simply varying the geometric anisotropy, defined by the ratio of the length of the cylindrical portion with respect to the diameter of the hemisphere cap, L/D, of the hard spherocylinder. Transitions from isotropic to nematic to a smectic phase have been observed by changing the volume fraction and the aspect ratio of the particles. Although much work focuses on hard particles, there is also a body of work studying the phase behavior of LC systems with more complicated inter-particle potentials [35, 5, 111, 17] and electrostatic interactions [50].

LC's have also been extensively researched due to their response to optical and electronic perturbations. Much of this work has focused on the response of the LC director induced by an external field [61, 10, 65, 66, 70, 7, 77]. LC particles align themselves with an external field due to the electric/magnetic anisotropy of the molecules. Experiments studying the dynamics of this phenomenon are often carried out using NMR and spectroscopic techniques

where the spectrometer field is used to align the LC particles in the system. Previous work has shown the dynamics of the LC director as the molecules reorient themselves to electric fields that are pulsed and oscillating [65, 66, 70, 7, 77]. It is possible to follow the director and measure the response time of director reorientation with respect to the external fields, as well as determine the effect of field strength. A number of different LC systems have been studied using spectroscopic techniques. Model systems have also been studied to determine the effect of a stationary aligning field on nematogens of spherocylinders [110, 20, 95]. For example, when an external electric field is applied to a system of Gay-Berne molecules, the smectic A phase is stabilized showing the coupling between the orientational and translational order [20]. Also, hard spherocylinders with a freely rotating magnetic dipole have shown stabilization in long-range order when the external electric field is parallel to the dipole. Conversely, destabilization of long range order occurs when the field and dipole are perpendicular [110]. Soft spherocylinders under the presence of an external field have also exhibited a novel crystalline structure in the high field limit [95]. The dynamics of a Brownian particle in a driven system of mesogens have also been elucidated. The reaction dynamics determined by this theoretical description showed that at constant frequencies the product composition can be controlled [45]. This work was performed when the mesogens were in the linear response limit, the mesogens perfectly follow the external field. Presumably, the phase behavior of the mesogens in the the presence of an external field would affect the product composition.

Previous theoretical work has been done on a system of hard spherocylinders. Using density functional theory, different dynamical states of the director of the nematogens have been found. Depending upon the frequency, the nematic director experiences towing, breathing, splitting or overtaking by the external field [41]. The frequencies studied in this work are relative to a frequency, ω_0. This frequency is roughly based on the Brownian time scale of rotation. In our model, the frequencies studied exist predominately in what the authors called the towing regime, where the nematic director follows the aligning electric field with some lag time.

Previous work has shown reentrant phase behavior for LC systems. Seminal work by

Cladis in Ref. [14] showed the first reentrant nematic phase. Systems of binary mixtures of LCs have exhibited reentrance in their phase diagrams. Computer simulations of attractive ellipsoids elucidated a reentrant nematic phase when the attractive interactions are tuned appropriately [21]. Binary mixtures of polar and nonpolar LCs show a transition from nematic to smectic and back to a nematic phase with varying temperature [14, 81, 18] and pressure [16, 15]. In all of these cases, the mixtures show a decrease in order with varying temperature or pressure when an increase of order is expected. Binary mixtures of spherical particles and cylindrical particles also exhibit reentrance [42]. Complex LC systems have shown reentrant phase behavior. For example, in a hydrogen bonded ferroelectric LC, the odd hydrogen bonded complexes show different phase behavior than the even, where a reentrant smectic ordering is observed in the even hydrogen bonding complexes [109]. Also in a chiral smectic LC under an external field, reentrant smectic ordering has been observed via ^{2}H NMR studies on the effect of a magnetic field on liquid crystalline mesophases [24].

The present work aims to provide an understanding of the phase behavior of a LC system under the influence of a rotating electric field by way of molecular dynamics simulation. The system studied is composed of hard spherocylindrical particles where each end has a hemispherical cap. The phase of the LC produced by the rotating electric field is reported and compared to that of the same system without the presence of the aligning field. The frequency dependence of the rotation is explored along with varying the geometric anisotropy of the particles.

6.2 The Model

The LC system is modeled as spherocylindrical particles with hard-sphere interactions. Hard spherocylindrical systems have been shown to exhibit LC phase behavior with a sufficiently large aspect ratio. The aspect ratio of the spherocylinder is defined as the ratio of the length of the cylindrical rod with respect to the diameter of the hemisphere cap, L/D. Systems where $L/D > 4$ have been shown to exhibit LC phases [69]. In the limit where L/D approaches infinity, the Onsager limit, a system of rods exhibits a nematic phase. In the limit where L/D approaches zero, the hard sphere system is obtained. Collisions between

molecules are found using the method described previously in Ref. [89]. Each particle is given a dipole moment that is oriented along the major axis of the spherocylinder. The dipole is solely used to couple the molecule to the driving external field and is subjected to a rotating electric field of either constant field strength and varying frequency or constant frequency with varying field strength. The torque experienced by each particle due to the interaction of the dipole with the electric field causes the particles to rotate about the center of mass. The torque on the dipole due to the electric field is the dot product of the dipole axis and the direction of the electric field. Assuming the particles will follow the electric field with high fidelity, the densities of the systems studied are chosen such that upon rotating the nematogens, the resulting density of the effective hard disks would be slightly less than the jamming fraction. The magnitude of the electric field used in the simulations was guided by similar experimental work [65, 66, 70, 7, 77]. Given the size of the system, the electric field strength applied would result in an electric field of $\sim$ 60V. For studies with constant frequency and increasing field strength , the frequency is held constant at $\omega = 0.5$ ps^{-1} and the field strength is increased from 0 to $\sim$ 500 VM^{-1} which corresponds to $\sim$ 200 V given the system size.

In order to determine the phase of the system, the nematic order parameter and the orientational pair radial distribution functions are calculated. The nematic order parameter is defined as

$$S = \frac{1}{N}\sum_{i=1}^{N} P_2(\cos\theta_i) \ , \tag{40}$$

where P_2 is

$$P_2(\cos\theta_i) = (3\cos^2\theta_i - 1)/2 \tag{41}$$

θ_i is the angle between the director, $\vec{n}$, that characterizes the nematic phase and the principal molecular axis of the nematogen i. The sum is over all of the particles in the system. This method works if the direction of $\vec{n}$ is known *a priori*. Usually, the orientation of the director is not known and must be determined by the order tensor,$\mathbf{Q}$.

$$\mathbf{Q} = \frac{1}{N}\sum_{i=1}^{N}(\frac{3}{2}\mathbf{u_i u_i} - \frac{\mathbf{I}}{2}) \ . \tag{42}$$

The orientation of the molecular axis is given by $\mathbf{u_i}$ and $\mathbf{I}$ is the unit tensor. Diaganolization

of Eq. 42 will produce the nematic order parameter as the largest eigenvalue. The eigenvector corresponding to this eigenvalue is the orientation of the director. Typical values for the order parameter range from zero to one indicating an isotropic and perfect crystalline phase, respectively. LC phases range between 0.25 and 0.8. In practice, isotropic phases will have small non-zero values of the nematic order parameters.

The orientational radial distribution functions is defined as:

$$g_2(r) = \langle P_2(\cos\theta_{ij}(r)\rangle \tag{43}$$

Here the orientational pair distribution function is defined in terms of the Legendre Polynomials where, $\cos\theta_{ij} = \vec{u_i} \cdot \vec{u_j}$, θ_{ij} is the angle between the direction of the molecular axis $\vec{u_i}$ of molecule i and the direction of the molecular axis of molecule j, $\vec{u_j}$ and P_L is the Legendre polynomial of degree L. It has been shown previously that as the aspect ratio of the spherocylinders increases, more LC phases are present. Previous work done on these systems use the same metrics (nematic order parameter and the orientational pair distribution functions) to determine the phase of the system [69]. The phase of the system without the presence of the electric field is determined then compared to that of the phase determined after the system has been perturbed by the rotating field.

6.3 Results and Discussion

6.3.1 Frequency Dependent Phase Behavior

The results of the nematic order parameter calculation for systems where no field is present are given in Figure 26. These results fit well with previous work on hard spherocylinders, where increasing aspect ratio and volume fraction give rise to increasing long-range order. For the densities and aspect ratios studied in this work, without the aligning field, we see mostly isotropically oriented particles and some systems that show nematic alignment. Large geometric anisotropy coupled with an increasing volume fraction leads to long range order. It is possible that in some of the intermediate volume fractions with larger aspect ratios, the fluid is in between an isotropic state and is weakly nematic, giving moderate values for the order parameter. The volume fractions studied in this system are low in comparison to previously described systems [69] in order to accommodate the rotation of

the molecules. However, given the trends provided in previous work, the phase obtained in this work are consistent.

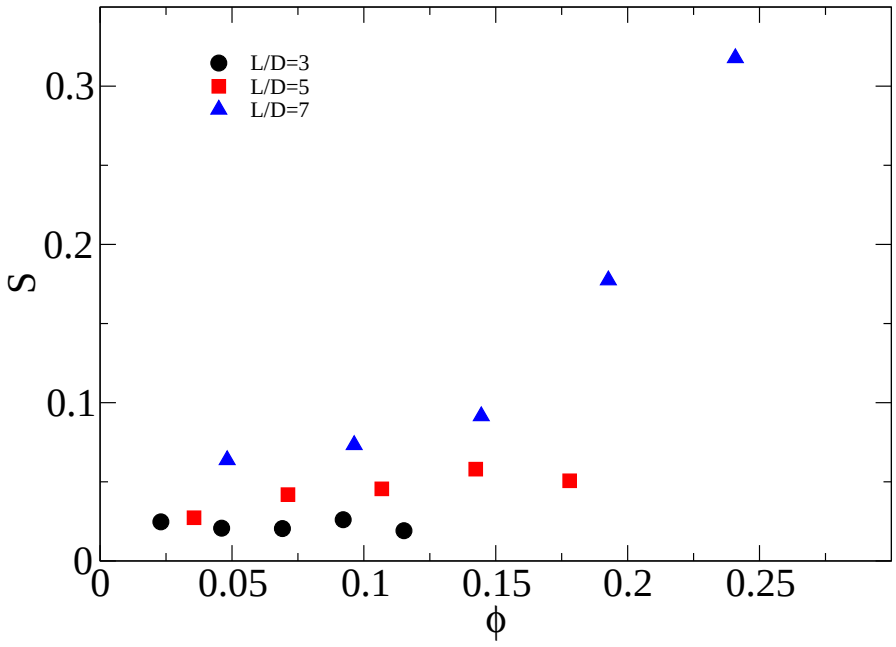

Figure 26: The nematic order parameters with respect to volume fraction, ϕ. The aspect ratio of $L/D = 3$ is given by the black dots, $L/D = 5$ is given by red squares and the blue triangles show data for aspect ratio $L/D = 7$.

The results for the nematic order parameters, calculated using Eq. 42, with respect to frequency is shown in Figure 27. The data is determined from snapshots of the system at constant time intervals, where both the number density of nematogens as well as the aspect ratio are increased. The nematic order parameters given in Figure 27 were calculated based on the time-average of calculated nematic order parameters at equally spaced intervals for a given frequency. As the number density is increased, we see that long-range order decreases with increasing frequency. The same trend is observed with increasing aspect ratio; the larger aspect ratio systems become less ordered. The driven nematogens lose long-range order when the frequency is large. When the frequency is increased, larger aspect ratio particles show a more significant decrease in the long-range order. When the field is static, *i.e* the frequency is zero, larger aspect ratio and larger number densities show an increase in long-range order; the aligning field stabilizes the nematic phase for lower aspect ratios and

volume fractions. This is consistent with previous work concerning the effect of stationary external fields [20, 110, 95].

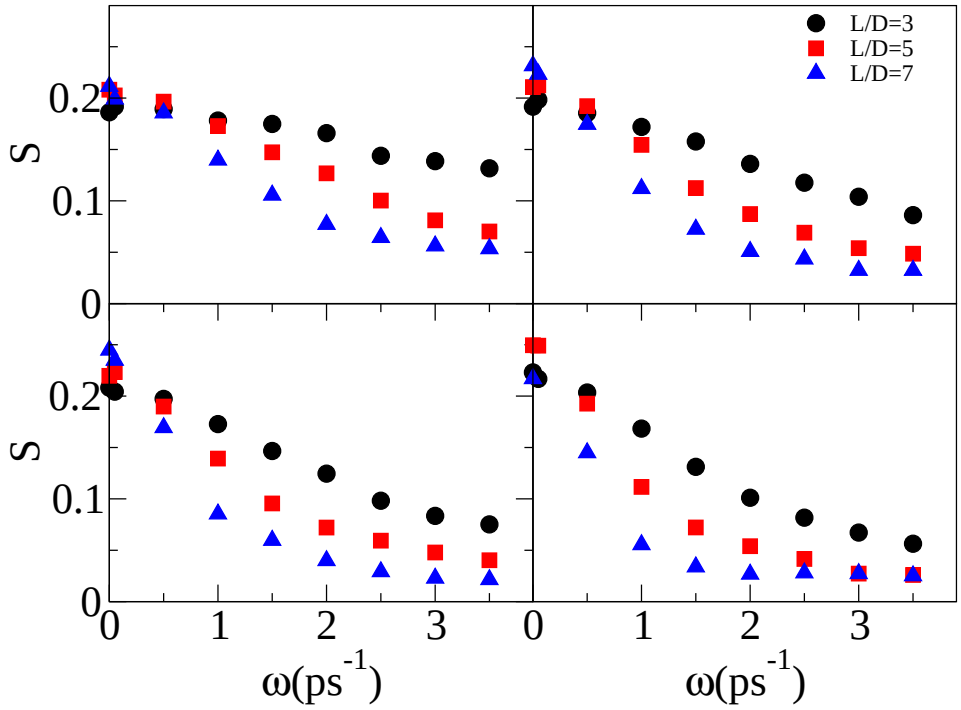

Figure 27: The nematic order parameters with respect to frequency. The number density of particles increases from left to right, $\rho = 0.008$ for the top left, 0.016 for the top right, 0.024 for the bottom left and 0.04 for the bottom right. Black dots are for L/D=3, red squares for L/D=5 and blue triangles for L/D=7.

Another metric to determine the long-range order of the fluid is the orientation correlation function defined in Eq. 43. The orientational correlation functions for varying number densities, aspect ratios and electric field frequency are given in Figures 28-31 with number densities of $\rho = 0.008, \rho = 0.016, \rho = 0.024$ and $\rho = 0.04$, respectively. The orientational correlation functions are reported with respect to center of mass distance, $\mathbf{r}$. The decay of the correlation function to a finite value indicates the presence of long-range order. The data for the stationary field, $\omega = 0$, shows the most order for each system and also an increase in long-range order with increasing aspect ratio. As the frequency increases, the correlation functions begin to decay to zero, indicative of an isotropic phase. The loss of long-range order occurs at smaller frequencies with increasing aspect ratio and nematogen

number density. As frequency increases, long range order decreases with increasing aspect ratio. The orientational correlation functions show the same trend observed in the nematic order parameters. We see that the largest volume fraction studied is most stabilized by the stationary electric field, but under a rotating field the order is lost rapidly. The smaller aspect ratio system, L/D=3, was most resistant to decreases in long-range order with respect to increasing frequency. This is due to the ease in which the shorter particles can follow the external field. Systems with larger volume fractions and larger aspect ratios show more difficulty in following the electric field than those with smaller volume fractions and shorter aspect ratios. In equilibrium systems however, increases in aspect ratio and volume fraction stabilize long-range order thus, there is a competing effect.

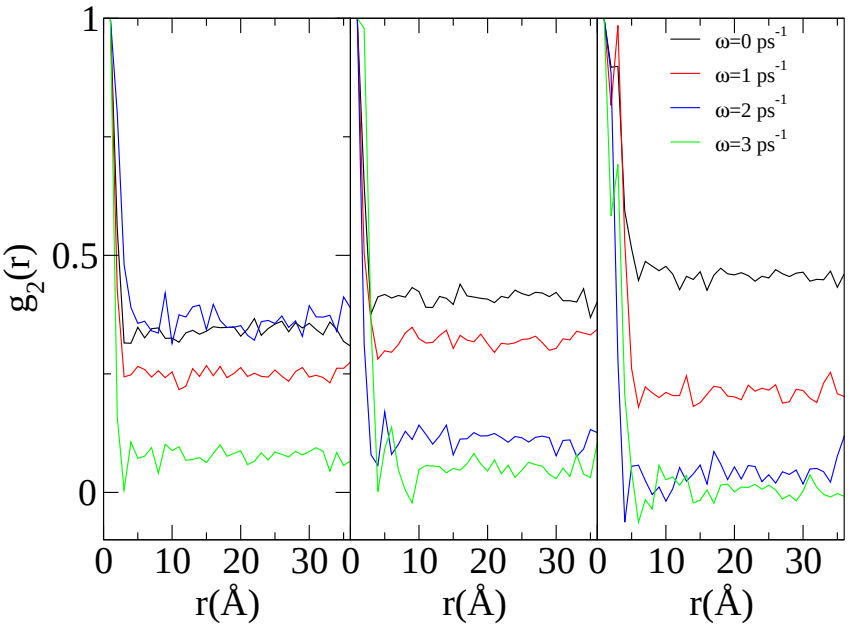

Figure 28: The orientational correlation functions for nematogen number density $\rho = 0.008$ and various aspect ratio for specific electric field frequencies. The left panel is for L/D=3, middle for L/D=5 and the right panel for L/D=7.

The observed loss in long-range order is due to the wobble of the particles around the electric field as well as the difficulty for nematogens to follow the electric field as the field frequency increases. The electric field induces a torque on the nematogen due to the dipole. The imposed torque causes the nematogens to rotate around their center of mass to align

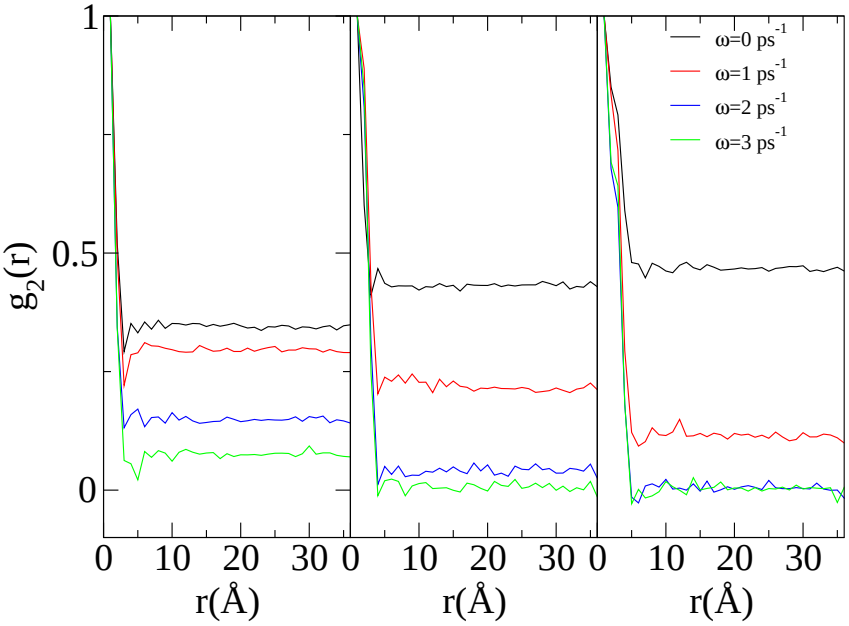

Figure 29: The orientational correlation functions for nematogen number density $\rho = 0.016$ and varying aspect ratio with respect to electric field frequency. The left panel is for L/D=3, middle for L/D=5 and the right panel for L/D=7.

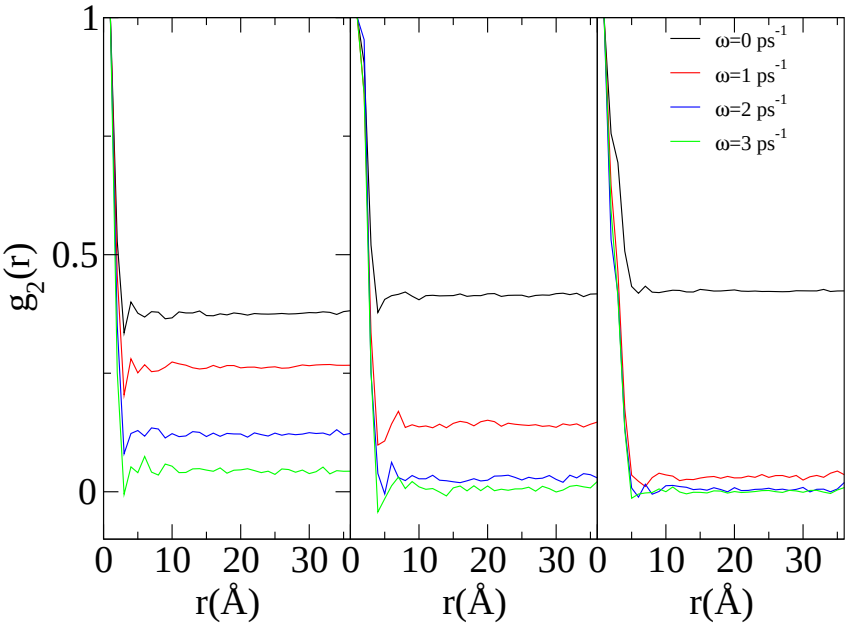

Figure 30: The orientational correlation functions for nematogen number density $\rho = 0.024$ and varying aspect ratio with respect to electric field frequency. The left panel is for L/D=3, middle for L/D=5 and the right panel for L/D=7.

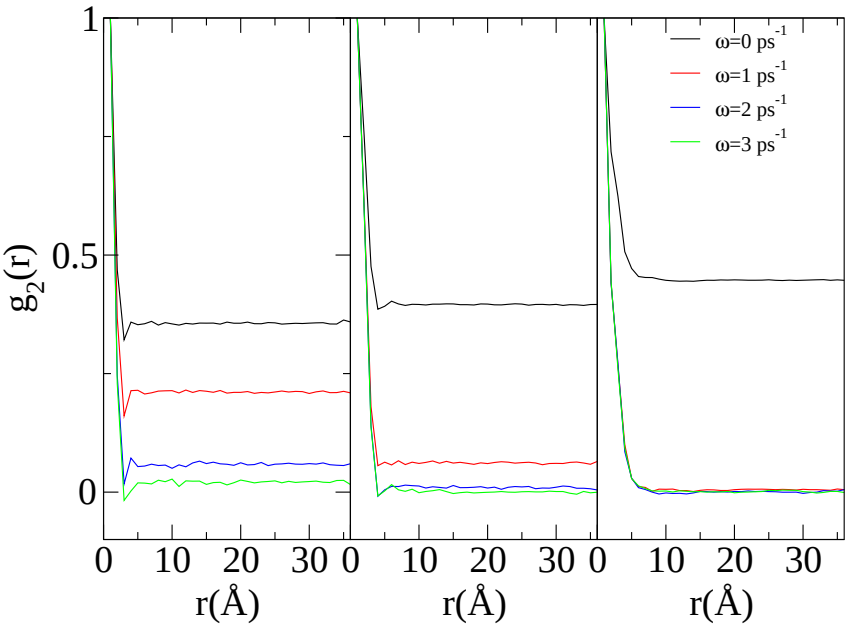

Figure 31: The orientational correlation functions for nematogen number density of $\rho = 0.04$, and varying aspect ratio with respect to electric field frequency. The left panel is for L/D=3, middle for L/D=5 and the right panel for L/D=7.

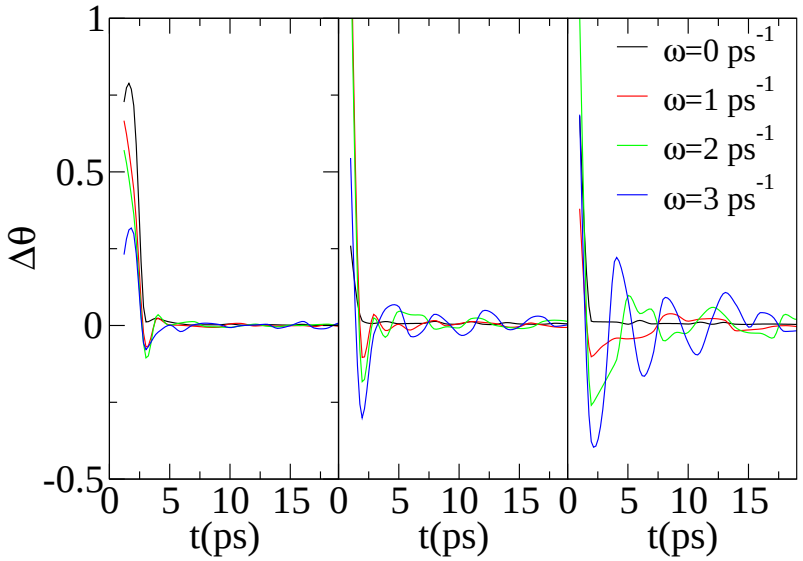

Figure 32: The angular difference between the nematic director and the direction of the external electric field for $\rho = 0.008$ with respect to increasing frequency. The left panel is for L/D=3, middle for L/D=5 and the right panel for L/D=7.

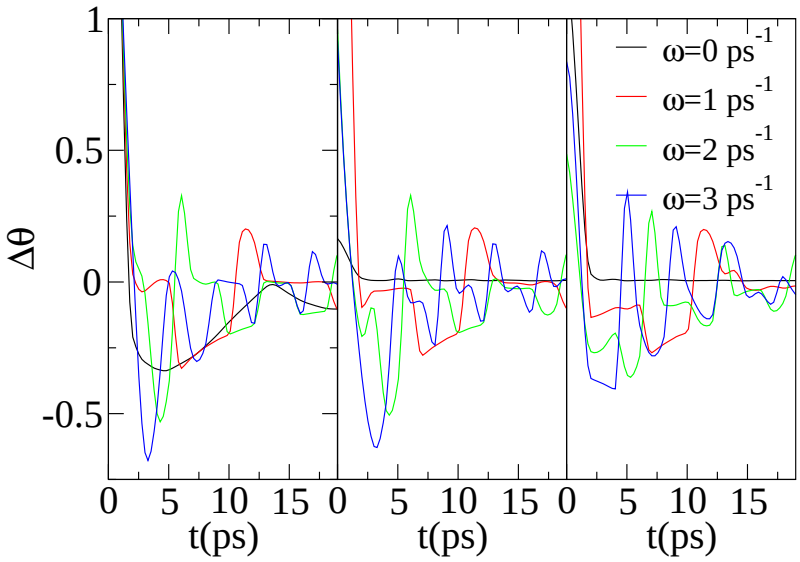

Figure 33: The angular difference between the nematic director and the direction of the external electric field for $\rho = 0.016$ with respect to increasing frequency. The left panel is for L/D=3, middle for L/D=5 and the right panel for L/D=7.

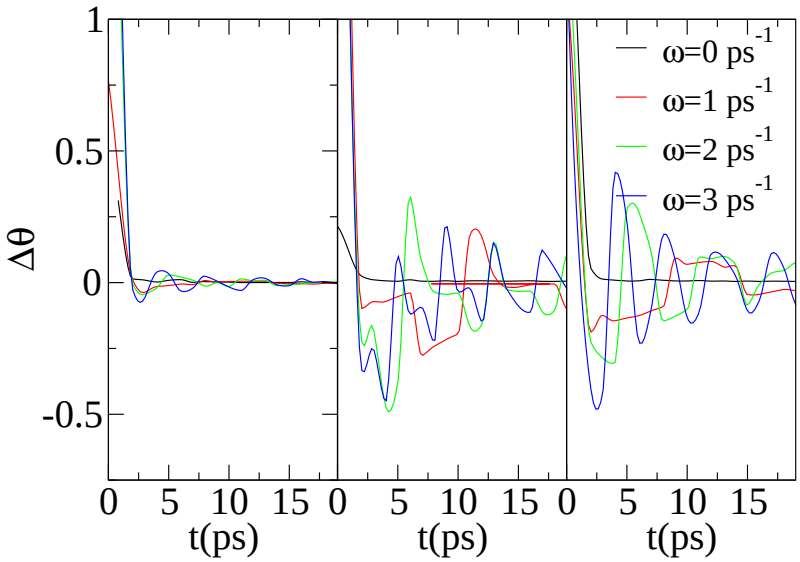

Figure 34: The angular difference between the nematic director and the direction of the external electric field for $\rho = 0.024$ with respect to increasing frequency. The left panel is for L/D=3, middle for L/D=5 and the right panel for L/D=7.

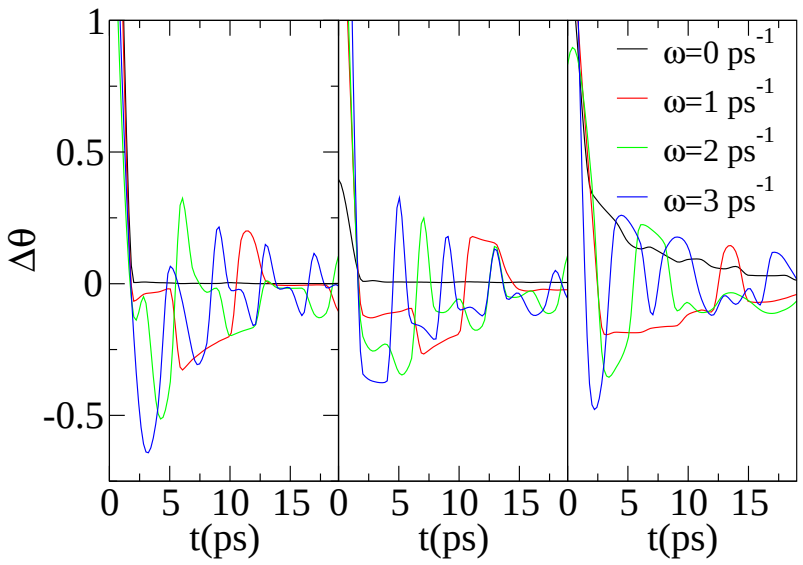

Figure 35: The angular difference between the nematic director and the direction of the external electric field for $\rho = 0.04$ with respect to increasing frequency. The left panel is for L/D=3, middle for L/D=5 and the right panel for L/D=7.

themselves parallel with the external field. Due to the torque however, it is possible for the nematogens to over rotate, producing a torque that will rotate the nematogens back thus creating a precessing motion of the particles around the external electric field. This precessing movement in concert with the quick rotating external field, results in a loss of long-range order. As the nematogen number density increases, the ability of the nematogens to follow the electric field decreases. This is also observed with increasing aspect ratios; giving rise to the trends observed in the nematic order parameters as well as the long-range orientational correlation functions. This behavior is further shown by examining the angular difference between the nematic director, calculated using Eq. 42, and the direction of the external field, shown in Figures 32 through 35. For all number densities and aspect ratios studied, when the field is held static, there is little angular difference. However, when the field frequency is larger, an oscillation about the external field is observed. This oscillation is seen to get larger as aspect ratio increases as well as with increasing number density when the frequency increases.

All of this data can be compiled to give a three dimensional phase diagram with respect to aspect ratio, volume fraction and frequency, given in Figure 36. Isotropic phases lie above

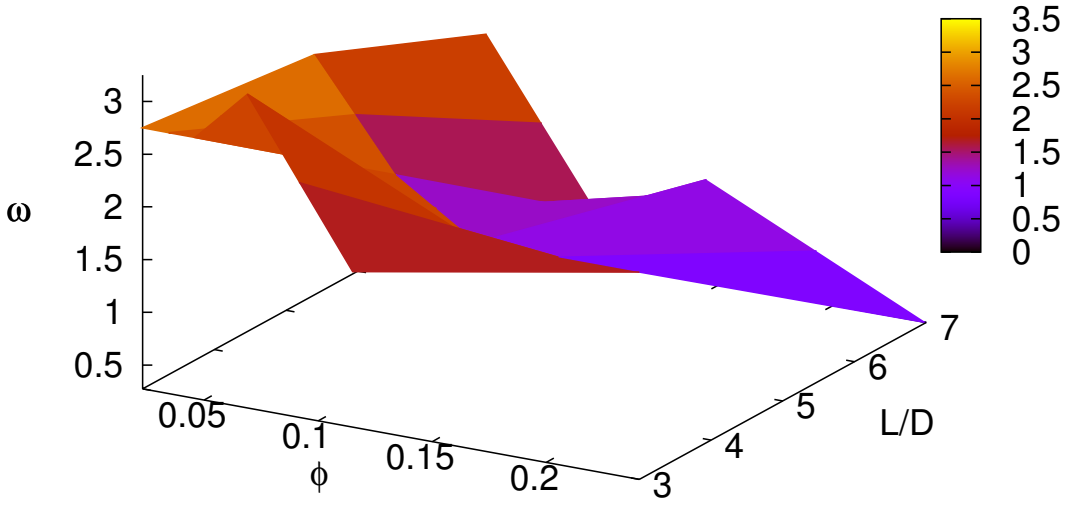

Figure 36: The surface dividing the isotropic from the nematic phases with respect to particle aspect ratio, frequency of the rotating external field and volume fraction. Above the dividing surface, the system exists in a isotropic phase and below is a nematic phase.

the surface, while nematic phases lie below the surface. As the aspect ratio is increased when the frequency is non-zero, the precessing of the nematogens around the electric field causes a decrease in order. A similar trend is observed when the volume fraction is increased for a given aspect ratio; a non-zero frequency destabilizes long range order. We do observe stabilization of long-range order when the field is held static, consistent with the body of work on spherocylinders in external fields [20, 110, 95].

6.3.2 Field Strength Dependent Phase Behavior

The previous section has dealt with the frequency dependent phase behavior of nematogens driven by a rotating, external field. In order to deduce the effect of field strength, a frequency of $\omega = 0.5$ ps^{-1} is applied to a system with number density $\rho = 0.024$ and L/D=7. The nematic order parameters were calculated at regular time intervals throughout the simulation, given the specific nematic director and are shown in Figure 37. Without the presence of the electric field, the nematogens initially exhibit slightly nematic behavior. However, with the addition of a weak electric field, an overall decrease in the amount of long-range order, indicated by a low value of the nematic order parameter, is observed. As

the field strength is increased, a concomitant increase in order parameter is observed as well. This behavior is due to the ease in which the dipole of the nematogen can couple to the electric field. When field strength is very low, each nematogen wobbles around the electric field director. As the field strength increases, the tendency for a nematogen to wobble decreases thus creating more order.

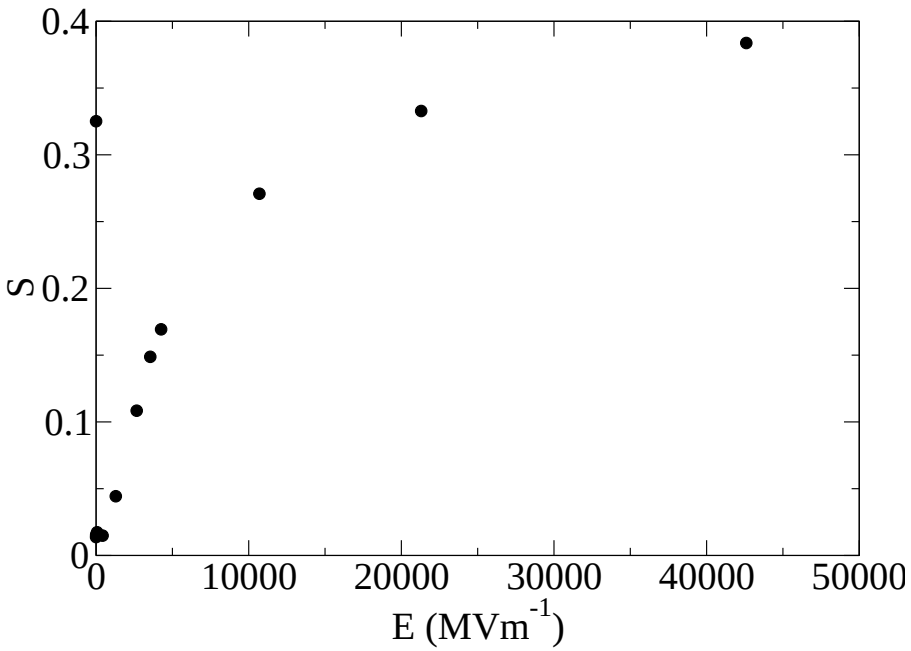

Figure 37: The nematic order parameters with respect to electric field strength for a frequency, $\omega = 0.5\text{ps}^{-1}$ and $L/D = 7$.

The orientational correlation functions are reported with respect to center of mass distance, **r** in Figure 38. The decay of the correlation function to a finite value indicates the presence of long-range order. As the field strength decreases, the correlation functions begin to decay to zero, indicative of an isotropic phase. When the field strength is large, we see a large amount of long-range order is seen. This is due to the increase in coupling with the electric field as the field strength is increased. This is shown in figure 39, where the angular difference between the nematic director and the external field is given with respect to time for selected field strengths. As the field strength increases, the particles couple more strongly to the electric field, as evidenced by the quick decay of the angular

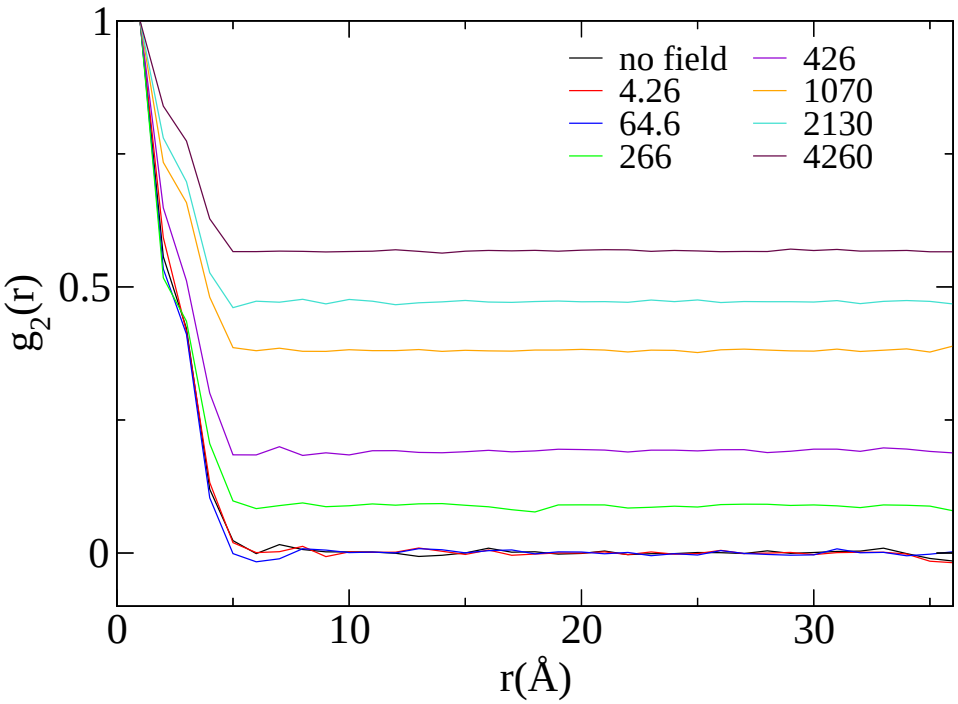

Figure 38: The orientational correlation functions with respect to electric field strength. Field strength increases going from black to purple curves. Field strengths are provided in the figure in units of MVm^{-1}.

differences between the director and field.

6.4 Concluding Remarks

We have shown that an external electric field applied to a system of hard spherocylinders coupled to the field with a dipole, will produce structure depending upon the frequency of rotation of the field. When the field is stationary, we see an enhancement of the nematic phase, accessing nematic phases at lower aspect ratio values as well as lower volume fractions. We also see a destabilizing of the overall order of the system when the field begins to rotate. The larger the frequency of rotation, the larger the disruption of the long-range order. The disruption is particularly enhanced when the aspect ratio of the spherocylinders is very large. This is due to the difficulty of the particles to follow the external field.

We have studied a system comprised of hard spherocylinders driven by an external, rotating electric field. The field strength is varied from 0 (no field) to very large field strengths.

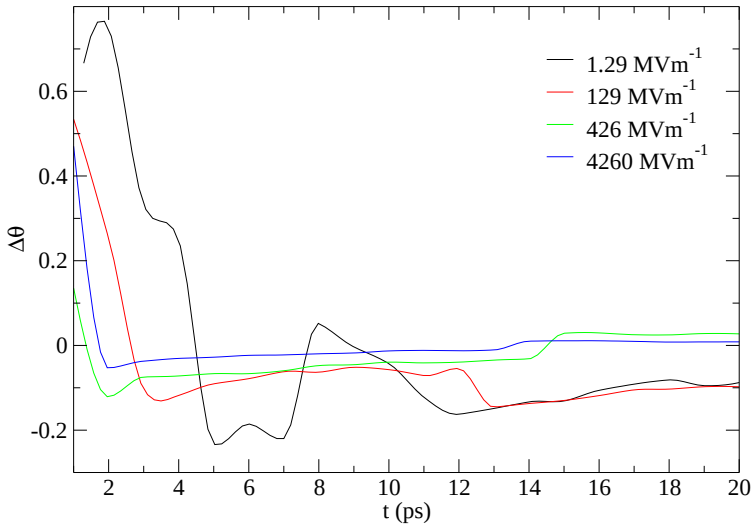

Figure 39: The angular difference between the nematic director of driven nematogens and the electric field for selected values of field strength.

At low field strengths, a decrease in the order of the system from that of the unperturbed system is observed, but as the field strength increases, reentrant nematic behavior occurs. The wobble of the nematogens about the electric field decreases as the field strength is increased, strongly coupling the electric field to the dipole of the nematogens. This work sheds light on avenues in which to control and access LC phases by perturbing the system with an external, rotating electric field.

CHAPTER VII

DYNAMICS OF A SPHERICAL PROBE IN DRIVEN NEMATOGENS

7.1 Introduction

Liquid crystal systems have been extensively studied due to the wide range of phases exhibited, ranging from the isotropic phase to phases displaying long range order. The degree of long range order defines the LC phase. Previous work, as well as the results in Chapter 5, indicate that hard spherocylinders are capable of exhibiting various LC phases [78, 31, 34, 84, 80, 99, 69, 49, 96]. Regarding hard spherocylinders, the LC phase is caused by the volume fraction of the the system and the geometric anisotropy of the hard nematogens, where the geometric anisotropy is measured by the aspect ratio, L/D. It has been previously shown, that a smectic phase is accessible with the proper aspect ratio and volume fraction [31]. Although rich phase behavior is determined with simple, hard-sphere interactions, a large body of work has focused on the phase behavior of nematogens with more complicated inter-particle interactions [35, 5, 111, 17, 50]

LCs respond to external fields, therefore, a large body of work studying the effect of an external field exists [65, 66, 70, 7, 77, 110, 20, 95]. A large portion of this work has focused on the director dynamics when the aligning field is pulsed at an angle to a stationary directing field [65, 66, 70, 7, 77]. Additionally, a large body of work has shown the stabilizing effect of a stationary external field on long range order of the nematogens[110, 20, 95]. It has been observed that stabilizing stationary fields lead to increased long-range order [110, 95]. Also, long-range order and translational order have been stabilized by a strong aligning field indicating that the field induces coupling between the rotational and translation order of the system. This behavior has been observed by an induced smectic phase in Gay-Berne nematogens [20], and the appearance of a novel crystalline phase in soft spherocylinders in the high field limit [95]. In the previous chapter, Chapter 6, the phase behavior of nematogens under the presence of a driving, rotating field was explored. As the frequency

of the rotating field increases, long-range order exhibited by the system decreases. The loss of long-range order is more severe in systems with larger aspect ratios, as well as systems with larger volume fractions of nematogens.

Due to the complex phase behavior exhibited by LC systems, the dynamics of solute in LC solutions exhibit complex, anisotropic dynamics. [58, 83, 52, 102, 53, 108]. Silica beads in colloidal rods have shown dynamics that depend strongly on the rod density when the spherical probe diameter is large. When the rod density is sufficiently large, caging effects of the surrounding mesh dominate the dynamics [58, 83]. As indicated in Chapter 5, the phase of the surrounding network, as well as the degree of geometric anisotropy exhibited by the surrounding rods, will affect the density dependence of the probe caging behavior.

LC phases are also formed by solutions of *fd* virus; a semi-flexible rod with a very large aspect ratio, $L/D \sim 300$. Work studying the dynamics of a spherical protein shell, apoferritin, in *fd* virus suspension have shown complex dynamical behavior dependent upon the hydrodynamics and spherical tracer size [52, 102, 53]. Dynamics of a spherical tracer in a LC suspension of ellipsoid particles shows anisotropic diffusion as the phase transition from isotropic to nematic is approached [108].

Clearly, complex dynamics occur when a spherical probe is immersed in a system that has the ability to access different LC phases. In previous chapters, the effect of long-range orientational order was studied with stationary scatterers. Anisotropy in the diffusion of the probe was observed. Also, complex phase behavior depending on the field strength, aspect ratio and volume fraction of nematogens under the presence of an external rotating field have been observed. Thus, the question of whether the dynamics of a probe can be tuned by the parameters of the driving field and the nematogenic system is one worth exploring. In this work, a spherical probe is immersed in a system composed of hard nematogens driven by an external, rotating field. The field strength is held constant, and the rotating frequency is increased from a stationary aligning field to frequencies consistent with the Brownian frequency of rotation. The frequency dependent dynamics of the probe is explored and compared to the dynamical behavior of the nematogens in the system.

7.2 Model Details

The system studied contains a spherical probe in driven nematogens. The nematogens are modeled as spherocylinders, cylindrical particles with a hemispherical cap on each end. The geometric anisotropy of the nematogens is measured by the aspect ratio, the ratio of the length of the cylindrical portion of the nematogen to the diameter of the spherical end-cap, L/D. The data given in this chapter, corresponds to a nematogenic system of needles with aspect ratio, L/D=7, and a volume fraction of $\rho = 0.008$. The spherical probe has a diameter of 1 Å, identical to the diameter of the needle. The nematogen-nematogen interactions and the interaction between the nematogens and the spherical probe are modeled as hard wall interactions. The nematogens are driven by an external rotating field in the xy-plane of the simulation cell. The field strength is commensurate to a field of 60V applied across the thin film created by the simulation box. Similar field strengths have been used experimentally to follow the dynamics of the director in the presence of a pulsed field [65, 66, 70, 7, 77]. The nematogens interact with the external field through a dipole along the length of the long-axis of the nematogen. The dipole serves only to align the nematogen with the electric field, and are is considered in the nematogen-nematogen interactions.

Collisions between nematogens are found using the algorithm previously described by Robertus and Sando [89]. The algorithm to determine collisions between the spherical probe and the nematogens is a variation of the technique described in the work of Hansen and McDonald [40]. The collision algorithm finds collisions after the particles are overlapping between successive time steps, thus the particles must be translated and rotated backwards in time to the point of impact. Collision dynamics are then determined by calculating the impulse of the collision and the velocities are updated accordingly.

7.3 Results

7.3.1 Dynamics of the Driven Nematogens

Dynamics of the nematogens in the driven system are deduced by determining the translational diffusion coefficients via the mean-square displacement, the VACFs and the rotational

correlation functions. The translational diffusion coefficients for the nematogens normalized by the diffusion coefficient of the commensurate system without the presence of an external field are given in Figure 40. The black circles give the diffusion coefficients determined from the mean-square displacements while the red squares give the diffusion coefficients determined by exponential fits of the VACFs (the details of the fits are given in the text below). The frequency dependence of the diffusion coefficients show a spike in the mobility when the driving frequency is $\omega = 2ps^{-1}$. The phase behavior of nematogens under the presence of a rotating field was deduced in Chapter 6. As the driving frequency increases, the nematogens show an overall decrease in long-range order indicating that a decrease in mobility of the nematogens is expected. However, according to the diffusion coefficients shown in Figure 40, it appears at a frequency of $\omega = 2$ ps^{-1} the mobility of the nematogens is greater than at a frequency of 1 ps^{-1} or 3 ps-1.

The VACFs of the driven nematogens with respect to time for the driving frequencies studied are provided in Figure 41. The VACFs show a multi-exponential decay in Figure 41 but this behavior is better illustrated on the semi-log scale provided in Figure 42. The exponential decay at short times is shown by dashed curves in Figure 41, and are the fits used to determine the diffusion coefficients corresponding to the red squares in Figure 40. The multi-exponential behavior in the VACFs indicate that the translational diffusion process is not a simple Markovian process, but rather, the underlying physics is more complicated. Nematogens in the stationary field also show a slight deviation from a single exponential decay. The diffusion coefficients determined from the exponential fits diverge from those calculated from the MSD. The divergence is due to the fact that the VACFs are not fully described by a single exponential. The VACFs also show a lack of frequency dependence on the translational motion of the driven nematogens, but a significant difference exists between a strong aligning field and no field. We expect, however, that a stronger frequency dependence will emerge as the density of nematogens is increased due to the large number of collisions that will be induced by rotating a larger density of nematogens.

The rotational correlation functions of the driven nematogens with respect to time are shown in Figure 43 and on the semi-log scale in Figure 44. As the frequency of the rotating

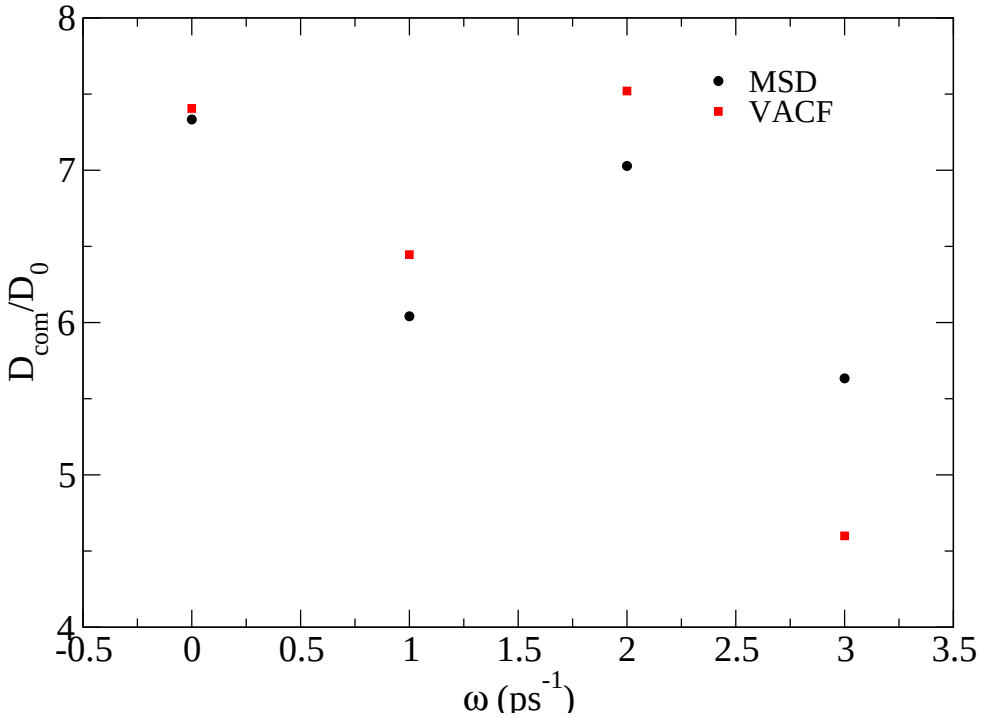

Figure 40: The translational diffusion coefficients for the nematogens with respect to frequency. The diffusion coefficients are normalized by the diffusion coefficients of the nematogens without the presence of an external driving field. Black circles are diffusion coefficients determined from the mean-square displacement and red squares are diffusion coefficients determined from fits to the velocity auto-correlation function.

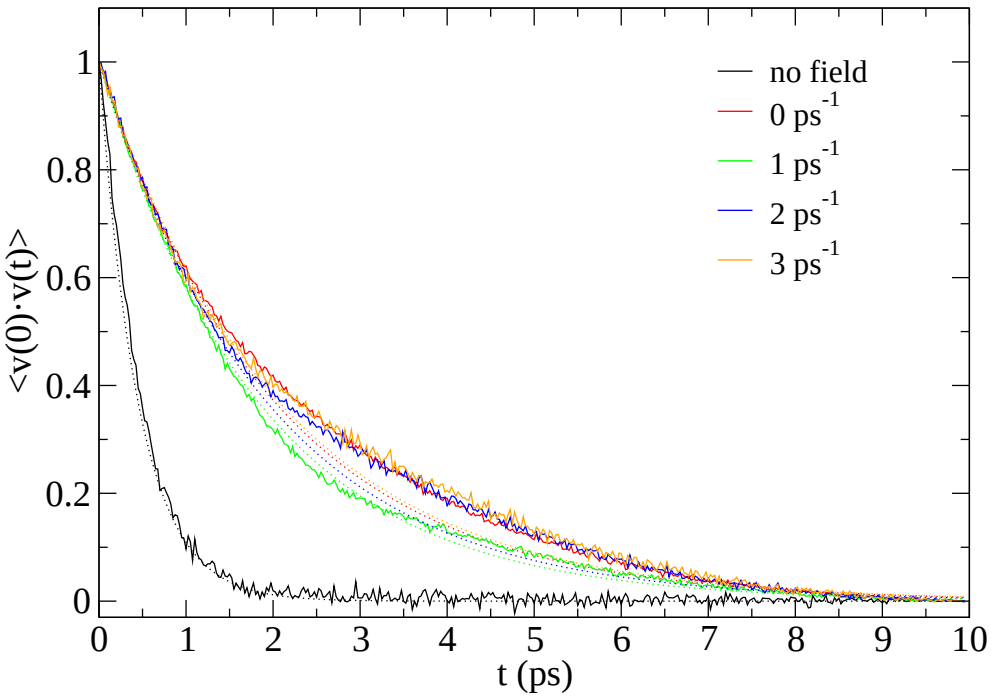

Figure 41: The VACFs for the driven nematogens as a function of time and frequency. The black curve corresponds to no field, red a driving frequency of 0 ps^{-1}, green, 1 ps^{-1}, blue 2 ps^{-1} and orange 3 ps^{-1}. The dashed lines show exponential fits to the VACFs.

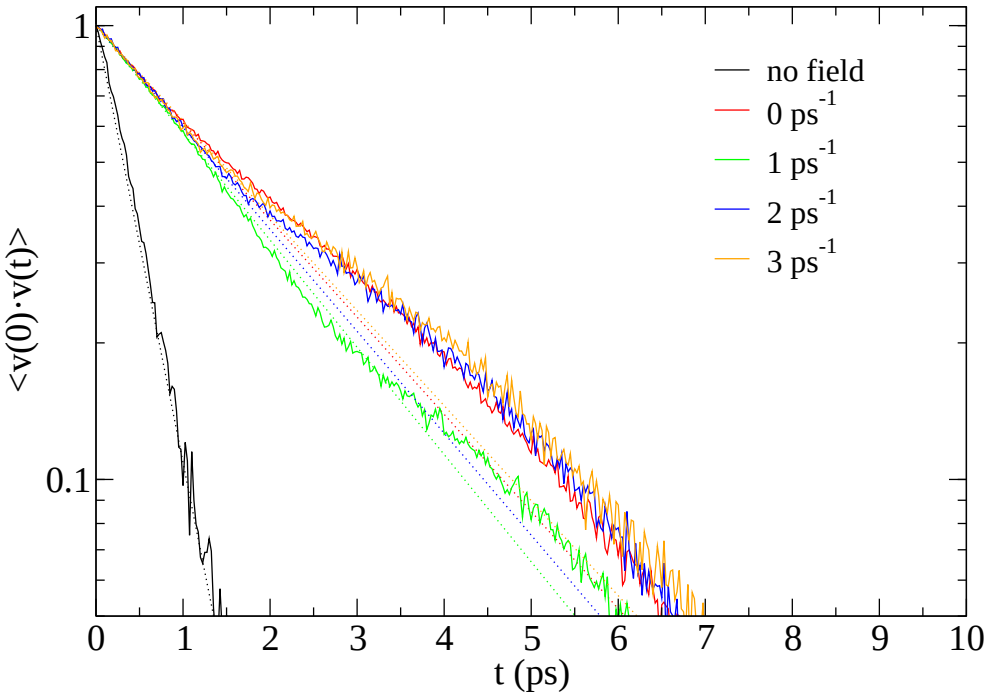

Figure 42: The VACFs for the driven nematogens as a function of time and frequency on a semi-log plot. The black curve corresponds to no field, red a driving frequency of 0 ps^{-1}, green, 1 ps^{-1}, blue 2 ps^{-1} and orange 3 ps^{-1}. The dashed lines show exponential fits to the VACFs.

field increases, rotational correlations persist at longer times. At short times, the rotational correlations in systems with a driving field, show very similar decay behavior. This trend is due to the torque induced on the particle, aligning the particles to the external field. The rotational correlations show, at low frequencies and without the presence of an external field, a decay behavior that is dominated by the behavior of a free rotor. The rotational correlation functions are defined as the ensemble average of the angle between the long-axis of the needle at a given time, t and t=0. For a free rotor, the orientational correlation function takes the form of $cos(\omega t)$ where ω is the frequency of the rotation of the free rotor. Because the model system is low density, the free rotor behavior is evident in the decay of the rotational correlations. As the frequency increases, the number of collisions in the system increases, and a transition to a multi-exponential decay in the rotational correlations is observed. In this particular system, collisions begin to dominate the rotational dynamics when the frequency reaches $\omega = 2\text{ps}^{-1}$. This transition is particularly evident when looking at the semi-log scale, given in Figure 44. We expect this transition in the rotational motion will not be as evident in systems with greater density of nematogens.

From Figures 41-44, it appears that the translational motion of the driven nematogens is not strongly coupled to their rotational motion. Only a weak frequency dependence is observed in the translational diffusion coefficients and in the VACFs, while a strong frequency dependence in the rotational behavior of the nematogens is seen. It is important to note that the presence of the electric field dramatically affects the translational dynamics of the nematogens. This is seen by noting that the diffusion coefficients of the nematogens, when under the influence of an external field, are far greater than the system without an external field. The coupling between the rotational motion and the translational motion should become more evident with increasing densities, as the number of collisions will increase and thus affect the translational and rotational dynamics.

7.3.2 Dynamics of the Spherical Probe

In the previous section, the data has indicated that there is a transition in the rotational motion of the nematogens as the frequency increases. The aim of this section is to deduce

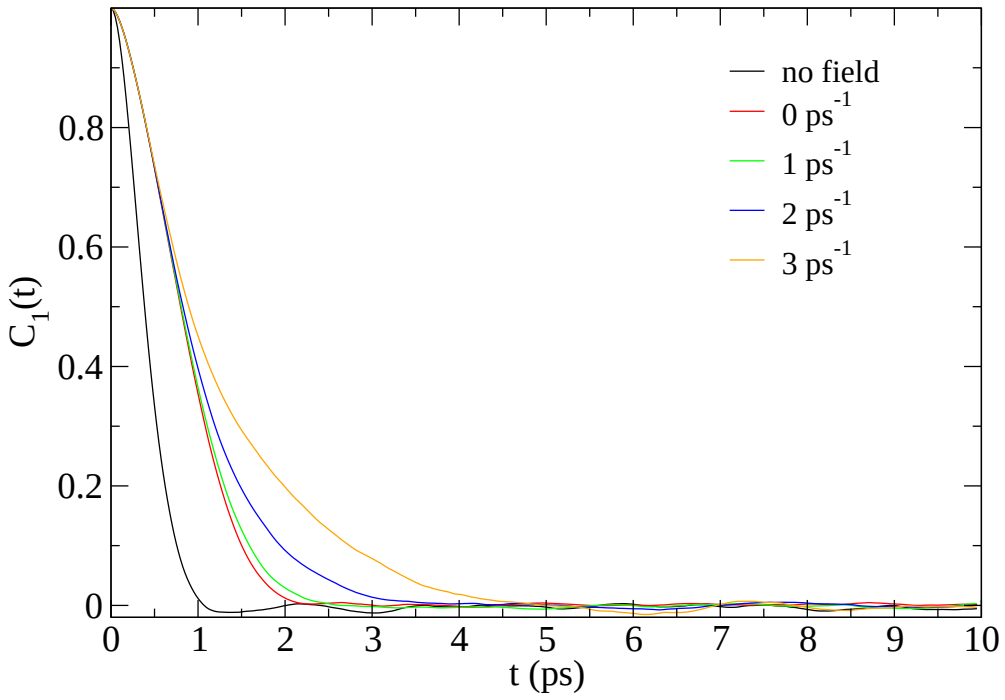

Figure 43: The rotational correlation functions for the driven nematogens with respect to time and frequency. The black curve corresponds to no field, red a driving frequency of 0 ps^{-1}, green, 1 ps^{-1}, blue 2 ps^{-1} and orange 3 ps^{-1}.

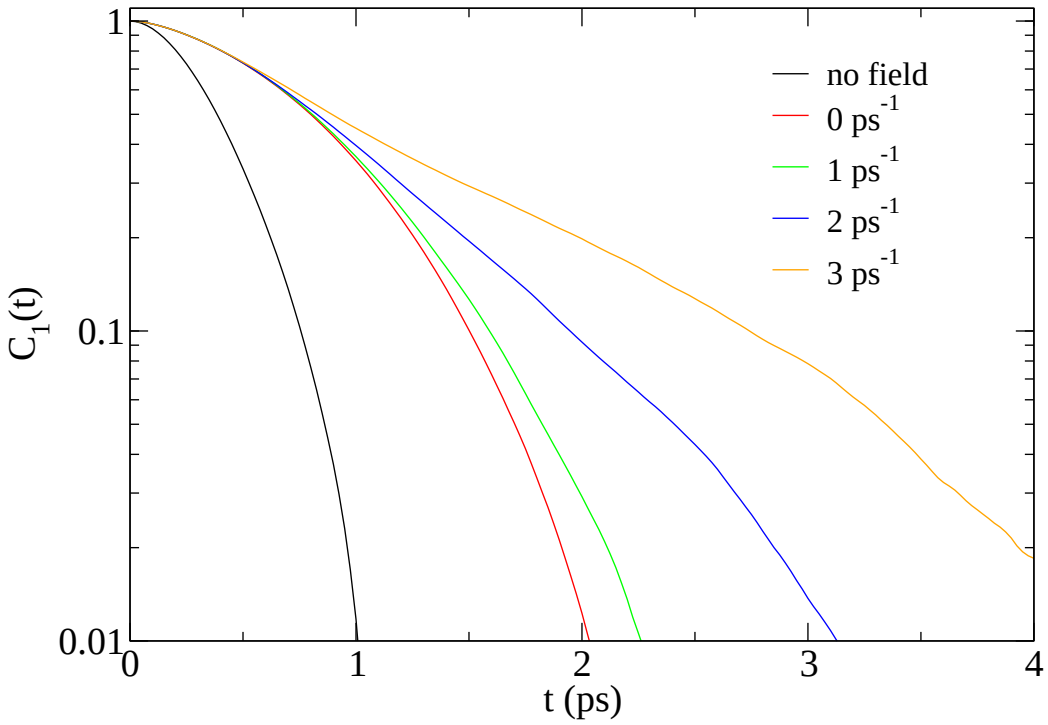

Figure 44: The rotational correlation function for driven nematogens with respect to time on a semi-log plot. The rotational correlations show multi-exponential decay, with the various dashed lines depicting exponential fits. Black circles depict correlations with no field, red squares for a driving frequency of 0 ps^{-1}, green diamonds 1 ps^{-1}, blue crosses 2 ps^{-1} and orange stars 3 ps^{-1}.

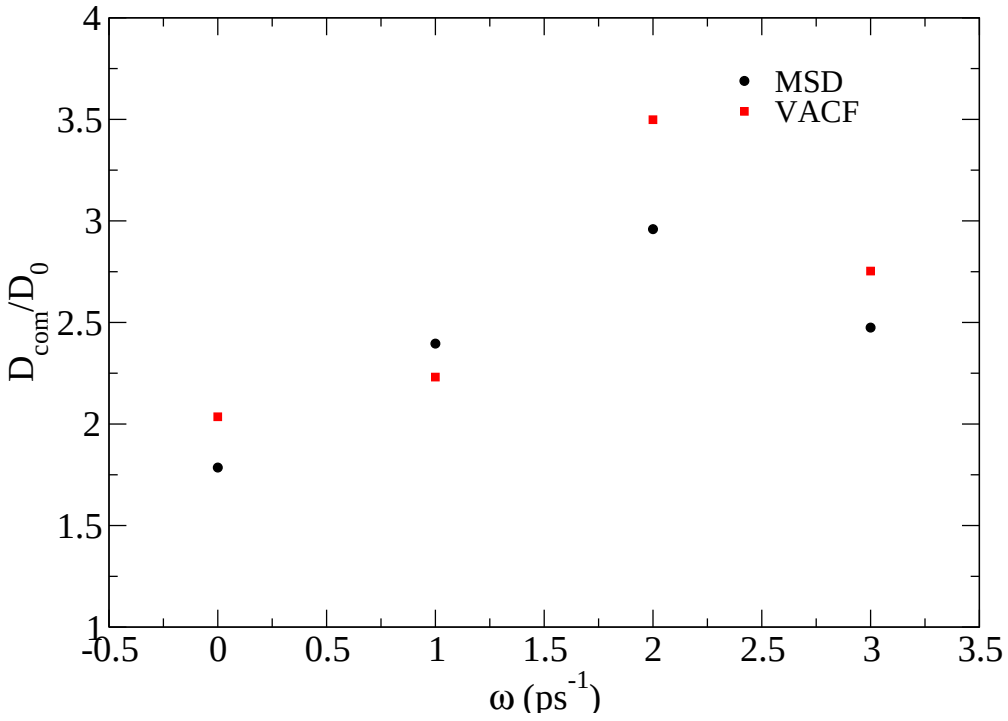

Figure 45: The translational diffusion coefficients for a spherical probe immersed in driven nematogens is given with respect to driving frequency. The black circles are determined using the mean-square displacement and the red squares are determined from fits to the VACFs.

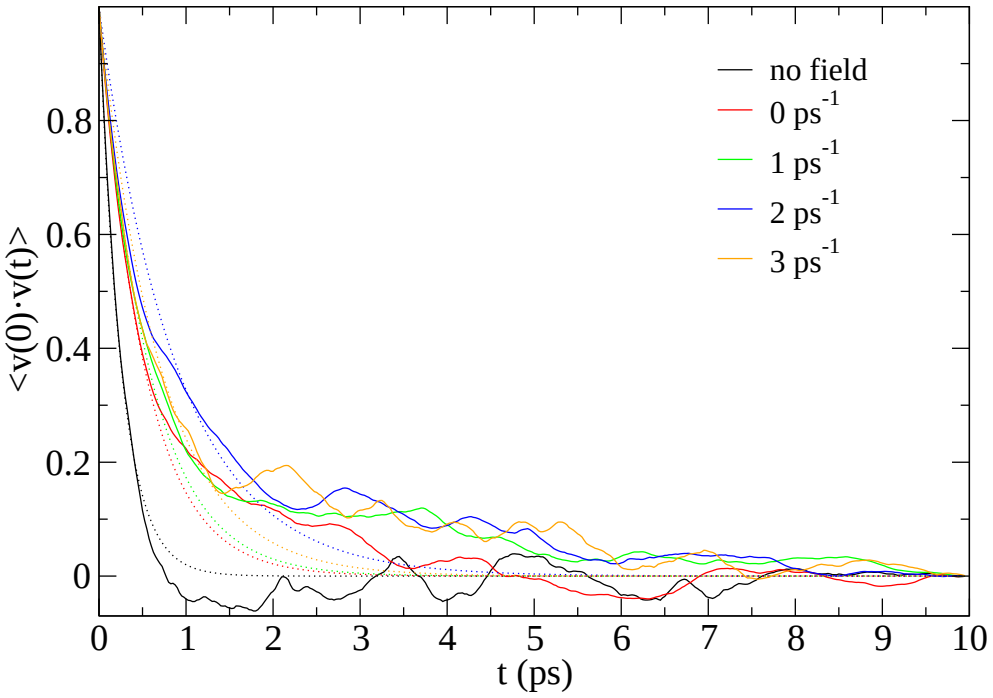

Figure 46: The velocity autocorrelation functions for the probe in driven nematogens with respect to time. The black curve corresponds to no field, red to a driving frequency of 0 ps^{-1}, green 1 ps^{-1}, blue 2 ps^{-1} and orange 3 ps^{-1}. Exponential fits used to determine the translational diffusion coefficients provided in Figure 45 are given by the dashed lines.

the effect of this transition on the dynamics of a spherical probe in the driven nematogens. The dynamics of a spherical probe immersed in the driven nematogens is deduced by calculating the translational diffusion coefficients using the mean-square displacements and VACFs. The probe is considered to be smooth, therefore, the rotational motion of the probe is not considered in this study. The diffusion coefficients of the probe are shown in Figure 45. The black circles are the diffusion coefficients determined using the mean-square displacement and the red squares are the diffusion coefficients determined by exponential fits to the VACFs. The diffusion coefficients for both methods show that at lower frequencies, the diffusion coefficient increases with increasing frequency, indicating that the frequency, enhances the translational motion of the spherical probe. However, at a frequency of ω =2 ps^{-1} the rotational motion of the nematogens changes as shown in Figures 43-44. Therefore, the behavior of the probe changes as well, and is reflected in the data shown in Figures 45-46.

The VACFs of the spherical probe are given in Figure 46 where the solid curves depict the data and the dotted lines show the exponential fits. As was seen in the VACFs of the nematogens, the correlations in the velocity exhibit a multi-exponential decay under the presence of an external rotating field. As stated previously, this is indicative of complex physics in the underlying dynamics of the probe and shows that the dynamics of the probe is not a Markovian process. We observe that the single exponential fit is increasingly inaccurate as the frequency increases, as is evident by the diverging diffusion coefficients calculated from the exponential fits to the VACFs with respect to the diffusion coefficients determined from the MSD, seen in Figure 45. As the frequency increases, the diffusion of the probe increases due to increasing correlations in the rotational behavior of the nematogens and the directional collisions of the probe along the nematogens. When the collisions dominate the rotational behavior of the nematogens, the diffusion of the probe decreases, indicating a strong coupling in the dynamics of the probe and the rotational motion of the nematogens.

7.4 Concluding Remarks

In this work, the effect of an external rotating field on the dynamics of a spherical probe immersed in nematogens is studied. The results are for low nematogen density with relatively large aspect ratios. The frequency dependence of the dynamics of the driven nematogens are compared to the frequency dependent behavior of the spherical probe. The driven nematogens show only slight frequency dependent behavior in their translational motion. However, a strong effect is observed when the system is under the influence of the field as compared to the system with no field. The rotational motion of the nematogens, indicated by determining the decay behavior of the rotational correlation functions, show a strong frequency dependence. A transition from free rotor dominated behavior to collision dominated behavior is observed, indicated by the change in the form of the decay of the rotational correlation function. The transition to collision dominated behavior occurs at a frequency of $\omega = 2$ ps^{-1}. A weak coupling between the translational motion of the nematogens and their rotational motion is observed, but is expected to become more prevalent at

larger densities of nematogens.

The dynamics of the probe show a strong coupling to the rotational motion of the nematogens. The translational diffusion of the probe increases with increasing frequency until the transition to collision dominated rotational behavior of the nematogens occurs, accompanied by a downturn in the probe diffusion coefficients. An increase in velocity correlations upon the introduction of the driving field is observed, due to directional collisions along the cylindrical axis of the particles, in conjunction with the increase in correlations of the orientations of the nematogens. This behavior is similar to that observed in the diffusion of a spherical probe in stationary nematic networks studied in Chapter 5.

Collectively, these results and those provided in the Chapter 5, show that the dynamics of a spherical probe is influenced by altering the parameters of an external, rotating field. It is also clear that more studies are needed to determine the density dependence of this behavior, as well as the dependence on aspect ratio, which would be helpful in deducing the apparent transition in the rotational motion of the system.

CHAPTER VIII

CONCLUSIONS AND FUTURE WORK

8.1 Concluding Remarks

8.1.1 Diffusion of a Thick Needle Through Stationary Scatterers

Throughout this thesis, Lorentz models with geometrically anisotropic scatterers and probes have been studied by molecular dynamics simulations. In systems where the freely translating and rotating probe is a needle with finite thickness, rich dynamical regimes are observed. At low densities, the translational diffusion coefficients of the needle follow the expected Enskog behavior, the diffusion coefficients follow the relation, $D \sim 1/n^*$, where n^* is the reduced scatterer density. As the scatterer density is increased, a crossover to reptative behavior is seen. Reptation is due to enhance motion parallel to the axis of the needle, while motion perpendicular to the axis and the rotational motion of the needle are severely suppressed. Movement through the effective Edwards tubes created by the scatterer network, causes an enhancement in the translational diffusion coefficients which had been previously observed in the diffusion of an infinitely thin needle in stationary point scatterers [47, 48], as well as in fluids of rigid, infinitely thin needles [23]. By increasing the scatterer density further, a glassy transition is eventually observed when translational diffusion coefficients decrease due to geometric trapping of the needle in the surrounding scatterers. These dynamical transitions occur because of the geometric anisotropy of the needle probe and structure of the surrounding stationary scatterers. When a system composed of a three-dimensional network of scatterers is considered, the enhanced regimes previously observed in two-dimensions are no longer observed, indicating a fragility of the formation of Edwards tubes on the surrounding medium. In a three-dimensional model, the excluded volume of the stationary scatterers (now spheres in three-dimensions) effectively cut off Edwards tubes. Therefore, a competition between end-cap collisions, now more prevalent, and the reptative motion of the needle is seen. In this system, the end-cap

collisions dominate the dynamics. On the other hand, in the two-dimensional system, an increase in end-cap collisions is observed, but the majority of collisions driving the motion are between the scatterer and the cylindrical portion of the needle. The dynamics of macromolecules diffusing through structured materials exhibit dynamical regimes expressed by the Lorentz models studied in this thesis. The competition caused by the length scales of the scatterer with respect to the length scales that characterize the surrounding structure connect to the diffusion of guest molecules through structured material and porous gels.

8.1.2 Diffusion of a Spherical Probe Through Stationary Nematogens

A Lorentz model that is comprised of stationary, needle-like scatterers and a freely translating spherical probe was studied with MD and shows rich dynamical behavior as well. When scatterers possess geometric anisotropy, it is possible to vary the orientational order of the scatterers. In this work, we studied isotropically orientated scatterers, as well as scatterers oriented along a director, a stationary nematic phase. By inducing long range order (*i.e.* the nematic phase) anisotropic diffusion of the spherical probe is observed. This behavior is caused by the formation of effective tubes created by the long-range order of the scatterers. The diffusion of spherical probes through a variety of liquid crystal systems, and a spherical probe through colloidal rods and stiff polymers also displays non-trivial diffusive behavior. We observed that the geometric trapping exhibited by the spherical probe is staved off when the particles are orientated along some director. The presence of long-time tails of the velocity autocorrelation functions is also seen, a well-known phenomenon in liquids. A power-law like decay of the negative long-time tails was seen, which is consistent with previously described long-time tails of other Lorentz models. The onset of negative time tails occurs when the diffusion coefficients, calculated from the mean-square displacement, show trapping due to the surrounding scatterers creating an effective cage. The results provided for this Lorentz model are directly applicable to more complex systems that exhibit geometric and spatial anisotropy. These systems include diffusion of solutes through liquid crystals and ordered arrays. The stark difference in the transport quantities measured for systems possessing long-range order and those that do not, provide insight into such systems.

8.1.3 Phase Behavior with Respect to Frequency and Field Strength

In this thesis, the phase behavior of liquid crystal systems under the presence of a rotating, external field was investigated. Through numerical simulation, we were able to describe the frequency dependence of the phase behavior of hard nematogens. With a stationary frequency, $\omega = 0$ ps^{-1}, long-range order was stabilized. By increasing the frequency of the rotating the field, however, long range order is lost. This is due to the librational motion induced around the aligning field and the difficulty of the particles to follow the electric field. Disruption in long-range order is also seen to become more severe with increasing aspect ratio and volume fraction of the nematogens. Results show that at a specific frequency of $\omega = 0.5$ ps^{-1}, reentrant phase behavior is exhibited. At low field strengths, the precessing motion of the nematogens around the electric field disrupts long range order. As the field strength increases, the particles follow the electric field more easily and thus give rise to an increase in long range order. This work lends knowledge in understanding how to drive liquid crystals to other phases that may not be accessible without some external perturbation.

8.1.4 Dynamics of a Spherical Probe in Driven Nematogens

The effect of a rotating, external electric field on the dynamics of a probe through nematogens has also been elucidated in this thesis. The dynamics of the spherical probe and of the driven nematogens are observed to be a function of the frequency. The translational diffusion coefficients of the probe appear to be greatly affected by the rotational motion of the nematogens. Multi-exponential decay is observed in both the VACFs and the rotational correlations of the driven nematogens, indicating complex physics underlying the dynamics of the nematogens. The spherical probe also exhibited multi-exponential decay in the VACFs. These results support the idea that the dynamics of the probe can be controlled by changing the parameters of the external field.

8.1.5 Overarching Conclusions

Overall, this work has studied a variety of simple models that possess geometric and spatial anisotropy that are relevant to a wide variety of liquid and soft matter systems, ranging from

the environment produced by the cytoplasm in the cell to micro- and nano-porous materials with inherent pores and channels. By tuning simple geometric parameters, densities and external perturbations, we were able to access dynamical and phase behaviors not normally observed.

8.2 Future Work

One potential extension to this work would be to add another layer of complexity to the simple models, such as attractive interactions between particles or a surrounding solvent. The solvent can be modeled as a Brownian or Langevin solvent, dampening the tracer diffusion and also stabilizing rotational fluctuations caused by the torque of an external field. Work on a Brownian walker in stationary media has shown interesting behavior. Surprisingly, even when the tracer is dampened, long time tails still present themselves in the dynamics [30]. Useful insight into the origins of the persisting time tails would be gained by a direct comparison between the ballistic simulations presented in this thesis and the numerical results of damped Lorentz models of needles with finite thickness, as well as a probe diffusing through stationary needles. Presumably, the hydrodynamic effects of a surrounding fluid along with the stationary scatterers would lead to complex behavior in the dynamics of the probe. Additionally, dampening the motion of the nematogens would aid in stabilizing the precessing motion observed when the nematogens are in the presence of an external field, thus stabilizing long range order. However, the fluid and hydrodynamic effects would greatly affect the ease in which the nematogens follow the driving external field, destabilizing the long-range order. The competition between these two phenomena is worth investigating. Furthermore, adding a more complex inter-particle potential would certainly provide some valuable insight. With attractive interactions, it would be possible to observe clustering in the nematogens when the electric field has induced a dipole in the nematogens. The structural behavior of the nematogens could be strongly coupled to the well depth and the parameters of the driving field.

Experimental studies, like those of Roichman et. al, can be completed to investigate the numerical findings of the Lorentz models described [92, 91, 93, 38, 94]. Optical traps can

be used to generate static arrays of scatterers in many configurations. Such experimental studies would enhance the numerical and theoretical descriptions provided in this thesis. Also, experimental studies of LC particles in the presence of a rotating external field would add significant value. As described previously, a large body of work exists studying the dynamics of the director in pulsed fields via spectroscopic techniques [61, 10, 65, 66, 70, 7, 77]. Measurement of the twist viscosity coefficient of two LC compounds has been determined by studying the effect of slow rotating magnetic fields [88]. More recently, experimental work has been completed on the effect of rotating magnetic fields on silicon transport in the liquid phase during the growth of SiGe. Specifically, a rotating frequency of 40 Hz was used, indicating that such experimentation is possible and has been accomplished [4].

It would also be valuable to study more complicated particle geometries. For example, making the needle in the Lorentz models or the nematogenic particle semi-flexible would create a more realistic model for complex polymer systems and provide non-uniform dynamics and phase behaviors. Reptative motion of the needles would still be observed, but perhaps altering the rigidity of the needle would change the dynamic transitions observed between reptative motion, glassy behavior etc. Perhaps by inducing some flexibility, the entrapment observed in a needle in stationary media would be staved off due to the ability of the needle to access more tubes by allowing it to bend and flex.

In addition, Lorentz models with varying scatterer realizations could be studied. Forming patterns with the scatterer molecules could recreate the structure formed by mesoporous materials [100, 101] that produce anisotropic diffusion of the guest molecules. It would also be valuable to follow more than one tagged particle through the stationary scatterers, creating a binary mixture of very small mass particles with very large mass particles. Such systems have been studied previously [59, 97], but do not possess the geometric anisotropy of the particles studied in this thesis.

A theoretical description of the dynamical transitions observed in a thick two-dimensional needle would also provide insight into the competing processes that give rise to this behavior. It is possible to look at the transport of the needle when the scatterer density is sufficiently high to induce reptation, as a series of reflections parallel to the long-axis of the needle

and rattles perpendicular to the needle. The average time between reflections is quite large relative to the time between rattles. Thus, a hopping mechanism from one reflection to another could be used to develop a simple theoretical description of transport of the thick needle through an Edwards tube.

It is also necessary to complete a more thorough study of the frequency dependent dynamics of a spherical probe in driven nematogens. In this work, only one density and aspect ratio is explored and in order to obtain a clear picture of the behavior of this system, more densities as well as aspect ratios need to be studied. Additionally, studying a wider range of frequencies would also be valuable in order to fully characterize the apparent transition in the rotational motion of the nematogens that seems to affect the translational diffusion.

An abundance of rich dynamical and phase information can be obtained by studying the simple models investigated in this thesis and a large amount of work still remains to be finished. Connections to a wide range of systems, makes the study of these models exceedingly valuable. Furthermore, adding to the value in studying these models is the ease in which the dynamics and phase of the models can be tuned by changing geometric parameters and density.

REFERENCES

[1] Åkerman, B., "Ring-polymer dynamics in gels: Supercoiled and relaxed circular DNA in polyacrylamide," *J. Phys. Chem. B*, vol. 102, pp. 8909–8922, 1998.

[2] Alder, B. and Wainwright, T., "Decay of the velocity autocorrelation function," *Phys. Rev. A*, vol. 1, pp. 18–21, 1970.

[3] Allen, M. and Tildesley, D., *Computer Simulation of Liquids*. Oxford University Press, 1987.

[4] Armour, N. and Dost, S., "Silicon transport under rotating and combined magnetic fields in liquid phase diffusion growith of SiGe," *Cryst. Res. Technol.*, vol. 45, pp. 335–340, 2010.

[5] Bates, M. and Luckhurst, G., "Computer simulation studies of anisotropic systems. XXX. The phase behavior and structure of a gay-berne mesogen," *J. Chem. Phys.*, vol. 110, pp. 7087–7107, 1999.

[6] Bausch, A. and Kroy, K., "A bottom-up approach to cell mechanics," *Nat. Phys.*, vol. 2, pp. 231–238, 2006.

[7] Bender, M., Holstein, P., and Geschke, D., "Electrically induced dyamic processes in nematic liquid crystals: 1H nuclear magnetic resonance investigations," *J. Chem. Phys.*, vol. 113, pp. 2430–2439, 2000.

[8] Bruin, C., "Logarithmic terms in the diffusion coefficient for the Lorentz gas," *Phys. Rev. Lett.*, vol. 29, pp. 1670–1674, 1972.

[9] Bruin, C., "A computer experiment on diffusion in the Lorentz gas," *Physica*, vol. 72, pp. 261–286, 1974.

[10] Carr, S. G., Luckhurst, G. R., Poupko, R., and Smith, H. J., "The director distribution in a spinning nematic mesophase subject to a static magnetic field," *Chem. Phys.*, vol. 7, 1975.

[11] Chandler, D., "Translation and rotational diffusion in liquids. II Orientational single-particle correlation functions," *J. Chem. Phys.*, vol. 60, p. 3508, 1974.

[12] Chandrasekhar, S., "Stochastic problems in physics and astronomy," *Rev. Mod. Phys.*, vol. 15, p. 1, 1943.

[13] Chernov, N. and Dettmann, C., "The existence of Burnett coefficients in the periodic Lorentz gas," *Physica A*, vol. 279, pp. 37–44, 2000.

[14] Cladis, P., "New liquid-crystal phase diagram," *Phys. Rev. Lett.*, vol. 35, pp. 48–51, 1975.

[15] Cladis, P., Bogardus, R., and Aasden, D., "High-pressure investigation of the reentrant nematic bilayer smectic-A transition," *Phys. Rev. A*, vol. 18, pp. 2292–2306, 1978.

[16] Cladis, P., Bogardus, R., Daniels, W., and Taylor, G., "High-pressure investigation of the reentrant nematic-bilayer-smectic-A transition," *Phys. Rev. Lett.*, vol. 39, pp. 720–723, 1977.

[17] Cuetos, A., Martínez-Haya, B., and Lago, S., "Liquid crystal behavior of the Kihara fluid," *Phys. Rev. E*, vol. 68, p. 011704, 2003.

[18] Cusmin, P., Salud, J., Lopez, D., de la Fuente, M., Diez, S., Pérez-Jubindo, M., Barrio, M., and Ll.Tamarit, J., "Re-entrant nematic behavior in the 7OCB+9OCB mixtures: Evidence for multiple nematic-smectic tricritical points," *J. Phys. Chem. B*, vol. 110, pp. 26194–26203, 2006.

[19] de Gennes, P. G., "Reptation of a polymer chain in the presence of fixed obstacles," *J. Chem. Phys.*, vol. 55, p. 572, 1971.

[20] de Miguel, E., Blas, F., and del Río, E., "Molecular simulation of model liquid crystals in a strong aligning field," *Mol. Phys.*, vol. 104, pp. 2919–2921, 2006.

[21] de Miguel, E. and del Río, E., "Computer simulation of nematic reentrance in a simple molecular model," *Phys. Rev. Lett.*, vol. 95, pp. 217802–1–217801–4, 2005.

[22] Dhara, D. and Chatterji, P. R., "Electrophoretic transport of poly(ehtylene glycol) chains through poly(acrylamide) gel," *J. Phys. Chem. B*, vol. 103, pp. 8458–8461, 1999.

[23] Doi, M. and Edwards, S., "Dynamics of rod-like macromolecules in concentrated solution," *J. Chem. Soc. Faraday Trans.*, vol. 74, pp. 560–570, 1978.

[24] Domenici, V., Marini, A., Veracini, C., Zhang, J., and Dong, R., "Effect of the magnetic field on the supramolecular structure of chiral smectic C phases: ^{2}H NMR studies," *ChemPhysChem*, vol. 8, pp. 2575–2587, 2007.

[25] Ernst, M., Machta, J., Dorfman, J., and van Beijeren, H., "Long time tails in stationary random media. I. Theory," *J. Stat. Phys.*, vol. 34, pp. 477–495, 1984.

[26] Ernst, M. and Weyland, A., "Long time behaviour of the velocity auto-correlation function in a Lorentz gas," *Phys. Lett.*, vol. 34A, pp. 39–40, 1971.

[27] F. Höfling, T. F. and Frey, E., "Localization transition of the three-dimensional Lorentz model and continuum percolation," *Phys. Rev. Lett.*, vol. 96, p. 165901, 2006.

[28] Fakhri, N., MackKintosh, F. C., Lounis, B., Cognet, L., and Pasquali, M., "Brownian motion of stiff filaments in a crowded environment," *Science*, vol. 330, pp. 1804–1807, 2010.

[29] Fernández, P., Grosser, S., and Kroy, K., "A unit-cell approach to the nonlinear rheology of biopolymer solutions," *Soft Matter*, vol. 5, pp. 2047–2056, 2009.

[30] Franosch, T., Höfling, F., Bauer, T., and Frey, E., "Persistent memory for a Brownian walker in a random array of obstacles," *Chem. Phys.*, vol. 375, pp. 540–547, 2010.

[31] Frenkel, D., Lekkerkerker, H., and Stroobants, A., "Themodynamic stability of a smectic phase in a system of hard rods," *Nature*, vol. 332, pp. 822–823, 1988.

[32] Frenkel, D. and Maguire, J., "Molecular dynamics study of infinitely thin hard rods: Scaling behavior of transport properties," *Phys. Rev. Lett.*, vol. 47, pp. 1025–1028, 1981.

[33] Frenkel, D. and Maguire, J., "Molecular dynamics study of the dynamical properties of an assembly of infinitely thin hard rods," *Mol. Phys.*, vol. 49, pp. 503–541, 1983.

[34] Frenkel, D., "Structure of hard-core models for liquid crystals," *J. Phys. Chem.*, vol. 92, pp. 3280–3284, 1988.

[35] Gay, J. G. and Berne, B. J., "Modification of the overlap potential to mimic a linear site site potential," *J. Chem. Phys.*, vol. 74, p. 3361, 1981.

[36] Gong, J. P., Hirota, N., Kakugo, A., Narita, T., and Osada, Y., "Effect of aspect ratio on protein diffusion in hydrogels," *J. Phys. Chem. B*, vol. 104, pp. 9904–9908, 2000.

[37] Gordon, R. G., "On the rotational diffusion of molecules," *J. Chem. Phys.*, vol. 44, p. 1830, 1966.

[38] Grier, D. G., Lee, S.-H., Roichman, Y., and Roichman, Y., "Assembling mesoscopic systems with holographic optical traps," *Proc. SPIE*, vol. 64833, pp. 64830D–1, 2007.

[39] Guan, Y., Ming Xu, Z. L., Xu, N., Lu, Z., Han, Q., Zhang, Y., and Zhao, X. S., "Heterogeneous transportation of α_{1B}-adrenoceptor in living cells," *Biophysical Chemistry*, vol. 127, pp. 149–154, 2007.

[40] Hansen, J. P. and McDonald, I. R., *Theory of Simple Liquids*. San Diego: Academic Press, 1986.

[41] Härtel, A., Blaak, R., and Löwen, H., "Towing, breathing, splitting and overtaking in driven colloidal liquid crystals," *Phys. Rev. E*, vol. 81, p. 051703, 2010.

[42] Hashim, R., Luckhurst, G., and Romano, S., "Computer simulation studies of anisotropic systems. XVIII. Re-entrant phase seperation in nematogenic mixtures of cylindrical and spherical particles," *Proc. R. Soc. London, Ser. A.*, vol. 429, pp. 323–339, 1990.

[43] Hernandez, R. and Somer, F. L., "Stochastic dynamics in irreversible nonequilibrium environments. 1. The fluctuation-dissipation relation," *J. Phys. Chem. B*, vol. 103, pp. 1064–1069, 1999.

[44] Hernandez, R. and Somer, F. L., "Stochastic dynamics in irreversible nonequilibrium environments. 2. A model for thermosetting polymerization," *J. Phys. Chem. B*, vol. 103, pp. 1070–1077, 1999.

[45] Hershkovits, E. and Hernandez, R., "Chemical reaction dynamics within anisotropic solvents in time-dependent fields," *J. Chem. Phys.*, vol. 122, p. 014509, 2005.

[46] Höfling, F. and Franosch, T., "Crossover in the slow decay of dynamic correlations in the Lorentz model," *Phys. Rev. Lett.*, vol. 98, p. 140601, 2007.

[47] Höfling, F., Frey, E., and Franosch, T., "Enhanced diffusion of a needle in a planar array of point obstacles," *Phys. Rev. Lett.*, vol. 101, p. 120605, 2008.

[48] Höfling, F., Munk, T., Frey, E., and Franosch, T., "Entangled dynamics of a stiff polymer," *Phys. Rev. E*, vol. 77, p. 060904(R), 2008.

[49] Hosing, M., Nakano, H., and Kimura, H., "Nematic-smectic transition in an aligned rod system," *J. Phys. Soc. Jap.*, vol. 46, pp. 1709–1715, 1979.

[50] Janeček, J. and Boublík, T., "Monte Carlo study of dipolar and quadropolar hard prolate spherocylinders," *Mol. Phys.*, vol. 104, pp. 197–210, 2006.

[51] Kang, K., Wilk, A., Patowski, A., and Dhont, J., "Diffusion of spheres in isotropic and nematic networks of rods: Electrostatic interactions and hydrodynamic screening," *J. Chem. Phys.*, vol. 126, pp. 214501–1:17, 2007.

[52] Kang, K., Gapinski, J., Lettinga, M. P., Buitenhuis, J., Meier, G., Ratajczyk, R., Dhont, J. K. G., and Patkowski, A., "Diffusion of spheres in crowded suspensions of rods," *J. Chem. Phys.*, vol. 122, pp. 044905–1:13, 2005.

[53] Kang, K., Wilk, A., Buitenhuis, J., Patkowski, A., and Dhont, J. K. G., "Diffusion of spheres in isotropic and nematic suspensions of rods," *J. Chem. Phys.*, vol. 124, pp. 044907–1:17, 2006.

[54] K as, J., Strey, H., and Sackmann, E., "Direct imaging of reptation for semiflexible actin filaments," *Nature*, vol. 368, pp. 226–229, 1994.

[55] Kihara, T., "Convex molecules in gaseous and crystalline states," *Adv. Chem. Phys.*, vol. 5, pp. 147–188, 1963.

[56] Kim, K., Miyazaki, K., and Saito, S., "Slow dynamics in random media: Crossover from glass to localization transition," *Europhys. Lett.*, vol. 88, pp. 36002–p1–36002–p5, 2009.

[57] Kimich, R. and Fatkullin, N., "Anisotropy of the segment mobility versus self- and pair-correlation functions in polymer melts under mesoscopic confinement," *Macromolecules*, vol. 43, pp. 9821–9827, 2010.

[58] Kluigtmans, S., Koenderink, G., and Philipse, A., "Self-diffusion and sedimentation of tracer spheres in (semi)dilute dispersions of rigid colloidal rods," *Phys. Rev. E*, vol. 61, pp. 626–636, 2000.

[59] Kurzidim, J., Coslovich, D., and Kahl, G., "Single-particle and collective slow dyanmics of colloids in porous confinement," *Phys. Rev. Lett.*, vol. 103, pp. 138303–1–139303–4, 2009.

[60] Lennard-Jones, J., "On the determination of molecular fields. II. From the equation of state of a gas," *Proc. R. Soc. Lond. A*, vol. 106, pp. 463–477, 1924.

[61] Leslie, F. M., Luckhurst, G. R., and Smith, H. J., "Magnetohydrodynamic effects in the nematic mesophase," *Chem. Phys. Lett.*, vol. 13, 1972.

[62] Lewis, J. C. and Tjon, J., "Evidence for slowly-decaying tails in the velocity autocorrelation function of a two-dimensional Lorentz gas," *Phys. Lett.*, vol. 66A, pp. 349–351, 1978.

[63] Lieleg, O., Schmoller, K. M., Cyron, C. J., Luan, Y., Wall, W. A., and Bausch, A. R., "Structural polymorphism in heterogeneous cytoskeletal networks," *Soft Matter*, vol. 5, pp. 1796–1803, 2009.

[64] Lowe, C., Frenkel, D., and van der Hoef, M., "Deviations from Fick's law in Lorentz gases," *J. Stat. Phys.*, vol. 87, pp. 1229–1244, 1996.

[65] Luckhurst, G. R., Miyamoto, T., Sugimura, A., and Timimi, B. A., "Director reorientation processes in a monodomain thin nematic liquid crystal film: A deuterium NMR spectroscopy study," *J. Chem. Phys.*, vol. 117, pp. 5899–5907, 2002.

[66] Luckhurst, G. R., Miyamoto, T., Sugimura, A., Timimi, B. A., and Zimmermann, H., "Electric-field driven director oscillations in a nematic liquid crystal: A NMR investigation," *J. Chem. Phys.*, vol. 121, pp. 1928–1937, 2004.

[67] Machta, J., Ernst, M., and Dorfman, J., "Long time tails in stationary random media II: Applications," *J. Stat. Phys.*, vol. 35, pp. 413–442, 1984.

[68] Magda, J., Davi, H., and Tirrell, M., "The transport properties of rod-like particles via molecular dynamics. I. Bulk fluid," *J. Chem. Phys.*, vol. 85, pp. 6674–6685, 1986.

[69] McGrother, S. C., Williamson, D. C., and Jackson, G., "A re-examination of the phase diagram of hard spherocylinders," *J. Chem. Phys.*, vol. 104, pp. 6755–6771, 1996.

[70] Mitsuishi, M., Ito, S., Yamamoto, M., Fischer, T., and Knoll, W., "Time-resolved optical waveguide study of the reorientation in a nematic liquid crystal under applied electric field," *J. Appl. Phys*, pp. 1135–1142, 1997.

[71] Moix, J. M. and Hernandez, R., "Dissipating the Langevin equation in the presence of an external stochastic potential," *J. Chem. Phys.*, vol. 122, p. 114111, 2005.

[72] Moix, J. M., Hernandez, R., and Pollak, E., "The momentum and velocity autocorrelation functions of a diatomic molecule are not necessarily proportional to each other," *J. Phys. Chem. B*, vol. 112, pp. 213–218, 2008.

[73] Moix, J. M., Shepherd, T. D., and Hernandez, R., "A phenomenological model for surface diffusion: Diffusive dynamics across incoherent stochastic aperiodic potentials," *J. Phys. Chem. B*, vol. 108, pp. 19476–19482, 2004.

[74] Moreno, A. and Kob, W., "Dynamics of a rigid rod in a glassy medium," *Europhys. Lett.*, vol. 67, pp. 820–826, 2004.

[75] Moreno, A. and Kob, W., "Relaxation dynamics of a linear molecule in a random static medium: A scaling analysis," *J. Chem. Phys.*, vol. 121, pp. 380–386, 2004.

[76] Munk, T., Höfling, F., and Franosch, T., "Effective perrin theory for the anisotropic diffusion of a strongly hindered rod," *Europhys. Lett.*, vol. 85, p. 30003, 2009.

[77] Ogaki, H., Okumoto, K., Sugimua, A., and Zimmermann, H., "Director dynamics in a monodomain thin smectic liquid crystal film," *Thin Solid Films*, vol. 499, pp. 249–255, 2006.

[78] Onsager, L., "The effects of shape on the interaction of colloidal particles," *Ann. N.Y. Acad. Sci.*, vol. 51, pp. 627–659, 1949.

[79] Otto, M., Aspelmeier, T., and Zippelius, A., "Microscopic dynamics of thin hard rods," *J. Chem. Phys.*, vol. 124, p. 154907, 2006.

[80] Parsons, J., "Nematic ordering in a system of rods," *Phys. Rev. A*, vol. 19, pp. 1225–1230, 1979.

[81] Peizl, G., Diele, S., Latif, I., Weissflog, W., and Demus, D., "A reentrant nematic phase in the binary system of two terminal-nonpolar compounds," *Cryst. Res. Tech.*, vol. 17, pp. K78–K82, 1982.

[82] Perkins, T., Smith, D., and Chu, S., "Direct observation of tube-like motion of a single polymer chain," *Science*, vol. 264, pp. 819–822, 1994.

[83] Philipse, A. and Kluijtmans, S., "Sphere caging by a random fibre network," *Physica A*, vol. 274, pp. 516–524, 1999.

[84] Poniewierski, A. and Sluckin, T., "Phase diagram for a system of hard spherocylinders," *Phys. Rev. A*, vol. 43, pp. 6837–6842, 1991.

[85] Popov, A. V. and Hernandez, R., "The ontology of temperature in nonequilibrium systems," *J. Chem. Phys.*, vol. 126, p. 244506, 2007.

[86] Popov, A. V., Melvin, J., and Hernandez, R., "Dynamics of swelling hard spheres surmised by an irreversible Langevin equation," *J. Phys. Chem. A*, vol. 110, pp. 1635–1644, 2006.

[87] Popov, A. V., Viehman, D. C., and Hernandez, R., "Nonequilibrium heat flows through a nanorod sliding across a surface," *J. Chem. Phys.*, vol. 134, p. 104703, 2011.

[88] Prost, J. and Gasparoux, H., "Determination of the twist viscosity coefficient in the nematic mesophases," *Phys. Lett.*, vol. 36A, pp. 245–246, 1971.

[89] Rebertus, D. and Sando, K., "Molecular dynamics simulation of a fluid of hard spherocylinders," *J. Chem. Phys.*, vol. 67, pp. 2585–2590, 1977.

[90] Renner, C., Löwen, H., and Barrat, J., "Orientational glass transition in a rotator model," *Phys. Rev. E*, vol. 52, pp. 5091–5099, 1995.

[91] Roichman, Y., Grier, D. G., and Zaslavsky, G., "Anomalous collective dynamics in optically driven colloidal rings," *Phys. Rev. E*, vol. 75, pp. 020401(R)–1–020401(R)–4, 2007.

[92] Roichman, Y., Waldron, A., Gardel, E., and Grier, D. G., "Optical traps with geometric aberrations," *Appl. Opt.*, vol. 45, pp. 3425–3429, 2006.

[93] Roichman, Y., Wong, V., and Grier, D. G., "Colloidal transport through optical tweezer arrays," *Phys. Rev. E*, vol. 75, pp. 011407–1–011407–4, 2007.

[94] Roichman, Y., Sun, B., Roichman, Y., Amato-Grill, J., and Grier, D. G., "Optical forces arising from phase gradients," *Phys. Rev. Lett.*, vol. 100, pp. 013602–1–013602–4, 2008.

[95] Rotunno, M., Bellini, T., Lansac, Y., and Glaser, M., "Phase behavior of polarizable spherocylinders in external fields," *J. Chem. Phys.*, vol. 121, pp. 5541–5549, 2004.

[96] Schilling, T. and Frenkel, D., "Self-poisoning of crystal nuclei in hard-rod liquids," *Phys. Rev. Lett.*, vol. 92, pp. 085505–1–085505–4, 2004.

[97] Schwanzer, D., Coslovich, D., Kurzidim, J., and Kahl, G., "Effects of porous confinement on the structural properties of the gaussian core model," *Mol. Phys.*, vol. 107, pp. 433–441, 2009.

[98] Somer, F. L. and Hernandez, R., "Stochastic dynamics in irreversible nonequilibrium environments. 3. Temperature-ramped chemical kinetics," *J. Phys. Chem. A*, vol. 103, pp. 11004–11010, 1999.

[99] Somoza, A. and Tarazona, P., "Nematic and smectic liquid crystals of hard spherocylinders," *Phys. Rev. A*, vol. 41, pp. 965–970, 1990.

[100] Stallmach, F., K arger, J., Krause, C., Jeschke, M., and Oberhagemann, U., "Evidence of anisotropic self-diffusion of guest molecules in nanoporous materials of MCM-41 type," *J. Am. Chem. Soc.*, vol. 122, pp. 9237–9242, 2000.

[101] Stempniewicz, M., Khalil, A., Rohwerder, M., and Marlow, F., "Diffusion in coiled pores - learning from microrelease and microsurgery," *J. Am. Chem. Soc.*, vol. 129, pp. 10561–10566, 2007.

[102] Tao, Y.-G., den Otter, W. K., Padding, J. T., Dhont, J. K. G., and Briels, W. J., "Brownian dynamics simulations of the self- and collective rotational diffusion coefficients of rigid long thin rods," *J. Chem. Phys.*, vol. 122, pp. 244903–1:10, 2005.

[103] Thomas J. Pucadyil, Soumi Mukherjee, A. C., "Organization and dynamics of NBD-labeled lipids in membranes analyzed by fluorescence recovery after photobleaching," *J. Phys. Chem. B*, vol. 111, pp. 1975–1983, 2007.

[104] Tucker, A. K. and Hernandez, R., "Observation of a trapping transition in the diffusion of a thick needle through fixed point scatterers," *J. Phys. Chem. B*, vol. 114, pp. 9628–9634, 2010.

[105] Tucker, A. K. and Hernandez, R., "Absence of enhanced diffusion in the dynamics of a thick needle through three-dimensional fixed point scatterers," *J. Phys. Chem. B*, vol. 115, pp. 4412–4418, 2011.

[106] van der Hoef, M. and Frenkel, D., "Long-time tails of the velocity autocorrelation function in two- and three-dimensional lattice-gas cellular automata: A test of mode-coupling theory," *Phys. Rev. A*, vol. 41, pp. 4277–4282, 1990.

[107] van Ketel, W., Das, C., and Frenkel, D., "Structural arrest in an ideal gas," *Phys. Rev. Lett.*, vol. 94, pp. 135703–1–135703–4, 2005.

[108] Vasanthi, R., Ravichandran, S., and Bagchi, B., "Anisotropic diffusion of tagged spheres near the isotropic-nematic phase transition," *J. Chem. Phys.*, vol. 115, pp. 10022–10028, 2001.

[109] Vijayakumar, V., Murugadass, K., and Mohan, M. M., "A study of reentrant smectic ordering in hydrogen bonded ferroelectric dodecyloxy benzoic acid and tartaric acid liquid crystal," *Mol. Cryst. Liq. Cryst.*, vol. 517, pp. 43–62, 2010.

[110] Williamson, D., Thacker, N., and Williams, S., "Effects of intramolecular dipolar coupling on the isotropic-nematic phase transition of a hard spherocylinder fluid," *Phys. Rev. E*, vol. 71, p. 021702, 2005.

[111] Wilson, M., "Molecular dynamics simulations of flexible liquid crystal molecules using a Gay-Berne/Lennard-Jones model," *J. Chem. Phys.*, vol. 107, pp. 8654–8663, 1997.

[112] Yoshizaki, T. and Yamakawa, H., "Dynamics of spheroid-cylindrical molecules in dilute solution," *J. Chem. Phys.*, vol. 72, pp. 57–69, 1980.